Forschungszentrum Karlsruhe
Technik und Umwelt

Wissenschaftliche Berichte
FZKA 6383
INV-CIT(98)-P026

ZrO_2 Dissolution by Molten Zircaloy and Cladding Oxide Shell Failure. New Experimental Results and Modelling

P. Hofmann, J. Stuckert, A. Miassoedov,
M. S. Veshchunov*, A. V. Berdyshev*, A. V. Boldyrev*

Institut für Materialforschung
Projekt Nukleare Sicherheitsforschung

*Nuclear Safety Institute (IBRAE), Russian Academy of Sciences, Moscow

Forschungszentrum Karlsruhe GmbH, Karlsruhe
1999

ZrO_2-Auflösung durch geschmolzenes Zircaloy und ZrO_2-Oxidschicht-Versagenskriterium. Neue experimentelle Ergebnisse und deren Modellierung

Zusammenfassung:

Dieser Bericht faßt die Aufgabe 2.4 des europäischen Projektes "Corium Interactions and Thermochemistry" (CIT) zusammen, die im Rahmen des 4. Rahmenprogrammes "Nuclear Fission Safety" der EG durchgeführt wurde. Der experimentelle Teil dieser Aufgabe wurde in der Zeit von 1997 bis 1999 im Forschungszentrum Karlsruhe durchgeführt. Der analytische Teil der Aufgabe 2.4 erfolgte am Institut für nukleare Sicherheit der Russischen Akademie der Wissenschaften (IBRAE).

Die Auflösung von ZrO_2 durch flüssiges Zircaloy ($\geq$ 1760°C) beeinflußt viele physikalisch-chemische Prozesse während der Kernzerstörung: (i) Verflüssigung von ZrO_2 ungefähr 1000°C unterhalb seines Schmelzpunktes, (ii) Verlagerung von (U, Zr, O) Schmelzen nach dem Versagen der äußeren ZrO_2 Schicht auf Zircaloy-Hüllrohren und (iii) die Spaltproduktfreisetzung.

Um die widersprüchlichen Versuchsergebnisse in der Literatur zu verstehen, und die Ungenauigkeiten des Hüllrohrversagenskriteriums zu reduzieren, wurden unterschiedliche Experimente durchgeführt: (i) isotherme ZrO_2 Auflösungstests mit ZrO_2-Tiegeln unterschiedlicher Abmessungen mit und ohne Bodenisolierung durch Y_2O_3-Scheiben bei 2100, 2200 und 2300°C und Reaktionszeiten bis 30 Minuten, (ii) Experimente zur Ermittlung des Versagenskriteriums von ZrO_2-Schichten auf Zircaloy-Hüllrohren. Zusätzlich wurden die früheren ZrO_2-Auflösungsests, die 1989 im damaligen Kernforschungszentrum (KfK) und bei AECL in Kanada durchgeführt wurden, mit den neuen FZK-Testdaten verglichen.

Die wesentlichen Versuchsergebnisse sind:

- Die Tiegel/Schmelze-Wechselwirkungen werden durch die Sauerstoffdiffusion entlang der ZrO_2-Korngrenzen bestimmt und laufen in zwei Schritten ab: Erosion (oder Auflösung) und Korrosion des ZrO_2. Während der Korrosionsphase hört die Auflösung des ZrO_2 auf, und es beginnt sogar ein Wachstum der ZrO_2-Tiegelwand. Der Erosions/Korrosionsprozeß schreitet bis zur Sauerstoffsättigung der Schmelze fort und in einigen Tests geht dieser Vorgang mit einer langsameren Kinetik weiter, unter gleichzeitiger Ausscheidung einer keramischen ZrO_2-Phase in der sauerstoffgesättigten Schmelze. Die Kinetik ändert sich mit dem Verhältnis zwischen der ZrO_2-Tiegeloberfläche in Kontakt mit der Schmelze und dem Zircaloy-Schmelzvolumen (S/V) und hängt außerdem stark von der Tiegelwandstärke ab;

- Die Tests bzgl. des Versagenskriteriums der ZrO_2-Oxidschicht zeigen eine klare Korrelation zwischen der Aufheizrate und der Versagenstemperatur. Die Versagenstemperatur der Oxidschicht nimmt kontinuierlich mit der Aufheizrate ab und bleibt nach Erreichen einer bestimmten Grenze konstant.

Das von IBRAE entwickelte analytische Modell erklärt die beobachten Widersprüche in den früheren ZrO_2-Auflösungsexperimenten und beschreibt gleichzeitig die neuen FZK-Versuchsergebnisse:

- Das ZrO_2-Auflösungsmodell kann die beiden Prozesse der Erosion und Korrosion des ZrO_2 in den früher beobachteten KfK-, und AECL-Tests sowie die Erosionsphase in den neuen FZK-Tests widerspruchsfrei beschreiben. Die Unterschiede zwischen den KfK-, AECL- und FZK-Resultaten liegen in den verschiedenen Tiegel/Schmelze-Geometrieverhältnissen, die unterschiedliche charakteristische Zeiten in den Auflösung- und Sauerstoff-Diffusionprozessen bewirken.
- Die Analyse der Versuchsergebnisse der ZrO_2-Oxidschicht-Versagenstests, die mit dem Code SVECHA/QUENCH durchgeführt wurde, erlaubt die Identifikation und die Modellierung des unterschiedlichen Versagensverhaltens der Oxidschichten, das in den neuen FZK-Tests mit kurzen Brennstababschnitten beobachtet wurde.

ABSTRACT

This report summarises the task 2.4 of the European Project on "Corium Interactions and Thermochemistry (CIT)" conducted within the 4th Framework Programme on "Nuclear Fission Safety". The experimental part of this task was performed during 1997/99 at the Forschungszentrum Karlsruhe. The analytical part of the task 2.4 was conducted at the Nuclear Safety Institute of the Russian Academy of Sciences (IBRAE).

The dissolution of ZrO_2 by molten Zry ($\geq$ 1760°C) influences many physico-chemical processes during core degradation: liquefaction of ZrO_2 at about 1000°C below its melting point, relocation of (U, Zr, O) melts after failure of the outer ZrO_2 layer on Zircaloy cladding tubes and fission product release rates.

In order to understand apparent inconsistencies in the experimental results published in the literature and to reduce uncertainties on the clad failure conditions, different tests were carried out: (i) isothermal ZrO_2 dissolution tests with ZrO_2 crucibles of different dimensions with and without bottom isolation by yttria disks at 2100, 2200 and 2300°C and reaction times up to 30 min, and (ii) ZrO_2 shell failure tests with short pre-oxidised cladding tubes filled with ZrO_2 pellets. In addition, new post-test analysis of the earlier tests on ZrO_2 crucibles dissolution performed by KfK in 1987 and AECL were performed and compared with the new FZK test data,.

The main test results are:

- The crucible/melt interaction is governed by the oxygen diffusion along ZrO_2 grain boundaries and occurs in two stages: erosion (or dissolution) and corrosion of the ZrO_2. During the corrosion stage of the ZrO_2 the dissolution ceases and an interface oxide layer growth on the ZrO_2 crucible wall commences. The erosion/corrosion process develops up to melt saturation by oxygen and in some tests continues with a slower rate accompanied by a ceramic ZrO_2 phase precipitation in the oxygen-saturated (Zr,O) melt. The kinetics increases with the surface to volume (*S/V*) ratio, that means the ZrO_2 surface (S) in contact with the melt volume (V), and strongly depends on the crucible wall thickness.
- ZrO_2 shell failure tests show a clear correlation between the heat-up rate and the failure temperature. The cladding failure temperature continuously decreases with increasing heat-up rate and after reaching a certain limit remains constant.

The developed analytical model by IBRAE explains the disagreement observed in previous dissolution results and reproduces correctly the new FZK tests:

- The ZrO_2 dissolution model is able to describe self-consistently the erosion and corrosion stages observed in the previous KfK and AECL tests and the unique erosion stage observed in new FZK tests. Differences between the KfK, AECL and FZK results are due to different crucible/melt geometries which induce different characteristic times in dissolution and oxygen diffusion processes.
- The analysis of ZrO_2 dissolution results using the single rod degradation code SVECHA/QUENCH enables the identification and modelling of different failure modes observed in the new FZK tests.

CONTENTS

Part I. ZrO_2 Dissolution by Molten Zircaloy

1. Introduction

The objective of experiments was to repeat the original ZrO_2 dissolution tests of Hofmann et al. [1,2] with the use of crucibles of higher density and partially with crucible cavity bottom isolation by Y_2O_3 discs (one-dimensional dissolution), and to compare the new test results with the recently performed tests in AECL [3]. Owing to the relatively rapid process of crucible through-wall melting (less than 10min at 2200°C), some tests were carried out without a Y_2O_3 disc. Self-consistent interpretation, modelling and comparative analysis of the new and previously performed tests [1-3], was the main objective of the analytical work.

1.1. Review of existing tests

The first published dissolution rates for ZrO_2 in molten Zry are from the work of Hofmann et al. [1,2]. Their data (hereafter called as KfK data) were obtained from crucible-based experiments wherein molten Zry charges were held in ZrO_2 crucibles for known time intervals while being isothermally heated at temperatures in the range 2000-2400°C. The used crucibles were of cubic zirconia stabilised with 2.7 wt.% CaO and were ~ 75% of theoretical density. Melt analysis was performed by an indirect method involving comparison of the melt microstructures and phase contents with those of previously melted ZrO_2 standards. The amount of dissolved ZrO_2 in each crucible melt was determined by correlating the measured area fraction of ZrO_2 in the cooled melt with those in the standards. After an initial brief period of very rapid ZrO_2 dissolution, the dissolution rate followed a parabolic time law.

However, this procedure of post-test analysis neglects additional amounts of oxygen in the melt transported from the oxide by the diffusion mechanism. For this reason, interpretation of the obtained data in terms of dissolved ZrO_2 in [1] might be erroneous. Nevertheless, direct data [1] are rather valuable and can be correctly reinterpreted by a model taking into account the diffusion fluxes in the solid phase (see below).

The experimental data [1] on the ZrO_2 crucible wall dissolution by molten Zry had only preliminary character, however, unambiguously demonstrated that the ZrO_2 dissolution rates at high temperatures ($T \geq 1900$°C) are significant and comparable with the UO_2 dissolution rates measured in the analogous crucible tests. Besides, it was observed in these tests that the composition of the solidified melt was spatially homogeneous, analogously to the observations in the UO_2 dissolution tests. This implies that convective mixing of the melt occurs also in the course of ZrO_2 dissolution by molten Zry.

Moreover, additional visual analysis of the post-test photographs of the specimens obtained in [1] (see below Section 3) apparently evidences that after cessation in ~ 500 s of the dissolution process the propagation of the solid/liquid interface changes its direction from inward to outward, that is the erosion of the ZrO_2 turns to the corrosion.

A recent AECL study of Hayward and George [3] was designed to overcome deficiencies of indirect analysis of [1] by using a more direct chemical analysis method that can distinguish between chemical dissolution and oxygen diffusion reactions. The experiments involved isothermal heating tests at 2000-2300°C with Zry charges in yttria-stabilised ZrO_2 crucibles that also contained ~1.4 wt.% HfO_2 as a natural impurity. Each post-test melt was then sectioned, dissolved and analysed for

Zr, Hf, and Y by ICP spectrometry. Optical and electron-microscopy examinations and analyses were also performed on the post-test samples. The Hf content of each melt was used to calculate the corresponding crucible weight fraction that had dissolved or become dispersed in the melt, based on the assumption that Hf dissolves congruently with Zry.

Chemical analyses of the melts [3] indicates that, in all but the 2000°C experiments, rapid dissolution had occurred during the first ~ 100-200 s. After this time, a solid ZrO_{2-x} layer formed at the crucible/melt interface and grew at a rate that was proportional to $t^{1/2}$ but independent of the reaction temperature.

1.2. Review of existing models

Kinetics of ZrO_2 dissolution by molten Zry was modelled by Veshchunov and Berdyshev [4,5] within a general approach for modelling of more complicated process of simultaneous dissolution of UO_2 and ZrO_2 by molten Zry, observed in the integral CORA tests as an important mechanism of core degradation. Detailed qualitative and quantitative data on post-tests metallographic examinations of the fuel rods in the bundle CORA tests allowed generalisation of the theoretical UO_2 dissolution model of Veshchunov and Hofmann [6] for modelling simultaneous dissolution kinetics. As a particular case of the general model, separate dissolution of ZrO_2 by molten Zry was specially analysed in [4,5].

In accordance with visual observations of [1], the model qualitatively correctly describes system behaviour at early (erosion) and late (corrosion) stages of the interaction process. It was demonstrated that the direction and velocity of the interface propagation is determined by the oxygen flux matching condition at this interface. In the initial stage of solid/liquid interactions the oxygen mass flux in the convectively stirred melt is rather large in comparison with that in the solid phase; for this reason, a high dissolution rate proportional to the difference between the two fluxes prevails. Since the melt approaches the saturation composition as a result of the dissolution process, the convective flux reduces and eventually matches the oxygen flux in the ZrO_2. This moment corresponds to the cessation of the erosion stage. After this moment the flux in the solid phase becomes larger than that in the melt since reduction of the latter with time is much quicker. According to the flux matching equation the velocity of the interface propagation changes its sign and the corrosion stage commences.

The subsequent experiments [3] confirmed the independent model predictions [4,5] qualitatively (two stages of erosion/corrosion process) and quantitatively (close to the parabolic rate law of oxide layer growth at the second, corrosion stage).

A further development of the model and a more thorough analysis of the new FZK tests on ZrO_2 dissolution by molten Zry in comparison with the previous tests, was foreseen within the 4th Framework Programme.

2. Experimental

Isothermal heating experiments within the temperature range 2100°C to 2300°C and with annealing times up to 30 min were performed to study the dissolution of CaO-stabilised zirconia crucibles by molten Zircaloy-4 (Zry). The experiments should simulate the dissolution of steam-oxidised cladding surface layers by the molten Zry cladding between the ZrO_2 layer and the fuel pellet during a high-temperature transient in a severe fuel damage accident. The comparison of the experimental results with those of P. Hayward's tests [3] showed a strong dependence of the dissolution rate on the crucible geometry.

2.1. Materials

The tests were performed with crucibles of CaO-stabilised zirconia containing charges of as-received (oxygen-free) Zry-4 (Table 1). The crucibles were fabricated by the company HITEC-MATERIALS GmbH&Co.KG (Karlsruhe) from partially CaO-stabilized (65% of cubic phase and 35% of monoclinic phase) powder, with nominal CaO contents of 4.2 wt.%. The geometrical parameters of crucibles were: inner diameter - 17.5 mm, wall thickness – about 4.5 mm, height – about 32 mm. The weight of crucibles was about 61 g, the crucible density – 93% (±1%) of TD.

In some of the experiments the bottom of the crucible cavity was covered by a Y_2O_3 disc of 2.5 mm thickness. The discs were fabricated also by HITEC from Y_2O_3 powder of 99.9% purity. The disc density was 97% (±1%) of TD.

The initial weight of the Zry charge (cylindrical pellet of 11.7 mm diameter) was 10 g.

2.2. Test procedure

The specimens were inductively heated by means of a tungsten susceptor in the LAVA facility (Fig. 1). In each test the furnace was several times evacuated and backfilled with high purity argon. Then the specimen was slowly heated (~ 1 K/s) up to about 1650°C and kept at this temperature for about 3 min for thermal equilibration. The specimen was then further heated to the desired test temperature with about 9 K/s. After the pre-determined annealing time the specimen was rapidly cooled-down (~ 5 K/s) to about 1500°C. The further cooldown was controlled with about 0.5 K/s.

The crucible temperatures were continuously recorded by a monochrome pyrometer and a W/Re thermocouple. The pyrometer, focused on the bottom of crucibles through a fused quartz window in the furnace bottom, was also used as feedback device to a high frequency generator. The sheathed W/Re thermocouple was used as additional monitor device; the distance between thermocouple and the upper level of the molten Zry was about 12 mm.

The millivolt outputs from the pyrometer and the thermocouple were fed into the computer-based data-acquisition system DATASCAN and recorded at 0.1 s intervals. A typical plot of a corresponding measurement is shown in Fig. 2. The temperatures for the pyrometer and the W/Re-thermocouple were calculated according to empirical approximation formulas:

$$T_{Py}(°C) = 0.1513 \cdot U + 998.1, \quad (1)$$

(for the ZrO_2-emissivity of ε=0.2 and the temperature range T=1200..2300°C),

$$T_{TC}(°C) = 0.0674 \cdot U^3 - 4.8379 \cdot U^2 + 178.67 \cdot U - 1100.1, \quad (2)$$

(in the temperature range T=1400..2300°C),

where U is the voltage in mV.

The melt duration was identified as the period between the melting point of the Zry charge, measured in commissioning tests, and the point corresponding to the α-Zr(O) solidus temperature with an oxygen content $\approx$ 35 at.%. During the commissioning

tests the temperature was increased in equal steps of ~ 50 K, with a visual control of the physical state of the Zry charge. The melting point of Zry corresponds to the thermocouple measured value of 1690°C and the pyrometer measured value of 1900°C (both values do not agree with the melting point of as-received Zry-4 of about 1760°C). The temperatures indicated in this report for the FZKA experiments (hereafter temed FZK tests) are the results of pyrometer bottom temperature measurements and might be higher than the corresponding melt temperatures. For instance, in the AECL experiments the temperature difference between the melt surface and the walls measured with a similar pyrometer attained 50 - 100 K.

Fig. 2 shows a strong influence of the high frequency generator on the thermocouple measurements: the higher the power of generator the lower the millivolt-output of the thermocouple. The correct temperature corresponds to that in the absence of any generator power.

Fig. 3 through Fig. 10 present the plots of temperature measurements for large crucible tests without ZrO_2 crucible failure (no melt-through of the crucible wall). Fig. 11 through Fig. 13 present the plots of temperature measurements for small crucible tests.

It should be mentioned, that the temperature measurements have the following uncertainties:

- owing to the intensive heat (radiation) losses from the melt surface there is significant difference (50 - 100 K) between the temperature measurements on the crucible bottom and on the melt surface. This should be taken into account for the comparison of temperature values measured in the AECL experiments (pyrometric melt surface measurement) and FZK experiments (pyrometric crucible bottom measurement);
- owing to a gas filled void between the yttria disk and crucible bottom (see Fig. 17), the temperature difference between the melt and crucible bottom becomes even larger for the tests with Y_2O_3 discs and can attain ~100 K.

After completion of the tests, each specimen was sectioned along a cylindrical axial plane using a diamond sectioning wheel. One half of each specimen was embedded in epoxy and polished prior to examination by an optical microscope and by SEM/EDX analysis. From the other half the melt region was mechanically separated for chemical analysis.

3. Test results

Sixteen tests were carried out altogether (Table 2). The reaction conditions were 2100, 2200 and 2300°C and annealing times up to 30 min. However, some of the crucibles failed at 2200°C after 15 min and at 2300°C after 3 min.

The post-test examinations showed a white metallic-looking stripe around the circumference on the outer surface of some crucibles (Fig. 14 through Fig. 16).The height of the stripes corresponds to the melt height. This stripe was identified by SEM/EDX analysis as metallic α-Zr(O) precipitates within the ZrO_2 crucible matrix. The ZrO_2 is reduced by oxygen diffusion into the melt [and precipitates on cool down: $ZrO_{2-x} \rightarrow ZrO_2 + \alpha$-Zr(O)].

Optical microscope examinations of the sectioned specimens showed, that the crucible dissolution occurred in all the FZK test specimens (Fig. 17–18). Similar observations at these temperatures ($\geq$ 2100°C) and time durations (> 100 s) were made in the AECL [3] tests (Y_2O_3 stabilised zirconia crucibles with a density of 5.9

g/cm³) and the previous KfK tests [1] (CaO stabilised zirconia crucibles with a density of 4.26 g/cm³). The formation and growth of a ZrO_{2-x} layer at the crucible/melt interface was not observed in the FZK tests. However, such layers have formed in the earlier AECL and KfK experiments and also in the FZK tests with AECL crucibles, performed in the LAVA rig under the same conditions (Fig. 19). The interface layers exhibited a typical «prior-cubic» structure containing coarse bands and fine lamellae of α-Zr(O) precipitates. Fig. 20 shows a comparison of the melt-crucible interaction zones of the AECL and FZK experiments at 2100°C. In the FZK experiments the interaction zone is relatively thin and has no clear structure with bands and lamellae as in the AECL experiments. Fig. 21 shows the comparison of a transition layer formation in the FZK, KfK and AECL experiments at 2200°C and melt duration of about 10 min. A well-structured transition layer, which can be considered as a «corrosion» layer, can be seen in the AECL and KfK tests; such a layer could not be observed in the new FZK tests – the transition region in the FZK consists only of a small interaction zone.

The difference between the AECL and FZK results can be explained by different *S/V* (interaction surface to melt volume) ratios and wall thickness which determine amounts and rates of oxygen diffusion from the ZrO_2 crucible into the molten Zircaloy (see Section 4). Different crucible densities (93%TD for the FZK and 75%TD for the KfK crucibles) should be also taken into consideration.

In contrast to the AECL tests in which no crucible melting through occurred, in the KfK tests the crucibles melted through at 2300°C after 3 min: Fig. 22. The crucibles in the new FZK tests failed already at 2200°C after 15 minutes. Fig. 23 shows a typical example of a failed crucible. Two phenomena can be noted: 1) the crucible melted through at the upper half of the melt volume; 2) the W-susceptor remained intact – no chemical interaction occurred between the released (Zr, O) melt and the tungsten.

The chemical behaviour of the Y_2O_3 discs was investigated by various methods. The optical microscopy showed no change of the disc thickness. There is only a small negligible dissolution of the upper disc edge. SEM/EDX analysis showed the existence of the yttrium traces along the thin transition layer between the melt and crucible after 5 minutes of annealing time. After an interaction time of 30 minutes yttrium traces could also be observed in the upper parts of the solidified melt.

3.1. SEM/EDX analyses

The measurements were performed with a Scanning Electron Microscope (SEM) type JEOL 6100, using a 15 kV accelerating voltage. For the Energy Dispersion X-Ray (EDX) examination a Kevex detector type Quantum 3600-19 was used.

3.1.1. Specimen #5 (2100°C, 101 s test duration)

Fig. 24 shows the SEM photos and EDX results of interaction zones between the melt and the crucible wall and between the melt and yttria disc. One can see a thin α-Zr(O) layer with small size ceramic precipitates in the area of the melt-crucible interaction zone. Adjacent to this α-Zr(O) layer, α-Zr(O) precipitates have formed in the ZrO_2 crucible matrix.

There are no ceramic precipitates in the bulk of the solidified melt.

The optical view of the cross-section with yttria disc shows clearly two optically different zones in Y_2O_3. Near the melt the disc is dark; the other part of the disc is bright – identical to the initial Y_2O_3 material. However, the precision of the EDX

analysis does not allow determination of an oxygen gradient through the disc, i. e. the difference of oxygen content in the upper and lower parts of the yttria disc is less than ca 3 at.%.

3.1.2. Specimen #4 (2100°C, 574 s test duration)

Fig. 25 shows the SEM photos and EDX results of interaction zones between the melt and crucible wall and between the melt and yttria disc. The interaction zone (with a thickness of about 200 μm) contains uniformly distributed two phases: α-Zr(O) and ceramic precipitates. The ceramic phase contains traces of calcium and yttrium. The calcium content in the ceramic phase is equal to calcium content in the crucible matrix.

There are two types of precipitates in the bulk of the melt: a) small-size and b) large-size ceramic dendrites. The large-size dendrites contain yttrium traces.

The SEM/EDX examination of the crucible wall microstructure shows the formation of α-Zr(O) metallic precipitates in the crucible matrix (Fig. 26). The electrical resistance measurement between the melt and the white stripe on the outer surface of the crucible wall shows continuous connection of the metallic precipitates (the resistance was about 3 ohm).

3.1.3. Specimen #7 (2100°C, 750 s test duration)

In the bulk of the (Zr,O) melt there are two different regions with the different amount of precipitates (Fig. 27): a) a large number and b) a small number of ceramic precipitates. The ceramic precipitates in a) contain more yttrium compared to the precipitates in b).

The interface zone between the melt and the crucible wall consists of three typical zones: 1) large-size ceramic precipitates in the α-Zr(O); 2) small-size ceramic precipitates in the α-Zr(O) and 3) a non-porous layer of the crucible matrix. The remaining bulk of the crucible matrix is porous and contains metallic precipitates along the grain boundaries.

3.1.4. Specimen #8 (2100°C, 1778 s test duration)

The formation of the α-Zr(O) precipitates in this crucible wall was investigated in more detail. Fig. 28 shows the microstructure of the crucible wall matrix. The α-Zr(O) precipitates along the grain boundaries of the ZrO_2 matrix exist only in the area between the melt and the outer crucible wall surface with white stripes. No metallic precipitates can be observed in other areas of the crucible matrix. The formation of the metallic precipitates can be interpreted as the oxygen diffusion process along the ZrO_2 crucible grain boundaries into the melt. This process enhances the oxygen diffusion from the bulk to the melt and the quantity of interconnected liquid α-Zr(O) along the grain boundaries. The liquid phase at the ZrO_2 grain boundaries accelerates the local dissolution and results in the local failure with melt-through of the crucible wall.

Fig. 29 shows interaction zones between the melt and the crucible wall, and between the melt and the Y_2O_3 disc. The interaction zone between the melt and the crucible wall contains α-Zr(O) areas with small-size ceramic precipitates A small layer with large-size ceramic precipitates exists between the interaction zone and the melt. The EDX analysis of the upper part of Y_2O_3 disc reveals some oxygen diffusion to the melt.

The bulk of the melt in this test consists of two slightly different areas (Fig. 30). In the upper part of the melt large-size ceramic dendrites with yttrium content up to 10 at% can be seen. In lower part of the melt small-size dendrites can be recognised which contain no yttrium.

3.1.5. Specimen #13 (2200°C, 106 s test duration)

The interaction zone between the melt and the crucible wall consists of two ceramic phases (Fig. 31): 1) the matrix with about 8 at.% calcium and about 2 at.% yttrium and 2) small-size precipitates with yttrium contents of about 17 at.%.

In the upper part of the melt there are only large-size ZrO_{2-x} precipitates without yttrium traces. The lower part of the melt contains two kinds of ceramic precipitates: the low-size precipitates with yttrium and calcium traces, and large-size ZrO_{2-x} precipitates.

3.1.6. Specimen #14 (2200°C, 102 s test duration)

There exists a thin layer in the crucible matrix along the melt-crucible interaction zone which contains α-Zr(O) traces in the matrix along the grain boundaries (Fig. 32). In the melt along the melt-crucible interaction boundary one can see a few longitudinal stripes which contain ceramic precipitates. These ceramic precipitates consist of two phases: inside the ZrO_{2-x} phase with a calcium content of about 4 at.% formed another dark (Zr, Ca, O) phase with a much higher calcium content, of about 18 at.%.

The solidified α-Zr(O) melt contains the small-size ZrO_{2-x} precipitates and some of the large-size precipitates with a calcium content of about 15 at.%.

3.1.7. Specimen #12 (2200°C, 587 s test duration)

The solidified melt contains well-formed and homogeneously distributed ZrO_{2-x} dendrites with calcium traces up to 1 at.% (Fig. 33). There are no calcium traces in the metallic α-Zr(O) phase.

Fig. 34 shows the structure of the interaction zone between the melt and the crucible material. Along the interaction boundary one can see a thin layer of solidified α-Zr(O) with small-size ZrO_{2-x} precipitates.

The crucible matrix shows the α-Zr(O) precipitates along the grain boundaries.

3.1.8. Specimen #24 (2200°C, 121 s test duration)

The solidified melt consists of the α-Zr(O) matrix (Fig. 35), which contains well-formed and homogeneously distributed ZrO_{2-x} dendrites with a calcium content up to 3.5 at.% (the same content of calcium as in the crucible wall matrix). There is no calcium in the α-Zr(O) phase. The structure of ZrO_{2-x} dendrites is homogeneous and contains no α-Zr(O) lamellae, i.e. there was no eutectoid decomposition of ZrO_{2-x} during cooling.

The interface boundary between the melt and the crucible has no complex transition structure. The layer of the crucible matrix along the interface boundary shows no pores.

On the inner crucible wall above the melt surface a small amount of a $CaO\text{-}ZrO_2$ eutectic ($T_{eut} \approx 2250°C$) has formed.

3.1.9. AECL specimens Z-11 (2200°C, 612 s test duration) and Z-18 (2300°C, 195 s test duration)

In order to compare the FZK and AECL results, two of the AECL post-test crucibles were investigated at FZK. The cross-sections show, in contradiction to the FZK results, negligible dissolution of the crucibles and quick formation of a ZrO_{2-x} transition layer with "prior cubic" structure. The α-Zr(O) lamellae in this layer contain low-size ceramic precipitates and traces of Sn (Figs. 36 and 37).

Although the dissolution of the ceramic crucible was relative small, the solidified melt contains well-developed ZrO_{2-x} dendrites. Obviously an intensive oxygen diffusion from the crucible wall to the melt occurred.

3.2. Chemical melt analyses

The halves of the melt zones were separated from crucible wall and studied with the help of different chemical methods. The chemical analysis was performed for O, Fe, Cr, Y, Hf, Sn, Ca. The results are given as wt.% values in Table 3.

The oxygen content increases with the growth of the temperature and the melt duration. The Y (tests with bottom isolation) and Ca contents increase with the growth of temperature and melt duration.

3.3. Phase-area analyses

In all specimens, except specimen #5, ceramic ZrO_{2-x} dendrites have developed within the metallic α-Zr(O) matrix. The dendritic structure is better developed in the specimens with longer interaction times. In order to determine the relative areas of ceramic and metallic phases in the solidified melts, image analyses were performed on Back Scattering Electrons micrographs using OPTIMAS-software. The microscope enlargement was 80 times for all the FZK specimens except the specimens #13, 14 (x400 enlargement). For specimens #4 and #8 melt areas were chosen with small-size dendrites (without any yttrium traces). The contrast threshold levels were adjusted for each analysis to distinguish the ceramic phase, the metallic phase and the voids. The same measurements were performed in the solidified regions of the AECL (Figs. 36 - 37) and KfK specimens (Figs. 38 - 42).

In order to reproduce the main qualitative observations of the previous AECL tests, the new FZK test series with small crucibles was performed under similar conditions and with the same crucible. However, to avoid the melt transfusion from the top of the crucibles at a late stage of the interactions, the initial Zry charge volume was decreased in comparison with the AECL tests, thus, the *S/V* ratio was increased, correspondingly. The post-test photographs and phase image analysis results are presented in Figs. 43 - 45.

The phase area analysis results of all the tests are presented in Tables 4 and 5 (columns «melt phase analysis»). The sum of ceramic and metallic parts in Table 5 is normalised to 100%, i.e. the voids are not included.

The data in Table 4 show that the content of ceramic precipitates in the solidified melts are higher in the AECL tests in comparison with the FZK tests under the same temperature and time conditions. Moreover, the precipitates in the FZK tests have formed mainly during the solidification process, whereas a part of the precipitates in the AECL tests was apparently formed already at temperature. This can be justified in the the following manner :

From the analysis of the ceramic phase content in earlier dissolution experiments [1] with known relationship between dissolved ZrO_2 and the resulting amount of ceramic (Zr, Ca, O) precipitates in the solidified melt, the following empirical formula was derived:

$$W = (S+34)/1.4, \tag{3}$$

where W is the weight part (in percents) of dissolved ZrO_2 in the melt, and S is the ceramic (Zr, Ca, O) phase area (in percents) in the melt. The weight part of the oxygen in ZrO_2 is 32/(32+91)=0.26. Therefore the correlation between the dissolved oxygen in the melt (O) and the ceramic phase in the melt (S) is:

$$O = 0.26\cdot(S+34)/1.4 = 0.186\cdot(S+34), \tag{4}$$

where O is presented in weight percents, S - in area percents. The presence of a stabiliser in the ZrO_2 material has only a small influence on the oxygen concentration in the melt [1].

Fig. 46 shows the liquidus points in the Zr-O phase diagram at 2100, 2200 and 2300°C corresponding to 12.7, 13.5, 14.7 oxygen weight percents. The calculated (in accordance with Eq. (4)) oxygen content in the melt at a late stage of the interactions, presented in the table in Fig. 46 for AECL tests, are significantly higher than the indicated liquidus pointsThe other estimation of the oxygen contents on the base of the ICP measurements [3] give even higher values up to 25 wt.%. Therefore, some of the cubic ZrO_2 precipitates in the melt were formed already at temperature. A similar behaviour revealed in the KfK tests is presented in Fig. 47.

3.4. Image analyses

Quantitative image analysis of the specimen cross-sections were performed to determine the volume of the dissolved part of the ZrO_2 crucibles. The initial (before the dissolution process) configuration of the crucibles was restored in the crucible cross-section images by means of graphic software (Figs. 48 - 50). Under the assumption of a cylindrical symmetry of the dissolution process the dissolved volume of each crucible was determined by means of the OPTIMAS-Software in accordance with the formula:

$$V = v \times \pi \times \sum_i r_i \ , \tag{5}$$

where v is the volume of one pixel; i numerates pixels in the dissolved area; r_i is a pixel distance from the cylindrical axis.

The same evaluation and calculation procedures were performed for the examined AECL post-test crucibles. The final quantitative image analysis results are presented in Table 3. On the base of this analysis the following conclusions can be made:

1. The dissolution rate grows with temperature;
2. After certain initial time period there is no growth of the dissolved ZrO_2 crucible volume. At 2100°C a larger dissolved volume was observed in the FZK test #4 with 574 s melt duration than that in the tests #7 and #8, despite longer interaction

times in the latters: 750 s and 1778 s; this can be explained only by uncertainties in the temperature measurements discussed in Section 2.2;

3. The extent of ZrO_2 crucible dissolution strongly depends on the ratio of the interaction surface (*S*) to the melt volume (*V*) and crucible wall thickness.

The dissolved mass of ZrO_2 crucible can be calculated and related to the initial Zircaloy melt charge. The derived ZrO_2 dissolution rate by molten Zircaloy is represented by the Arrhenius plot (Fig. 51). The variable parameter for this plot is the ratio *S/V* between the melt-crucible interaction surface and the initial melt volume. There are three different values of *S/V* - the ratio for AECL crucibles (695 m^{-1}), the ratio for FZK crucibles without bottom isolation (370 m^{-1}) and the ratio for FZK crucibles with bottom isolation (230 m^{-1}). The plot in Fig. 51 has no quantitative significance (too few experimental points), but clearly shows the tendency that the rate of dissolution depends strongly on the geometry factor *S/V*: the higher the *S/V* ratio the smaller the crucible dissolution rate.

Table 4 shows the relative dissolution values for the FZK tests: the relative dissolved crucible volume (with respect to the initial volume of liquid Zircaloy) and the relative height of dissolved crucible wall (with respect to the initial height of liquid Zircaloy). The results in Table 4 show that after 100 s there is no dependence of dissolved crucible volume and of dissolved crucible wall height on the interaction time.

3.5. Oxygen concentration in Zircaloy melt

The knowledge of the dissolved mass M_{dis} of the crucible (Table 4) allows calculation of the dissolved oxygen mass:

$$M_{Odis} = (1-\alpha)\cdot M_{dis}\cdot 32/(32+91) + \alpha\cdot M_{dis}\cdot 16/(16+40), \quad (6)$$

where $\alpha = 0.042$ is the weight part of the CaO in the dissolved crucible.

The mass M_{Odif} of oxygen diffused from the undissolved part of the crucible to the melt can be calculated from the following correlation:

$$O/100 = (M_{odif} + M_{Odis})/(M_{Zry} + M_{dis} + M_{Odif}) \quad (7)$$

where *O* is known from Eq. (4), M_{dis} is the calculated dissolved mass of crucibles (Table 3), and M_{Zry} is the mass of Zircaloy charges (Table 1). Therefore the diffused mass of oxygen is

$$M_{Odif} = ((M_{Zry} + M_{dis})\cdot O/100 - M_{Odis})/(1 - O/100). \quad (8)$$

The calculation results are presented in Table 6. One can see that the larger part of the oxygen in the melt is determined by the oxygen diffusion at test duration of more than 500 s.

3.6. Comparison of the chemical and image analyses results

The comparison between the image analysis results of the element content in the melt with the exact results of the chemical analysis allows to get information on the

precision of the image analysis method. Moreover, such a comparison allows to make statements about some physical-chemical processes during dissolution of ZrO_2.

3.6.1. Oxygen in the melt

The correlation between the estimation of the oxygen content in the melt by the image analysis (Table 6) and chemical data (Table 3) is depicted in Fig. 52. A linear fit for the two data sets shows a good agreement between the results of both methods. Therefore, the image analysis method gives quite satisfactory quantitative results.

3.6.2. Calcium in the melt

On the basis of the calculated dissolved crucible mass M_{diss} (Table 5) taking into account that the crucible material contains 4.2 wt.% of CaO, one can calculate the dissolved mass of Ca:

$$M_{Ca} = 0.042 \cdot M_{dis} \cdot 40/(40+16). \quad (9)$$

Thus, the image analysis allows to calculate how many calcium was transported from the dissolved crucible wall to the melt. The comparison between the image analysis and the chemical results for the calcium content in the frozen melt presented in Table 8, shows a large deficit of calcium in the solidified melt. The probable explanation is the evaporation of calcium from the melt: the formation enthalpy for CaO at 2300K is ΔG_{CaO} = -311 kJ/mol and is less than the corresponding value for ZrO_2: $\Delta G_{1/2ZrO2}$ = -337 kJ/mol, i.e. in the melt CaO can be reduced to the metallic calcium. The boiling temperature for the Ca is 1500°C - much lower than the test temperatures. The evaporation of Ca from the melt was proven by X-ray - fluorescent examinations. This means, the Ca content in the melt cannot be used as a measure to determine the extent of ZrO_2 crucible dissolution.

3.7. Comparison of the dissolution processes of UO_2 and ZrO_2

The above described method of image analysis for determination of the dissolved crucible wall volume was applied to the analysis of the AECL tests performed with the UO_2 crucibles [4]. Fig. 53 illustrates a good correlation between the estimation of dissolved uranium on the basis of image analysis and results of chemical analysis performed by AECL. The quantitative results of the calculated dissolved volumes of UO_2 crucibles are summarised in Table 9. Table 9 shows also the oxygen content in the melt based on these calculations. The comparison of the data in Table 9 with corresponding data for ZrO_2 dissolution (Table 7) shows that the diffused oxygen from the undissolved UO_2 crucible to the melt is higher than that from the undissolved ZrO_2 crucible.

The comparison of the dissolution rates for UO_2 and ZrO_2, depicted in Fig. 54 (data from Table 6 for ZrO_2 and Table 9 for UO_2) shows that under the same conditions (geometry and temperature) the dissolution process is more rapid for UO_2 than for ZrO_2.

The influence of the uranium presence in the (U,Zr,O) melt on the dissolution rate of zirconia should be investigated in the future tests. The first results on the simultaneous dissolution tests [4] (molten Zry in the UO_2 crucible with a ZrO_2 rod in

the centre) show that under the same conditions the dissolved volume of the ZrO_2 rod is much higher than that in the above described FZK tests.

3.8. Summary of the test results

- Different physical-chemical phenomena determine the character of the dissolution process: the oxygen diffusion from the crucible matrix to the melt and the convection stirring in the melt.
- There is practically no ZrO_2 dissolution at temperatures below 2000°C.
- Oxygen in the melt delivered from the dissolved part of the crucible makes up a smaller part of the total oxygen content in the melt. A larger part of oxygen in the melt in the experiments with duration more than 500 s is delivered by the solid state diffusion from the undissolved crucible matrix into the melt.
- The formation of interconnected α-Zr(O) precipitates along the grain boundaries of the ZrO_2 crucible matrix indicates that oxygen diffuses significantly along the grain boundaries of ZrO_2.
- An yttria (Y_2O_3) disc on the ZrO_2 crucible bottom prevents the chemical interactions between the Zircaloy melt and ZrO_2 crucible. There is only a small dissolution of the upper Y_2O_3 disc edge. The yttrium traces in the ceramic phase of the melt along the melt-crucible boundary and in the upper part of the melt can be explained as a result of the melt convection.
- In the FZK tests the oxygen content in the melts did not achieve the maximum solubility of oxygen in the liquid Zry and the ZrO_2 precipitates in the melts formed on cool down only. The oxygen content in the melt in the end of the AECL tests corresponds to the two-phase area (liquid + cub. ZrO_2) in the binary Zr-O phase diagram. Therefore, a part of the ZrO_2 precipitates formed already at temperature.
- The growth rates of the ceramic phase precipitates in the α-Zr(O) melt and of the transition layer between the melt and the ZrO_2 crucible wall are higher at higher ratios of the interaction surface to the initial melt volume (*S/V* ratio).
- The crucible dissolution rate depends on the dimensions of the ZrO_2 crucible test specimens: the smaller the ratio between the interaction surface and the melt volume the higher the dissolution rate.
- The analyses of KfK, AECL and FZK results show, that the dissolution (erosion) process of the crucibles takes place within the first 500 s of the interaction. In the KfK and AECL tests growth of the ZrO_{2-x} interface layer (corrosion) commences after this time interval, whereas in the FZK tests only diffusion of oxygen from the crucible matrix to the melt was observed.

3.9. Test conclusions

The results of the investigations show a strong influence of the geometry of the crucibles (the relationship between an initial melt volume *V* and a melt-crucible interaction surface area *S*) on the kinetics of the dissolution of the zirconia crucibles by molten Zircaloy. The larger the *S/V* ratio the faster the melt saturation with oxygen takes place and the earlier termination of the crucible wall dissolution process occurs. For a comprehensive quantitative kinetic description of the dissolution phenomena, additional tests with a wider range of interaction times, various inner crucible radii and different initial oxygen contents in the Zircaloy melt are necessary.

4. Modelling of ZrO_2 dissolution by molten Zircaloy

The following section gives brief generalised descriptions of the ZrO_2 dissolution tests modelling. Full details are provided in the four IBRAE interim reports that have been sent previously to FZKA [7-10].

4.1. Basic model

The model of ZrO_2 dissolution is essentially based on the theoretical consideration of the ZrO_2/(Zry melt) interactions proposed in the authors' paper [5] for modelling KfK tests [1,2].

The experimental data [1,2] on the ZrO_2 crucible wall dissolution by molten Zry had only preliminary character, however, unambiguously demonstrated that the ZrO_2 dissolution rates at high temperatures ($T \geq 1900°C$) were significant and comparable with the UO_2 dissolution rates measured in the analogous crucible tests [11]. Besides, it was observed in these tests that the composition of the solidified melt was spatially homogeneous, analogously to the observations in the UO_2 dissolution tests. This implies that convective mixing of the melt occurs also in the course of ZrO_2 dissolution by molten Zr. In the UO_2 dissolution tests a mass transfer in the liquid phase could be produced by natural convection driven by the density differences in the melt (due to the large weight of U atoms in comparison with Zr atoms). In the ZrO_2 dissolution tests the convective stirring of the melt apparently occurs only owing to high temperature gradients in the crucible system. [As mentioned above in Section 2.2, the temperature difference between crucible walls and the melt attained 50 - 100 K in the crucible tests]. For this reason, the mass transfer coefficient in the melt was expected to be much smaller in the ZrO_2 dissolution tests in comparison with the UO_2 dissolution tests.

On the other hand, some differences exist between the two dissolution processes. Additional visual analysis of the post-test photographs of the specimens obtained in [1] (see Figs. 40 - 42) apparently evidences that after cessation of the dissolution process within ~ 500 s (termed hereafter the erosion stage) the propagation of the solid/liquid interface changes its direction from inward to outward, that is the erosion of the ZrO_2 turns to the corrosion.

Such a behaviour has a quite natural explanation. As it will be shown below, the direction and velocity of the interface propagation is determined by the oxygen flux matching condition at this interface. In the initial stage of solid/liquid interactions the oxygen mass flux in the convectively stirred melt is rather large in comparison with that in the solid phase; for this reason, a high dissolution rate proportional to the difference between the two fluxes prevails. Since the melt approaches the saturation composition as a result of the dissolution process, the convection flux reduces and eventually matches the oxygen flux in the ZrO_2. This moment corresponds to the cessation of the erosion stage. After this moment the flux in the solid phase becomes larger than that in the melt, since reduction of the latter with time is much quicker. In accordance with the flux matching equation the velocity of the interface propagation changes its sign and the corrosion stage commences. For these reasons, in the following calculations the both stages are represented by a single curve for the "dissolved wall thickness" which becomes positive in the erosion stage and negative in the corrosion stage.

Under the crucible test conditions melt saturation may be achieved during a finite time interval and the growth of the interface oxide layer may be accompanied by the precipitation of ceramic ZrO_2 particles in the bulk of the melt at a late stage of the

corrosion stage (see below Section 4.6). In the current calculations the precipitation process is not considered.

Equations, describing (molten Zr)/ZrO_2 dissolution process, express various elements (oxygen, zirconium) mass balances and interface oxygen flux matches [5] in the one-dimensional (1-d) geometry: plane or cylindrical (see Fig. 55). In the frames of the convective mixing model after some transformations, these equations take the form:

$$\frac{dC_O(B)}{dt} = \frac{(k_O + \partial r_2/\partial t)[C_O(I) - C_O(B)]}{r_2^{\,L} - r_1^{\,L}}(2r_2)^{L-1}, \tag{10}$$

$$\frac{dr_2}{dt} = \frac{D_O^{(ZrO_2)}\left.\frac{\partial \varphi_O}{\partial r}\right|_{II} - k_o[C_o(I) - C_o(B)]}{C_o(I) - \varphi_o(I)\tilde{B}}, \tag{11}$$

$$\frac{dr_3}{dt} = (1-\tilde{B})(\frac{r_2}{r_3})^{L-1}\frac{dr_2}{dt}, \tag{12}$$

where r_1 and r_2 are the melt boundaries positions; r_3 is the ZrO_2 outer boundary position; $\tilde{B} = C_{Zr} / \rho_{Zr}$ is the zirconium molar density ratio in the liquid (molten Zr) and solid (ZrO_2) phases; $C_O(B)$, $C_O(I)$ are the bulk and interface values of oxygen concentration in the liquid Zr, respectively; $\varphi_O(r)$ is oxygen concentration in the solid phase and $\varphi_O(I)$ is its interface value at the lower ZrO_{2-x} phase boundary. Eqs. (10) - (12) are written in the general form comprising cylindrical (L=2) and plane geometry (L=1).

Oxygen radial distribution in zirconia $\varphi_O(r)$ and relevant boundary gradient $(\partial\varphi_O/\partial r)|_{r=r2}$ at the (molten Zr)/ZrO_2 interface are found by the solution of a moving boundary diffusion problem:

$$\frac{\partial \varphi_o}{\partial t} + V\frac{\partial \varphi_o}{\partial r} = \frac{1}{r}\frac{\partial}{\partial r}\left(rD_i\frac{\partial \varphi_o}{\partial r}\right), \tag{13}$$

with boundary conditions $\varphi_O(r=r_2,t)=\varphi_O(I)$ and $(\partial\varphi_O/\partial r)|_{r=r2}=0$, corresponding to the conditions of the dissolution experiments in an inert atmosphere.

The model includes parameters such as k_O, $D_O^{(ZrO2)}$, $C_O(I)$ which are poorly known, especially at temperatures above 2000°C. These parameters could be derived by fitting experimental and theoretical data.

In order to simulate the crucible tests without bottom isolation (KfK [1], AECL [3] and FZK) in the framework of the 1-d model, a special procedure for calculation of linear dimensions (internal and external radii) of the effective 1-d cylinder was applied (Fig. 55). Namely, the internal radius $R_{in} = r_2(t=0)$ of the cylinder was chosen to provide the same S/V ratio as in the real crucible (i.e. $R_{in} = 2S/V$), whereas the external radius $R_{ex} = r_3(t=0)$ was chosen to provide the same ratio V_{cr}/V_{liq}, where V_{cr} is the total volume of the interacting part of the crucible (bottom + wetted parts of the walls), V_{liq} is the melt volume. These two conditions afforded an appropriate treatment of the mass transfer process in the melt and oxygen diffusion in the crucible in the course of the interactions.

4.2. Analysis of the previous KfK tests

In the experiments [1] dissolution of the inner walls of ZrO_2 crucibles by molten Zircaloy was studied at temperatures between 2000 and 2400°C. The data on weight content of ZrO_2 in the melt were obtained by comparison of a cooled melt microstructure with those of previously prepared (Zry melt)/ZrO_2 standards. This procedure generally neglected additional amounts of oxygen in the melt transported from the oxide by the diffusion mechanism. For this reason, interpretation of the obtained data in terms of dissolved ZrO_2 in [1] might be inaccurate. However, these data can be correctly re-interpreted by the present model taking into account the oxygen diffusion fluxes in the solid phase. Indeed, the determined in [1] quantity W_{ZrO_2} (recalculated from the observed ceramic phase fraction in the solidified melt) can be uniquely connected with the molar oxygen density $C_O(B)$ in the liquid phase by the formula:

$$W_{ZrO_2} = \frac{0.5C_o(B)(\mu_{Zr} + 2\mu_o)}{C_{Zr}\mu_{Zr} + C_o(B)\mu_o}, \qquad (14)$$

where μ_O (μ_{Zr}) is the oxygen (zirconium) molar weight, C_{Zr} - the zirconium molar density in the melt. Hence, experimental results [1] can be treated within the framework of the present model in order to extract necessary parameters. The density of the stabilised zirconia was taken 75%TD in accordance with the crucible material properties; the lower oxygen concentration in zirconia (attained at the interface) was taken ≈ 60 at.% in accordance with the EDX measurements performed in the new FZK test series with a similar crucible material (see Figs. 34 - 35).

Calculated by the numerical model and measured values of weight content of ZrO_2 in the melt are presented in Fig. 56. Fitted parameters are shown in Table 10. Temperature dependence of mass transfer coefficient is well described by the Arrhenius equation:

$$k_O = 1.06\cdot10^7 \cdot\exp(-108436/RT)\ \text{cm/s},$$

where R = 1.987 cal/mol, T in K,

which fairly corresponds to the power dependence $k_O \propto D_{liq}^{3/4}$ (D_{liq} is the oxygen diffusion coefficient in the melt). As expected, the value of k_O in the ZrO_2 dissolution tests occurred to be much smaller than that in the UO_2 dissolution tests (which at 2000°C was estimated as ~ 10^{-2} cm/s [12,6], i.e. one order of magnitude larger).

Calculated magnitudes of the oxygen terminal solubility $C_O(I)$ in the liquid zirconium show a somewhat higher values in comparison with the previously published data [13], however, can be well confirmed by the new data (see below).

Oxygen diffusion coefficient in the stabilised ZrO_2 is described by the Arrhenius correlation:

$$D_O^{(ZrO2)} = 4\cdot\exp(-24000/T)\ \text{cm}^2/\text{s}.$$

The largest deviation of the calculated kinetic curves from the test data was attained at 2200°C after 600 s, however, this discrepancy was successfully eliminated (see an

arrow in Fig. 56) after additional image analysis of the corresponding KfK test sample microphotograph (see Section 3.4).

In order to further validate the model against the KfK data, the model predictions on the wall dissolution kinetics at various temperatures were compared with available KfK photographs of the crucible cross-sections (see Figs. 38 - 42). In these photographs one can clearly distinguish and estimate the depth of the wall dissolution and thickness of the interface corrosion layers formed at various times. Results of the calculations at four temperatures 1900, 2000, 2100 and 2200°C presented in Figs. 57 – 59, are in a good qualitative and quantitative agreement with the available photographs data. Indeed, at lower temperatures 1900 and 2000°C the model predicts no dissolution (erosion) process and a rather thick (~ 2 mm) corrosion layer after 120 min, in a fair agreement with observations. At higher temperatures 2100 and 2200°C the model predicts strong erosion (~ 1 mm) during the first 400 - 500 s, and a thick (~ 2 mm) corrosion layer after 120 min, also in a fair agreement with observations. Calculated oxygen content in the saturated melt (see Table 10) satisfactory corresponds to the new image analysis data (see Fig. 47) , which can be interpreted in the following way:

At 2000°C melt attains its saturation value (≈ 11 wt.% of oxygen) during ≈ 7200 s, whereas at higher temperatures the oxygen melt content slowly approaches the corresponding limiting values (≈ 14 wt.% at 2100°C and ≈ 15 wt.% at 2200°C) in the time interval 600 - 3600 s (in a fair agreement with calculations in Fig. 60), but then rather steeply increases and significantly exceeds these values in a late stage of the erosion process (3600 - 7200 s). A similar behaviour was observed in the subsequent experiments of AECL and FZK with smaller crucibles (see Sections 4.3 and 4.4) even more pronouncedly, and might be interpreted as the onset of the ceramic phase precipitation in the melt bulk. Possible reasons for such an oversaturation of the melt in the late stage of the corrosion process will be presented in Section 4.6.

In order to illustrate an important influence of the crucible wall thickness on the dissolution behaviour, the above presented calculations for the thick wall (5 mm) crucible are compared with calculations for a thinner wall (4 mm) crucible under the same conditions (T = 2200°C and the same *S/V* ratio) in Fig. 59. From these results it is clearly seen that a relatively small variation (within 20%) of the wall thickness (and thus reduction of the oxygen content in the crucible walls) changes the system behaviour drastically: the erosion depth is significantly increased, whereas the corrosion layer growth is suppressed completely in the new case.

4.3. Analysis of the AECL tests

The same model was applied without any additional tuning of the model internal parameters (such as mass transfer and diffusion coefficients and the oxygen terminal solubility in the liquid zirconium) for modelling the AECL tests [3] which were performed under identical conditions (2100 and 2200°C), but in smaller crucibles with larger material density (5.9 g/cm^3). Since the *S/V* ratio and wall thickness in these tests differed considerably from that in the KfK tests, the model predicts quite different behaviour in comparison with the previous case.

Indeed, as seen from Figs. 61 and 62 , in both temperature cases that model predicts a small erosion (≈ 0.2 mm) during the first ≈ 200 s of the interactions, and then a noticeable growth of the corrosion layer. Being compared with the available experimental data [3], these results demonstrate a very good agreement with the measurements in the first ≈ 1000 s of the interactions, however, at a later stage of the corrosion period the model overpredicts the corrosion layer thickness. Deviations

of the calculated kinetic curves from the experimental points in Figs. 61 and 62 occur practically simultaneously with the onset of the melt oversaturation detected in Fig. 46 (and corrected in Section 4.2), i.e. when the oxygen melt content exceeds ≈ 14 at.% at 2100°C and ≈ 15 at.% at 2200°C. This additionally confirms the above assumption (see Section 4.1) on the ceramic ZrO_2 phase precipitation in the melt bulk at a late stage of corrosion. Indeed, in this case the above presented model predictions for the corrosion layer thickness should be assigned to the overall volume of the ceramic phase (i.e. corrosion layer + precipitates, see Section 4.6 below) and for this reason, the model naturally overpredicts the corrosion layer thickness when the precipitation of the ceramic phase in the melt bulk is not taken into account.

4.4. Analysis of the FZK tests with small crucibles

The new FZK test series with small crucibles was performed under conditions similar to the previous AECL tests and with the same crucible dimensions, specially to reproduce the main qualitative observations of the previous tests. In order to avoid the melt transfusion from the top of the crucibles at a late stage of the interactions, the initial Zry charge volume was decreased in comparison with the AECL tests, thus, the *S/V* ratio was also decreased, correspondingly (see Section 3.4).

In this case the model predicts a similar to the previous case erosion behaviour during the first 100 - 200 s and a more rapid growth of the corrosion layer after this time interval (see Figs. 63 and 64). As in the previous case, the model well predicts the corrosion layer growth kinetics in the beginning (≈ 600 s), but overpredicts the layer thickness in the late stage of the corrosion period when melt oversaturation and precipitation of the ceramic ZrO_2 phase in the melt bulk commence (see Figs. 43 - 45).

4.5. Analysis of the FZK tests with large crucibles

The new FZK test series with large crucibles was performed under conditions similar to the previous KfK tests and with the same crucible dimensions (but with the higher crucible density, 93% TD). However, some tests were performed with the crucible cavity bottom isolation by Y_2O_3 discs, in order to reproduce the one-dimensional dissolution process typical for the fuel rod geometry, and to avoid the above described difficulties in modelling simultaneous dissolution of the crucible walls and bottom by the simplified one-dimensional model (see the end of Section 4.1).

For the tests without crucible bottom isolation performed at 2200°C, the model predicts a similar to the KfK test behaviour, however, with a somewhat smaller dissolution depth in the erosion stage (and a slower growth of the corrosion layer in the subsequent period) owing to the higher crucible material density. The model predictions for the dissolved wall thickness are in a reasonable agreement with the data at the two available time points ≈ 100 and 600 s, Fig. 65 .

For the tests with Yttria discs preventing the crucible bottom from interactions with the melt, calculations were performed in the one-dimensional geometry with the real internal and external radii of the crucible walls. A systematic temperature shift of about 100 K to lower temperatures was accounted for in the calculations in accordance with the above presented analysis of the test procedure in Section 2.2. Such temperature corrections allowed reasonable coincidence with the test data at two temperatures initially measured as 2100 and 2200°C but then assigned to 2000 and 2100°C, respectively (see Fig. 66 and 67).

Simulations of the FZK tests at 2300°C was not attempted, since practically all crucibles failed during the tests (with exception of a very short interaction time of ≈ 100 s), as it was also in the KfK tests.

4.6. Ceramic phase precipitation

In order to explain the reasons for the observed ceramic phase precipitation at a late stage of the crucible tests, one should take into account a significant temperature difference between the crucible walls (or bottom) and the melt. In accordance with the above presented data, this difference attained 50 - 100 K . Since the melt is well mixed in the crucible tests (probably, owing to this temperature difference) and thus has a homogeneous temperature and composition distribution in the melt bulk, a thin transition layer exists in the melt near to the interface in which temperature and concentration drops occur. The melt in the transition layer at the interface sustains the thermodynamically equilibrium state with the crucible wall. Owing to the temperature difference in the melt bulk and at the interface, this state differs from the saturation state in the melt bulk. For this reason, the concentration drop in the transition layer still exist even when the bulk of the melt attains the saturation level (corresponding to reduced temperature with respect to the wall), and thus oxygen supply from the walls to the melt bulk through the transition layer continues after the melt saturation attainment. In this situation the melt unavoidably becomes oversaturated (and falls in the two-phase region of the phase diagram) and continues to consume oxygen until it completely precipitates into the ceramic phase (see Fig. 42).

Such a behaviour drastically differs from that under isothermal conditions. Indeed, under isothermal conditions the melt saturation state coincides with the melt/crucible equilibrium state sustained at the interface and, for this reason, oxygen flux through the transition layer disappears with the saturation approach.

In order to model the oxide layer growth accompanied by the ceramic phase precipitation in the melt bulk, one should generalise the above described model to consider the problem of the mass transfer through the two-phase zone. Such a general consideration was presented in the authors paper [6] for a similar case of the UO_2 crucible dissolution by molten Zry, where the flux matching conditions were combined with the mass conservation laws. However, the exact solution of the full problem was not searched in that paper owing to additional difficulties in the treatment of the mass convection problem (in comparison with the diffusion problem considered in the earlier authors' paper [14]). Instead of this, a simplified solution based on the mass balance equations with an additional assumption on the invariable $(U,Zr)O_{2-x}$ composition, was found. In the present case, there is no similar simplification of the problem, for this reason, only some general conclusions on the system behaviour might be drawn from the mass balance equations.

Under conditions of the ceramic phase precipitation, one should introduce in the mass balance equations a new variable of the total precipitates volume W in the melt (compare with [6]). As a result, it is straightforward to show in this case that the ordinary oxidation kinetics equation:

$$\partial L/\partial t = J^*/L(t), \qquad (15)$$

where $L(t)$ is the growing oxide layer thickness, $J^* \propto D_O^{(ZrO_2)} \Delta\rho_O$ characterises the solid state diffusion flux due to the oxygen concentration drop $\Delta\rho_O$ across the crucible wall, will be transferred in the new one (compare also with [4,5]):

$$\partial(W/S)/\partial t+\partial L/\partial t=J^*/L(t), \quad (16)$$

where S is the melt/solid interface area. It is clearly seen from Eq. (16) that the parabolic rate solution of Eq. (15), $L(T) \propto t^{1/2}$ is not anymore valid, since the oxygen flux from the solid is now consumed also by precipitates. This naturally results in a slower growth of the oxide layer thickness $L(T)$ which provides a barrier for the oxygen penetration, and for this reason, in a slower growth of this barrier. In its turn, this leads to the subsequent increase (in comparison with the ordinary case, Eq. (15)) of the total oxygen consumption by the growing ceramic phase (oxide layer + precipitates) and thus, to the increase of the total volume of the ceramic phase ($W + LS$) (in comparison with the ordinary case). In the limiting case of a very slow oxide layer growth, the oxygen flux does not anymore reduce with time leading to the linear increase of the ceramic phase volume with time (instead of the parabolic time law in the ordinary case).

Therefore, an important conclusion may be drawn that the total amount of the ceramic ZrO_2 phase formed under precipitation conditions in the oxidising melt might be significantly higher than that in the ordinary oxidation case. This conclusion can be applied to the interpretation of the oxidation kinetics and hydrogen generation in the QUENCH - 02 and 03 tests [15], where an extremely large amounts of hydrogen were produced in the course of molten Zry clad oxidation.

4.7. Qualitative analysis of melt oxidation in the bundle QUENCH tests

A visual analysis of available photographs of the bundle cross-sections (see Fig. 68) shows that extended areas of the molten material were formed in the QUENCH-02 test [15] at different elevations. At lower elevations (e.g. 850 mm) where the melt was formed later (and thus was oxidised for a shorter period of time), such «molten pools» consist mainly of pure metal (Zr,O) melts with different oxygen contents and decompose into mixtures of α-Zr(O) and ZrO_2 phases on cool-down (see Fig. 69). Along the periphery the molten pools are confined by relatively thin (up to 1 mm) and homogeneous oxide layers which form some kind of a thin-walled zirconia crucible for each molten pool (see Fig. 69). At higher elevations oxidation time of the melt was longer and in many positions the melt was completely converted into ceramic ZrO_2 phase (see Fig. 68). A typical example of completely oxidised melt at elevation 950 mm is presented in Fig. 70, where one can clearly distinguish thin peripheral oxide layers and the bulk ceramic phase.

In Fig. 71 a set of micrographs of the solidified melts at different locations of the QUENCH-02 bundle cross-sections, is presented. From this figure one can clearly see that the amount of ceramic phase in the refrozen melts smoothly varies in a wide range corresponding to the different oxygen contents in the melt. Assuming that temperature did not exceed 2200°C in this test (in accordance with experimental data [15]), one can conclude that at all presented photographs the melt content corresponds to the two-phase region in the equilibrium phase diagram, Fig. 46 , i.e. some of the ceramic particles were already formed at temperature. It is also clear that in the last two photographs the melt was completely converted into ceramic phase at temperature via formation and growth of the ceramic precipitates in the melt bulk. As mentioned above, this region can be clearly distinguished from the peripheral oxide layers (Fig. 70), and the visual evaluation of its volume (Fig. 68) confirms that the most part of the ceramic ZrO_2 phase was formed in the course of the precipitation rather than the peripheral oxide layer growth.

Such a behaviour of the melt in the molten pools is qualitatively similar to the one observed in the zirconia crucible dissolution tests (compare Figs. 42 and 71), and, therefore, might be described by the same material interaction model. In particular, the important conclusion derived from the crucible tests analysis, that the total amount of the ceramic ZrO_2 phase formed under precipitation conditions in the oxidising melt might be significantly higher than that in the ordinary oxidation case, becomes valid also for the correct interpretation of the QUENCH tests.

It is proposed that the present dissolution model being implemented in the SVECHA/QUENCH code (see Part II) and further developed to account for the precipitation process, will allow adequate description of the melt oxidation kinetics and hydrogen generation in the QUENCH tests.

4.8. Modelling conclusions

- The present model qualitatively and quantitatively correctly describes different behaviour of ZrO_2 dissolution in the three test series: KfK, AECL and new FZK tests.
- Depending on temperature, crucible dimensions (*S/V* ratio and wall thickness) and geometry (with/without bottom isolation), two stages (erosion and corrosion) or only one stage (erosion) of the crucible/melt interactions are correctly predicted by the model.
- The newly developed model of ZrO_2 dissolution by molten Zry is ready for implementation in the integral CD codes.
- Being implemented in the single-rod version of the SVECHA code, the model allows simulations of the new FZK tests on cladding oxide shell failure (see Part II).
- The further development of the model should include consideration of the ceramic melt precipitation in the melt bulk that will allow adequate description of the melt oxidation kinetics and hydrogen generation in the QUENCH tests.

Acknowledgements

The authors thank Mr. H. Metzger for the metallographic preparation of the specimens and Mr. J. Burbach for the SEM examinations and Dr. Ch. Adelhelm for the conduct of the chemical analysis.

This report was prepared for the Commission of the European Communities within the 4th Framework Programme on Nuclear Fission Safety in part-fulfillment of Contract Number FI4S-CT96-0032 (Corium Interactions and Thermochemistry).

References:

1. Hofmann, Ch. Adelhelm, E. Garcia, M. Markiewicz, J. Burbach, G. Gussmann, K. Kurz and H. Metzger, Chemische Auflösung von festem ZrO_2 durch geschmolzenes Zircaloy-Hüllmaterial, Kernforschungszentrum Karlsruhe Report No. KfK-4100. September 1987
2. P. Hofmann, S. Hagen, G. Schanz and A. Skokan, Nuclear Safety, 87(1989)146.
3. P.J. Hayward and I.M. George, Dissolution of ZrO_2 in Molten Zry-4, - J.Nucl.Mater., 265(1999)69.
4. M.S. Veshchunov, A.V. Berdyshev, A.V. Palagin, Theory of simultaneous dissolution of UO_2 and ZrO_2 by molten Zircaloy in oxidizing atmosphere and its application for description of chemical interactions of relocating melt, - Preprint IBRAE-96-10, Moscow 1996.
5. M.S. Veshchunov, A.V. Berdyshev, Modeling of chemical interactions of fuel rod materials at high temperatures. Part 1: Simultaneous dissolution of UO_2 and ZrO_2 by molten Zircaloy in an oxidizing atmosphere, - J.Nucl.Mater., 252(1997)98.
6. M.S.Veshchunov and P.Hofmann, J.Nucl.Mater. 209(1994)27.
7. A.V.Berdyshev, M.S.Veshchunov, 1st Interim Report, 1997 May, unpublished
8. A.V.Berdyshev, M.S.Veshchunov, 2nd Interim Report, 1997 December, unpublished.
9. A.V.Berdyshev, M.S.Veshchunov, 3rd Interim Report, 1998 June, unpublished.
10. A.V.Berdyshev, M.S.Veshchunov, 4th Interim Report, 1998 December, unpublished.
11. P.Hofmann, H.Uetsuka, A.N.Wilhelm and E.A.Garcia, Proc.Int.Symp. on Severe Accidents in Nuclear Power Plants, Sorrento, Italy, March 21-25, 1988, IEAE-SM-296/1, p.3.
12. K.T.Kim and D.R.Olander, J.Nucl.Mater. 154(1988)85, 102.
13. E. Gebhardt, G.Elssner, Untersuchungen im System Zirconium -Sauerstoff, Teil 2, - J. Nucl. Mater., 4(1961)255.
14. M.S.Veshchunov and P.Hofmann, J.Nucl.Mater. 210(1994)11.
15. P. Hofmann, C. Homann, W. Leiling, A. Miassoedov, D. Piel, L. Schmidt, L. Sepold, M. Steinbrück. Experimental and Calculational Results of the Experiments QUENCH-02 and QUENCH-03, FZKA 6295, Forschungszentrum Karlsruhe, 1999

Table 1
Pre-test material dimensions and weights

Test No.	[1]O.D. mm	*Post-test O.D., mm*	[2]I.D. mm	Height mm	*Post-test Height, mm*	[3]Depth mm	Cruc. wt g	Cruc. Dens. g/cm³	Zry wt g	Mass ratio
4	27.00	*26.8*	17.60	32.35	*32.15*	27.65	60.5739	5.214	10.0031	6.056
5	26.85	*26.85*	17.45	32.30	*32.15*	27.60	60.3913	5.304	10.0255	6.024
7	26.95	*26.95*	17.50	32.30	*32.1*	27.55	60.6446	5.282	10.026	6.049
8	26.95	*26.95*	17.55	32.20	*32.05*	27.65	60.5636	5.259	10.0207	6.044
11	27.00	*26.8*	17.70	32.35	*32.05*	27.50	60.6695	5.253	10.0226	6.053
12	26.85	*26.85*	17.60	32.20	*32.1*	27.55	60.7907	5.255	10.0282	6.062
13	26.90	*26.8*	17.45	32.20	*32.15*	27.50	60.8566	5.253	10.032	6.066
14	27.05	*27.1*	17.55	32.20	*32.15*	27.50	60.8629	5.249	10.0199	6.074
15	26.90		17.55	31.95		27.30	60.737	5.240	10.0457	6.046
16	27.00		17.55	32.25		27.85	60.8214	5.242	10.0192	6.070
17	27.05		17.60	32.3		27.60	60.7997	5.213	10.0238	6.066
18	27.05		17.60	32.3		27.60	60.8328	5.243	10.0354	6.062
19	27.05		17.40	32.2		27.45	60.9791	5.289	10.0352	6.077
24	26.95	*26.95*	17.50	32.15	*31.95*	27.30	60.914	5.261	10.0123	6.084
25	26.95		17.55	32.3		27.60	61.0789	5.240	10.037	6.085
26	26.95		17.55	32.4		27.60	60.8075	5.247	10.0515	6.050
*FA1	13.7		6.45	16.65		13.3	11.8392	5.932	1.340	8.86
FA2	13.8		6.4	16.5		13.4	11.7365	5.859	1.340	8.74
FA3	13.8		6.4	16.35		13.3	11.7365	5.880	1.339	8.78

[1]crucible outer diameter; [2]crucible inner diameter; [3]crucible cavity depth
*FA - FZK tests with AECL crucibles

Table 2
Dissolution test parameters

Test No.	Pyrometer temper., °C	Melt duration, s	Isothermal time, s	Crucible bottom	Comments
4	2100	574	570	Y_2O_3	OK
5	2100	101	90	Y_2O_3	OK
7	2100	750	740	Y_2O_3	OK
8	2100	1778	1770	Y_2O_3	OK
11	2200	590	567	Y_2O_3 inclined	OK
12	2200	587	552	no Y_2O_3	OK
13	2200	106	85	Y_2O_3	OK
14	2200	102	93	no Y_2O_3	OK
15	2200	1830	1758	Y_2O_3	crucible dissolved through
16	2200	1835	1762	Y_2O_3	crucible dissolved through
17	2200	925	857	Y_2O_3	crucible dissolved through
18	2200	625	553	Y_2O_3	crucible dissolved through
19	2200	1830	1758	no Y_2O_3	crucible dissolved through
24	2300	121	67	no Y_2O_3	OK
25	2300	345	252	no Y_2O_3	crucible dissolved through
26	2300	227	126	no Y_2O_3	crucible dissolved through
FA1	2100	1820	1568	no Y_2O_3	OK
FA2	2100	610	555	no Y_2O_3	OK
FA3	2200	1220	1139	no Y_2O_3	OK

Table 3

Chemical analysis results* of the frozen melt zones of the FZK tests

Element	Zry-Charge	Initial ZrO_2 Tiegel	Melt 4	Melt 5
O	0.135 ± 0.015		9.81 ± 0.26	3.63 ± 0.04
N	0.007 ± 0.005		< 0.04	< 0.04
Fe	0.221 ± 0.001	0.039 ± 0.004	0.181 ± 0.001	0.204 ± 0.003
Cr	0.105 ± 0.001		0.086 ± 0.001	0.103 ± 0.001
Y	< 0.002	0.0079 ± 0.0001	0.019 ± 0.002	0.038 ± 0.019
Sn	1.525 ± 0.011	<0.04	1.221 ± 0.015	1.424 ± 0.017
Ca	< 0.005	3.632 ± 0.014	0.069 ± 0.003	0.015 ± 0.006
Hf	< 0.005	1.386 ± 0.004	0.202 ± 0.0005	0.074 ± 0.001
Ti		0.069 ± 0.0005		
Al		0.049 ± 0.001		

Results in wt%

Element	Melt 8	Melt 12	Melt 13	Melt 14	Melt 24
O	11.27 ± 1.00	13.25 ± 0.82	8.57 ± 0.06	7.30 ± 0.22	12.40 ± 0.45
N	< 0.04	0.063 ± 0.020	< 0.05	0.083 ± 0.027	< 0.05
Fe	0.195 ± 0.004	0.123 ± 0.001	0.180 ± 0.001	0.194 ± 0.004	0.126 ± 0.001
Cr	0.096 ± 0.0005	0.058 ± 0.001	0.075 ± 0.0005	0.081 ± 0.001	0.049 ± 0.0005
Y	0.049 ± 0.023	0.0026±0.0001	0.102 ± 0.008	< 0.002	0.0040±0.0002
Sn	1.405 ± 0.015	0.910 ± 0.020	1.111 ± 0.013	1.197 ± 0.032	0.735 ± 0.007
Ca	0.019 ± 0.002	0.236 ± 0.004	0.162 ± 0.006	0.152 ± 0.008	0.960 ± 0.030
Hf	0.132 ±0.002	0.319 ± 0.0005	0.297 ± 0.001	0.231 ± 0.003	0.571 ± 0.002

Results in wt%

Table 4

Phases areas distribution in the solidified melt as result of image analysis

Melt phase analysis for KfK-tests (1987)

No	T°C	t, s	Ceramic, %	α–Zr(O), %	microvoids, %
LV111	2000	1200	0	100	0
LV112	2000	3600	26	68	6
LV131	2000	7200	24	64	12
LV113	2100	60	10	89	1
LV114	2100	180	23	77	0
LV115	2100	600	42	54	4
LV127	2100	1800	42	50	8
LV126	2100	3600	41	45	14
LV128	2100	7200	62	27	11
LV133	2200	60	7	88	5
LV121	2200	180	34	66	0
LV123	2200	600	46	52	2
LV124	2200	1800	60	34	6
LV132	2200	3600	51	40	9
LV134	2200	7200	70	22	8
LV137	2300	60	48	51	1
LV125	2300	180	54	45	1

Melt phase analysis for AECL-tests (1997)

No	T°C	t, s	Ceramic, %	α–Zr(O), %	microvoids, %
Z-10	2000	146	0	97	3
Z-2	2000	553	19	78	3
Z-9	2000	1506	21	67	12
Z-8	2000	3615	20	38	42
Z-6	2100	116	20	79	1
Z-4	2100	601	35	57	8
Z-22	2100	1490	40	43	17
Z-23	2100	3585	59	28	13
Z-15	2200	136	28	53	19
Z-11	2200	612	37	43	20
Z-12	2200	1197	41	26	33
Z-21	2200	1787	46	15	39
Z-19	2300	187	42	38	20
Z-20	2300	599	49	25	26
Z-18	2300	1195	62	10	28
Z-16	2300	1798	57	14	29

Melt phase analysis for FZK-tests (1998, 1999)

No	T°C	t, s	ceramic, %	α–Zr(O), %	Microvoids, %	Y_2O_3 bottom
5	2100	101	0	100	0	+
4	2100	574	14	86	0	+
7	2100	750	13	87	0	+
8	2100	1778	19	81	0	+
13	2200	106	10	90	0	+
14	2200	102	4	96	0	-
12	2200	587	39	53	8	-
24	2300	121	32	65	3	-
FA1	2100	1820	62.9	28.1	8	-
FA2	2100	610	38.9	49.5	11.5	-
FA3	2200	1220	63.4	19.8	16.8	-

Table 5

Image analysis results:

dissolved crucible volume and phase area distribution in the solidified melt cross-section

FZK tests(mass ratio ZrO_2/Zry=6.1)
Interaction surface area to volume ratio S/V=230m^{-1}\370m^{-1} (with\without Y_2O_3 disc)

Test conditions				Wall and bottom dissolution values						Melt phase	
No	T °C	Time s	Y_2O_3	Wall depth mm	Bott. depth mm	Wall volume mm^3	Bottom volume mm^3	Diss. mass g	ZrO_2/(Zry+ZrO_2) wt%	Ceram. phase %	α-Zr(O) phase %
5	2100	101	+	0.33		179		0.95	8.6	0	100
4	2100	574	+	0.63		344		1.79	15.2	14	86
7	2100	750	+	0.49		256		1.35	11.9	13	87
8	2100	1778	+	0.44		250		1.32	11.6	19	81
13	2200	106	+	1.09		584		3.07	23.4	10	90
14	2200	102	-	0.47	0.77	268	166	2.28	18.5	4	96
12	2200	587	-	0.65	0.62	333	108	2.32	18.8	41.8	58.2
24	2300	121	-	1.28	1.51	886	314	6.31	38.8	32.5	67.5

AECL tests(mass ratio ZrO_2/Zry=5.75)
Interaction surface area to volume ratio S/V=695m^{-1}

Test conditions			Trans. layer ZrO_{2-x} mm	Wall and bottom dissolution values						Melt phase	
No	T °C	Time s		Wall depth mm	Bott. depth mm	Wall volume mm^3	Bottom volume mm^3	Diss. mass g	ZrO_2/(Zry+ZrO_2) wt%	Ceramic phase %	α-Zr(O) phase %
6	2100	116	-							20	80
4	2100	601	0.63	0.12	0.76	30	21	0.30	13.0	38	62
22	2100	1490	1.27	0.09	0.71	24	19	0.25	11.1	48	52
23	2100	3585	1.58	0.17	1.05	55	32	0.50	19.6	68	32
15	2200	136	-							35	65
11	2200	612	0.69	0.24	1.08	71	34	0.60	23.1	46	54
12	2200	1197	1.00	0.09	0.64	24	18	0.25	10.8	61	39
21	2200	1787	1.13	0.17	0.76	48	22	0.41	16.7	75	25
19	2300	187	0.17							53	47
20	2300	599	0.51	0.56	1.32	159	40	1.15	36.2	66	34
18	2300	1195	0.68	0.5	1.45	143	44	1.09	34.5	86	14
16	2300	1798	0.67	0.48	1.17	134	36	0.99	32.7	80	20

Table 6

Image analysis results. Relative parameters of the dissolution process

Test No	Tempera-ture °C	Melt duration s	S/V for melt 1/m	V_{diss}/V_{Zry}	H_{diss}/h_{Zry}	Oxygen in the melt at%
5	2100	101	229	0.10	1.3	
4	2100	574	227	0.20	1.3	35.8
7	2100	750	229	0.15	1.2	35.2
8	2100	1778	228	0.14	1.3	38.3
14	2200	102	368	0.25	1.4	30.2
12	2200	587	368	0.25	1.3	48.2
13	2200	106	229	0.34	1.3	33.6
24	2300	121	368	0.70	1.6	44.5

V_{diss} - dissolved volume of crucible; **V_{Zry}** - initial volume of molten Zircaloy

H_{diss} - maximal height of dissolved part of the crucible; **h_{Zry}** - initial height of the molten Zircaloy

Table 7

Image analysis results. Oxygen in the melt as result of two processes: dissolution of crucible material and oxygen diffusion from undissolved crucible matrix to the melt

Test No	Tempera-ture °C	Time S	S/V 1/m	$ZrO2_{dis}$ g	O_{dis} g	O in melt wt%	O_{dif} g	$O_{dif}+O_{dis}$ g	$O_{dif}/(O_{dif}+O_{dis})$ %
5	2100	101	229	0.95	0.25				
4	2100	574	227	1.79	0.47	8.9	0.64	1.11	58
7	2100	750	229	1.35	0.35	8.7	0.70	1.05	66
8	2100	1778	228	1.32	0.34	9.8	0.86	1.20	71
14	2200	102	368	2.28	0.59	7.1	0.29	0.89	33
13	2200	106	229	3.07	0.80	8.2	0.29	1.09	27
12	2200	587	368	2.32	0.60	14.1	1.32	1.92	69
24	2300	121	368	6.33	1.65	12.4	0.42	2.06	20

Table 8

Calcium content: image and chemical analysis

Test No	Temperature °C	Time s	S/V 1/m	Ca_{dis}, image anal., wt%	Ca in melt, chem., wt%	Evapor. Ca, wt%	Evapor. Ca, g
5	2100	101	229	0.26	0.015	0.24	0.027
4	2100	574	227	0.46	0.069	0.39	0.046
8	2100	1778	228	0.35	0.019	0.33	0.037
14	2200	102	368	0.56	0.152	0.40	0.050
13	2200	106	229	0.70	0.162	0.54	0.071
12	2200	587	368	0.56	0.236	0.33	0.040
24	2300	121	368	1.16	0.960	0.20	0.033

Table 9
Image analysis results for UO_2 dissolution tests

Test No	Wall Dissolution V_W , mm³	Bottom dissolution V_B, mm³	Volume ratio $(V_W + V_B)/V_{Zry}$	Cruc. wall Thickness µm	H_{diss}/h_{Zry}	O_{dif}/O_{melt} %
HF-13	784	164	0.57	3831	1.67	31
HF-6	481	170	0.39	4236	1.51	18
HF-12	766	153	0.55	3947	1.72	38
HF-7	846	179	0.61	3760	1.69	24
HF-11	1232	270	0.89	3531	1.86	22
HF-8	804	164	0.58	3970	1.68	23
HF-9	799	217	0.61	3977	1.76	28
HF-1	971	264	0.74	3726	1.77	16
HF-4	792	215	0.61	3905	1.72	23
HF-10	1021	247	0.76	3636	1.75	19
HF-3	890	239	0.68	3843	1.75	27
HF-2	763	199	0.58	3993	1.64	34
HF-19	970	-	0.82	3555	2.12	6
HF-17	1237	-	1.04	3282	2.22	15
HF-18	1785	-	1.51	2725	2.44	9
HF-15	1969	-	1.65	2572	2.37	19
HF-28	1523	371	1.37	3396	2.00	17
HF-24	977	280	0.94	3971	1.85	32
HF-27	1704	276	1.47	3143	1.98	28
HF-29	2399	439	2.11	2537	2.19	18
HF-22	2163	291	1.84	2584	2.11	23
HF-21	2009	336	1.73	2853	2.00	23
HF-20	2151	238	1.76	2925	2.15	23

Table 10
Oxygen mass transfer coefficient and oxygen terminal solubility in the molten zirconium obtained by fitting of the experimental data [1] and calculated values

T,°C	k_O, cm/s	$C_O(l)$, at.(wt.)% calculated	$C_O(l)$, at.(wt.)% after [7]
2000	$3 \cdot 10^{-4}$	40 (10.5)	42 (11.3)
2100	$1.1 \cdot 10^{-3}$	49 (14.5)	45 (12.7)
2200	$2 \cdot 10^{-3}$	50 (15)	47 (13.5)
2300	$6 \cdot 10^{-3}$	56.5 (17.6)	49.5 (14.7)
2400	$1.3 \cdot 10^{-2}$	57.4 (19.2)	53 (16.5)

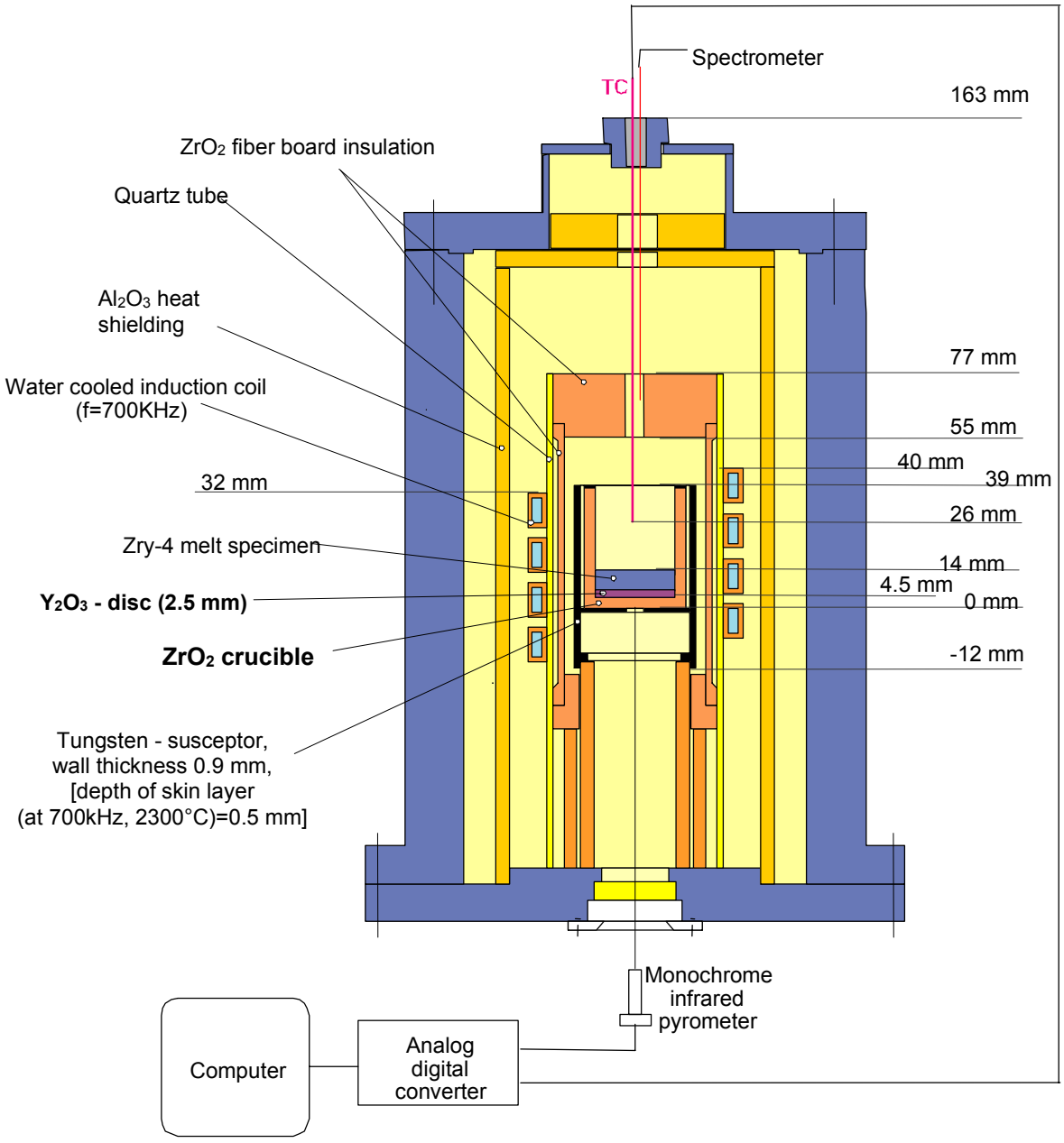

T_{max} = 2400 °C; p_{max}=3 bar

Fig. 1: LAVA Test Apparatus

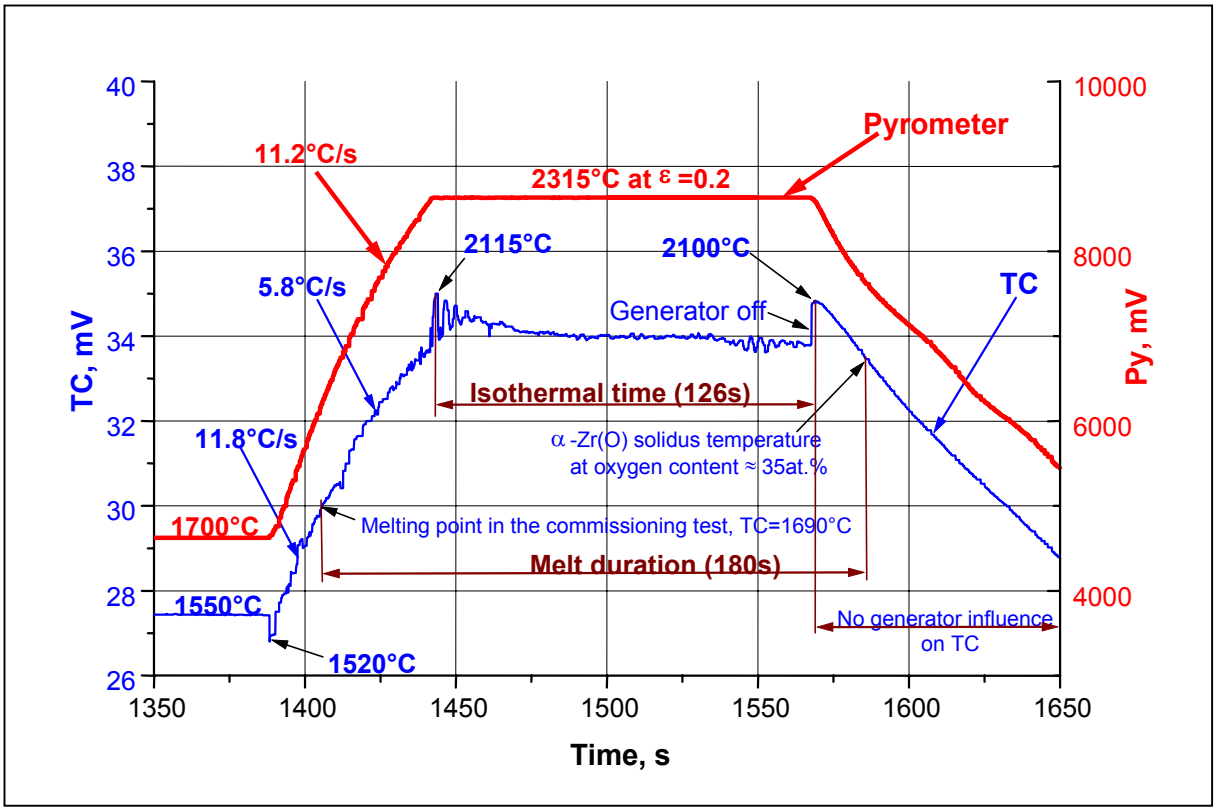

Fig. 2: Thermocouple and pyrometer signals
for test #26 (2300°C, target time ~3 min.)

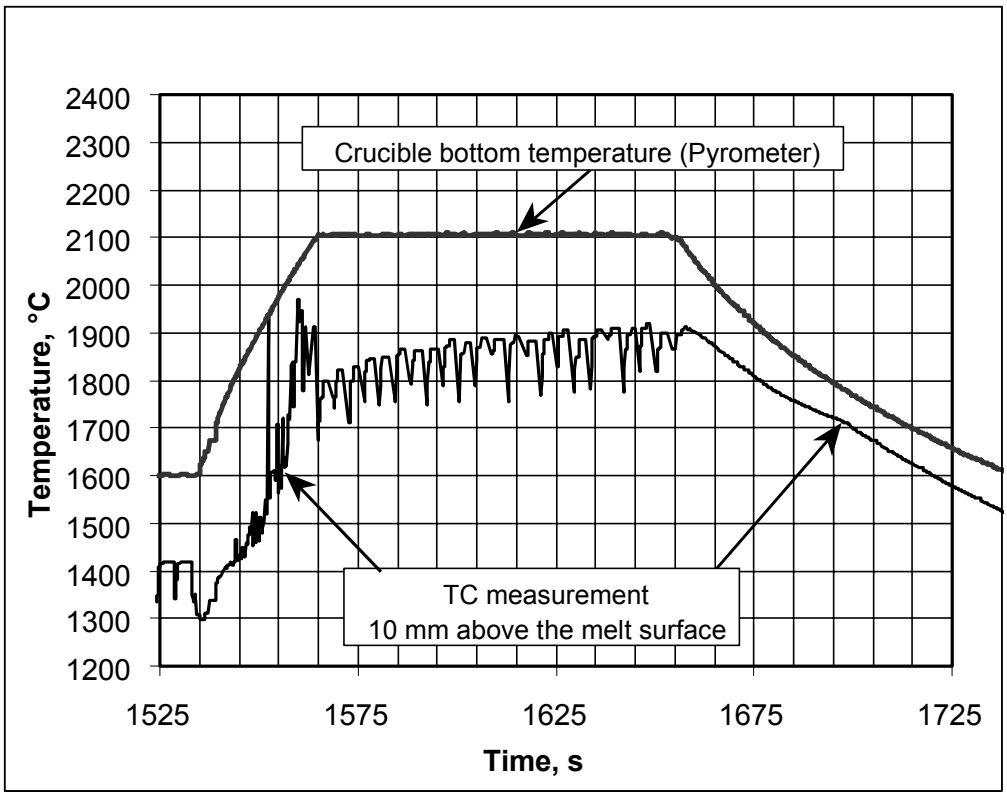

Fig. 3: Thermocouple and pyrometer temperature-time traces of test #5; 2100°C, 101s

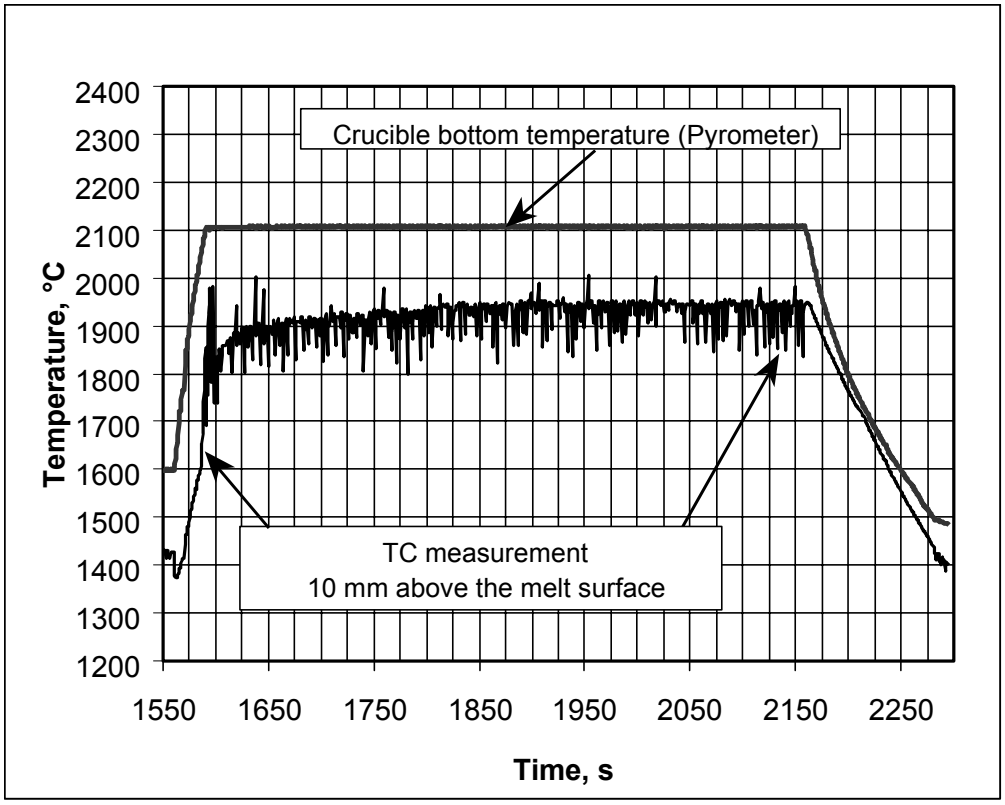

Fig. 4: Thermocouple and pyrometer temperature-time traces of test #4; 2100°C, 574s

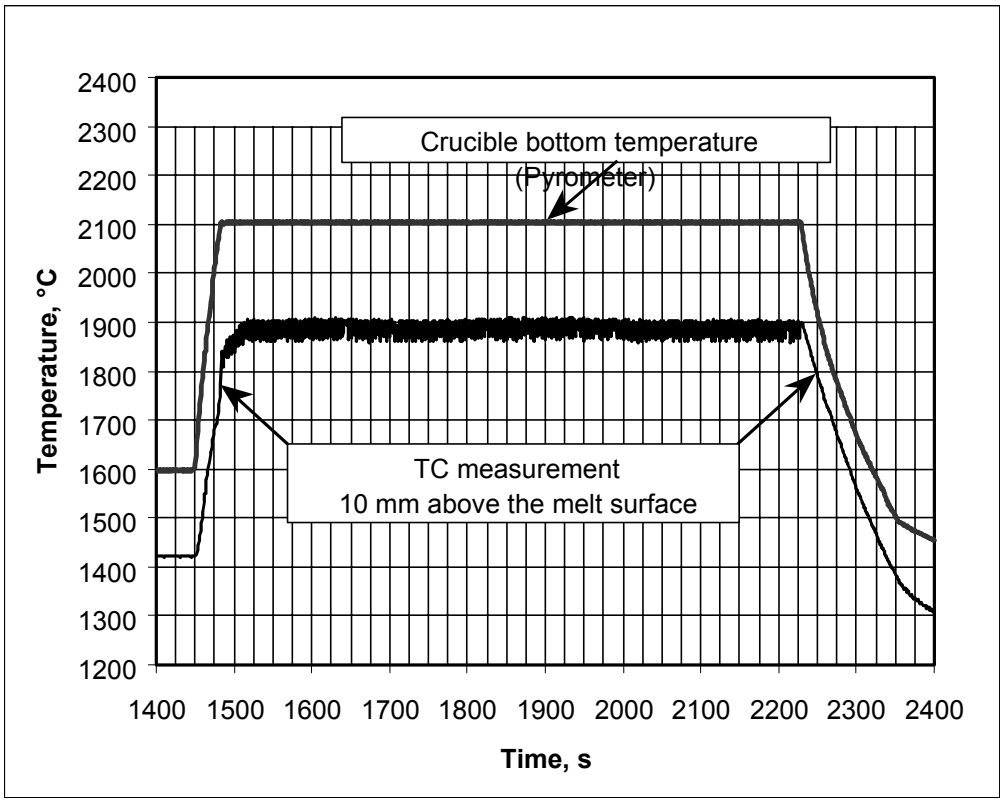

Fig. 5: Thermocouple and pyrometer temperature-time traces of test #7; 2100°C, 750s

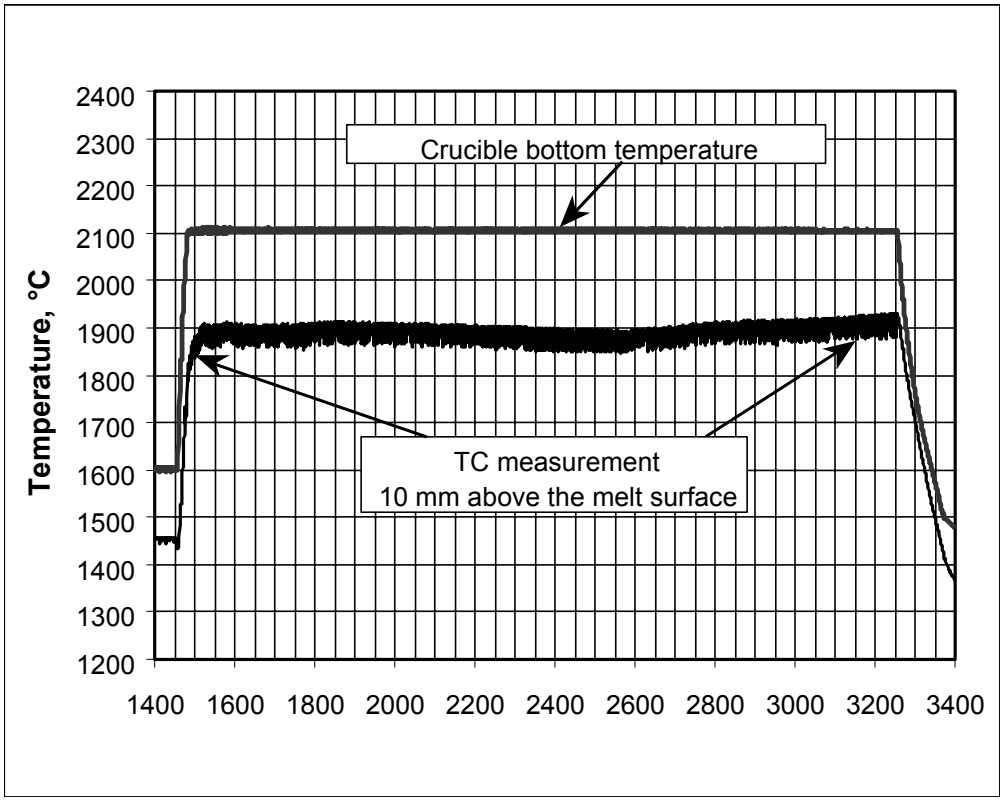

Fig. 6: Thermocouple and pyrometer temperature-time traces of test #8; 2100°C, 1778s

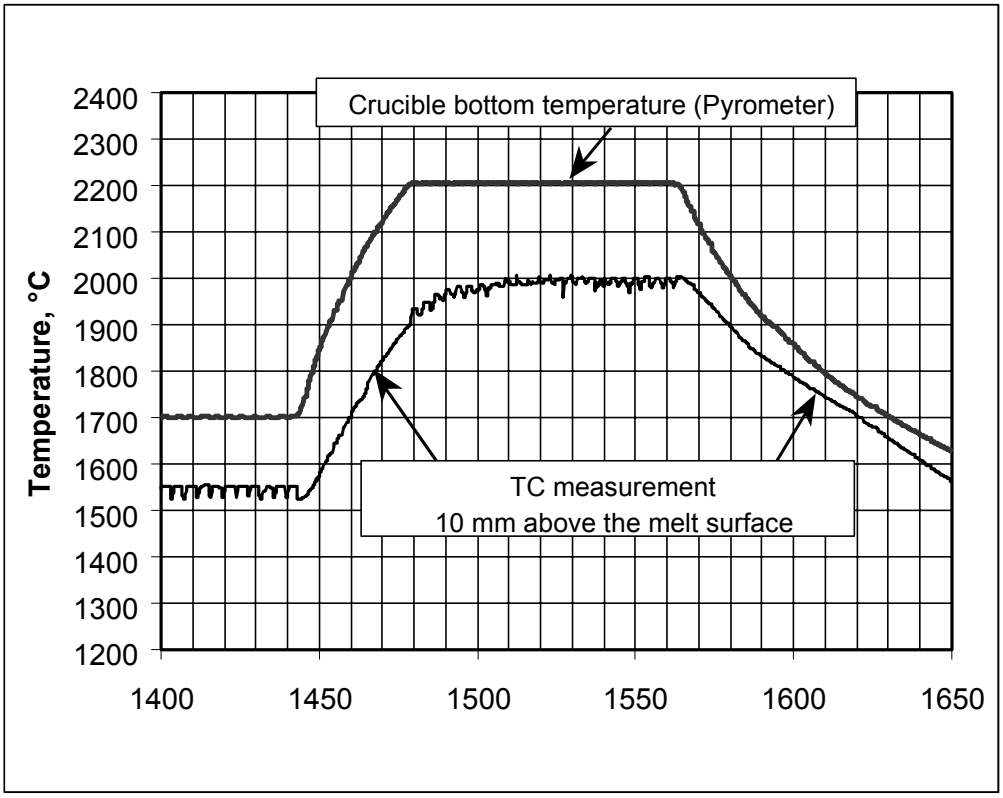

Fig. 7: Thermocouple and pyrometer temperature-time traces of test #13; 2200°C, 106s

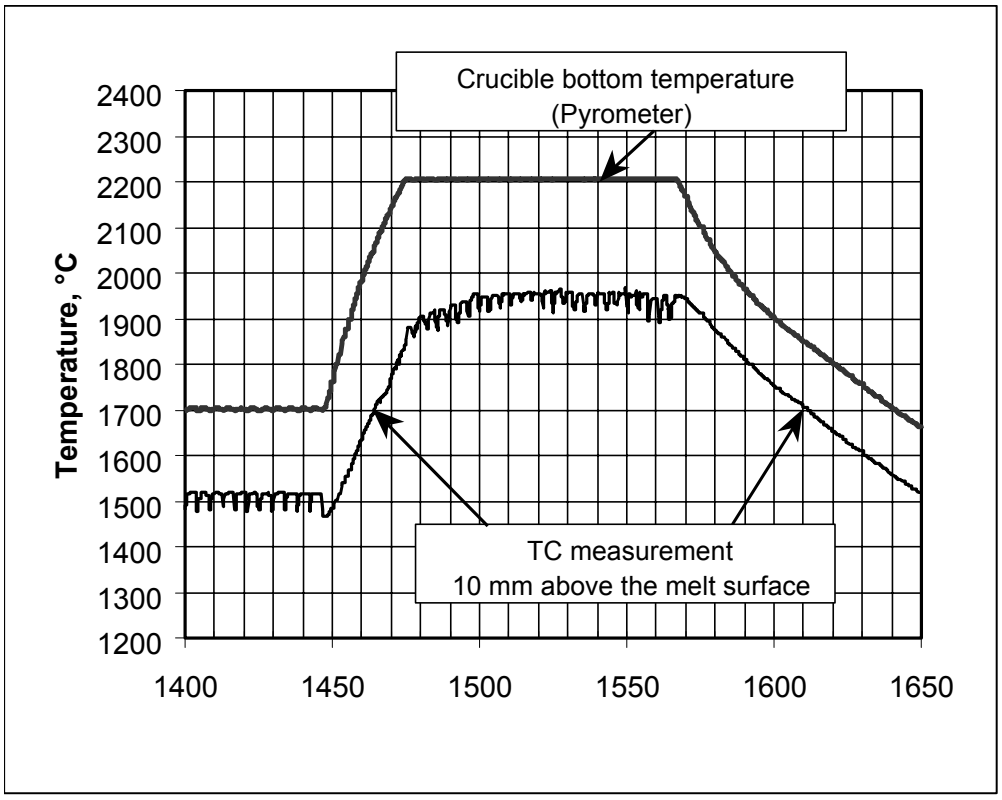

Fig. 8: Thermocouple and pyrometer temperature-time traces of test #14; 2200°C, 102s

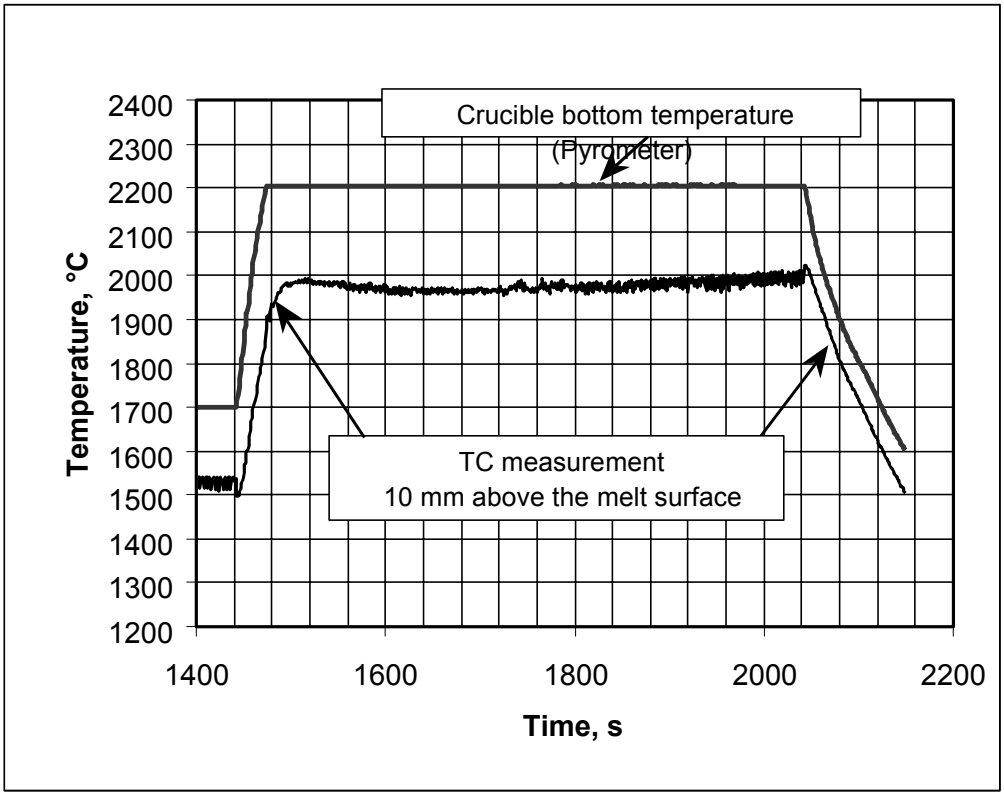

Fig. 9: Thermocouple and pyrometer temperature-time traces of test #12; 2200°C, 587s

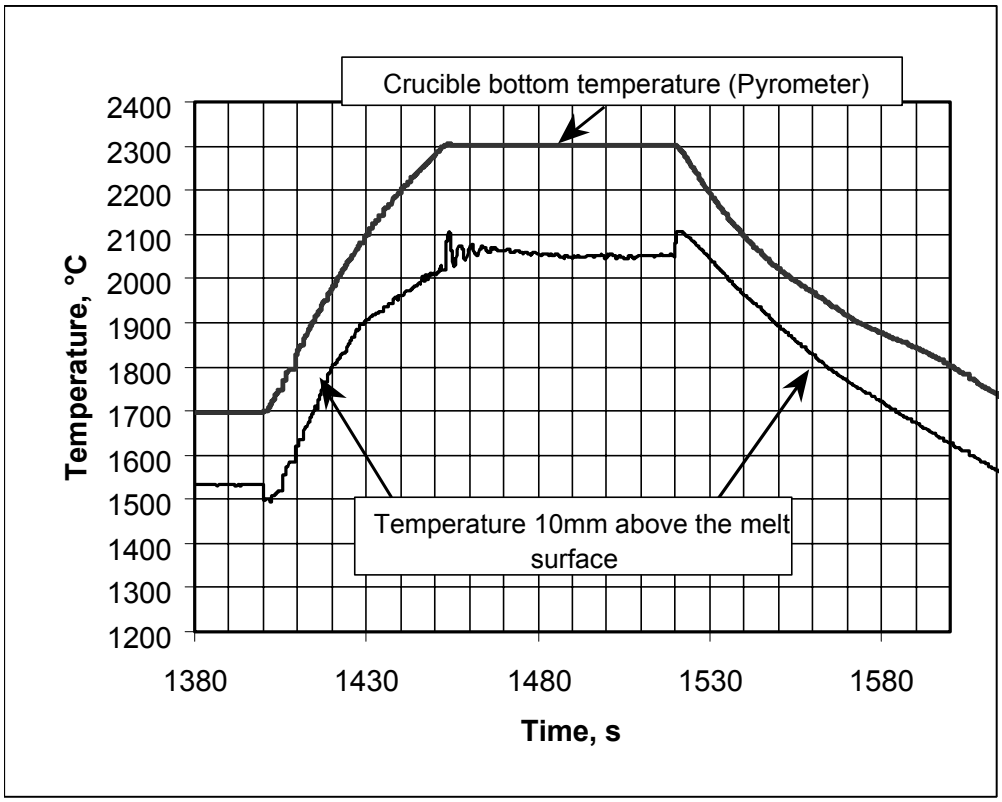

Fig. 10: Thermocouple and pyrometer temperature-time traces of test #24; 2300°C, 121s

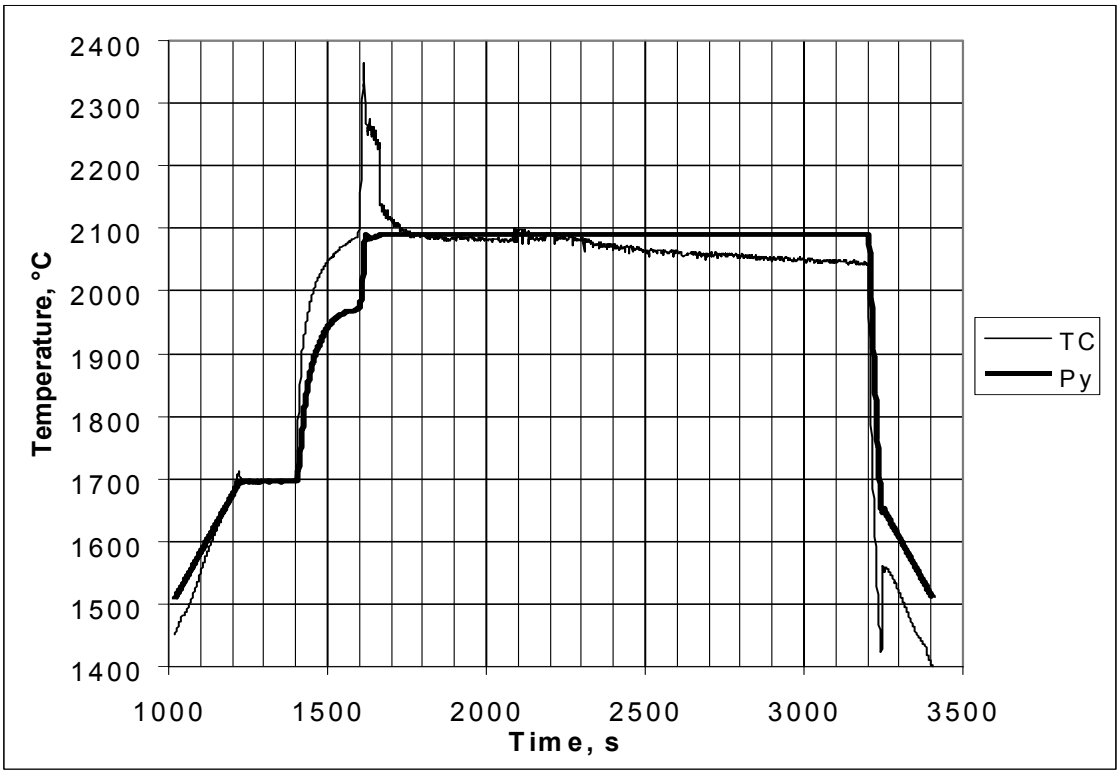

Fig. 11: Thermocouple and pyrometer temperature-time traces of test #FA1; 2100°C, 1820s

Fig. 12: Thermocouple and pyrometer temperature-time traces of test #FA2; 2100°C, 610s

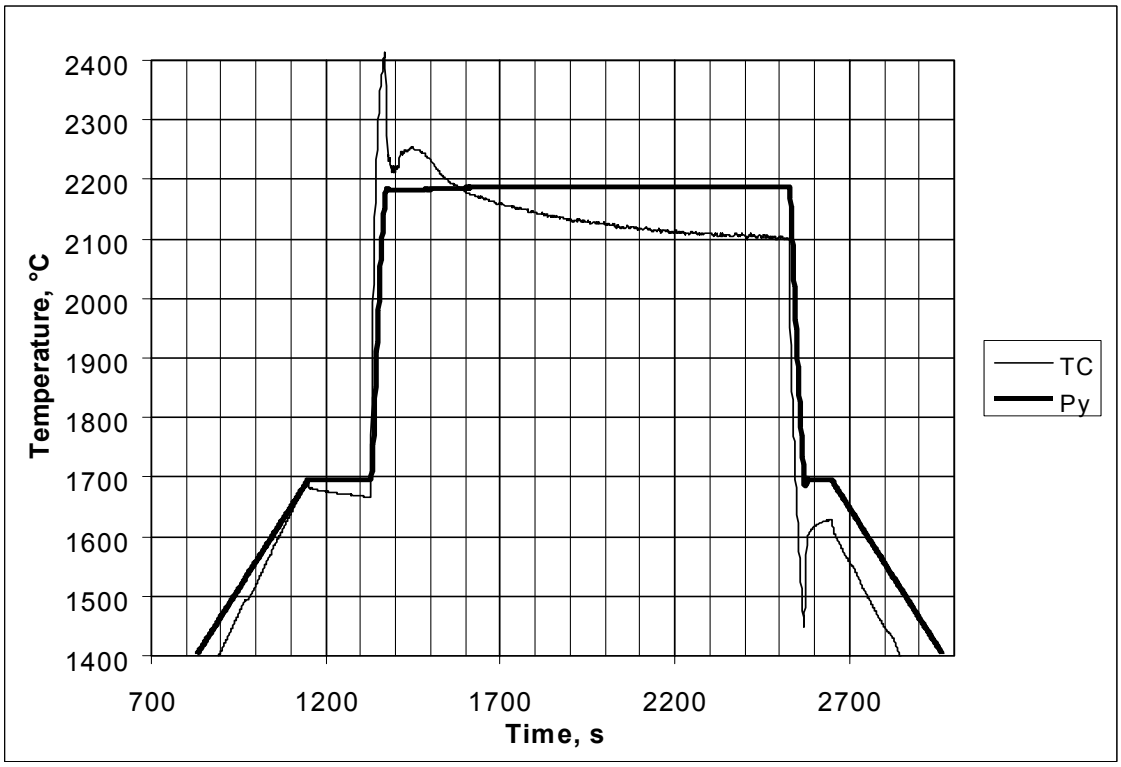

Fig. 13: Thermocouple and pyrometer temperature-time traces of test #FA3; 2200°C, 1220s

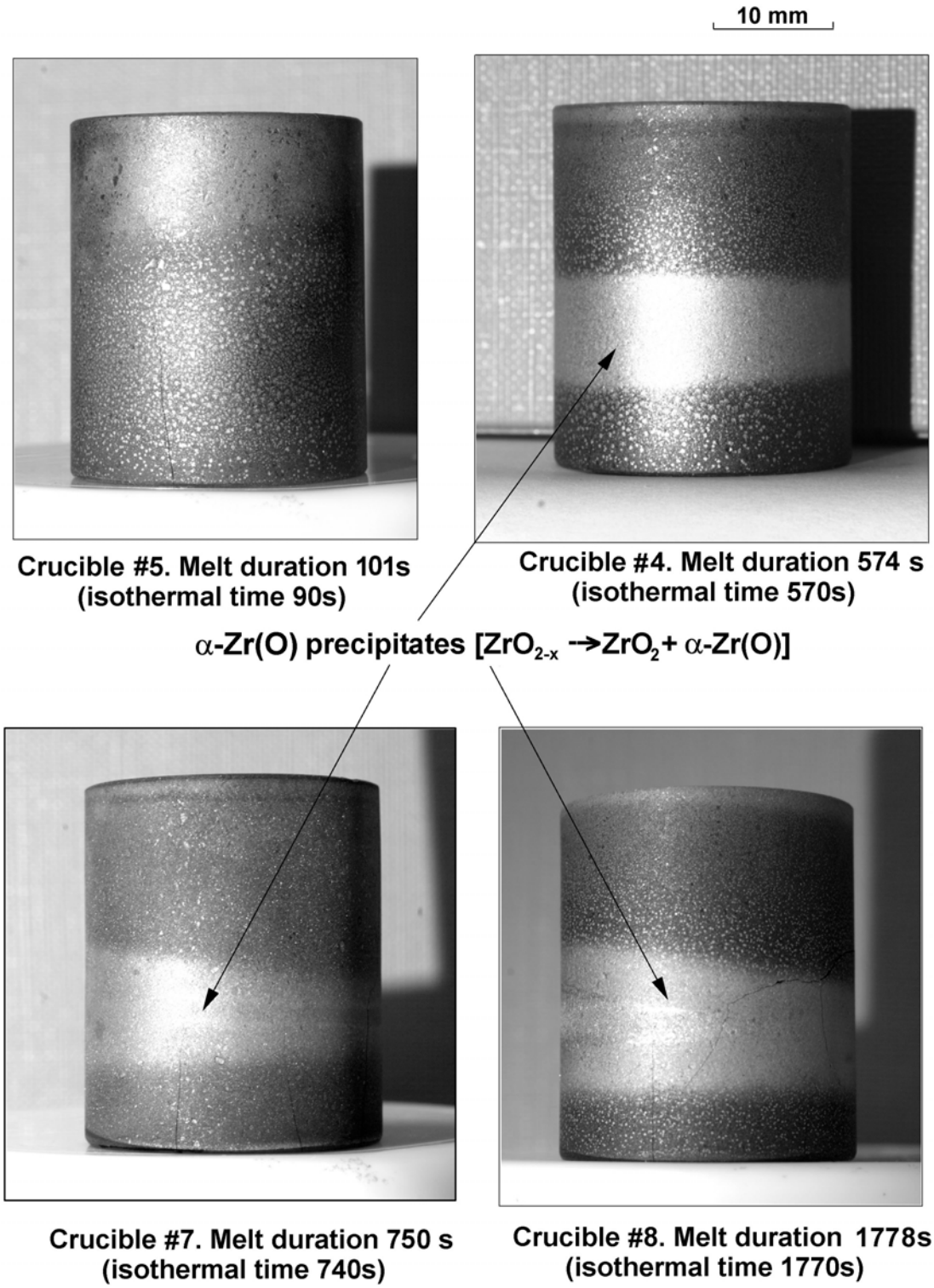

Fig. 14: Crucibles after dissolution tests at 2100°C

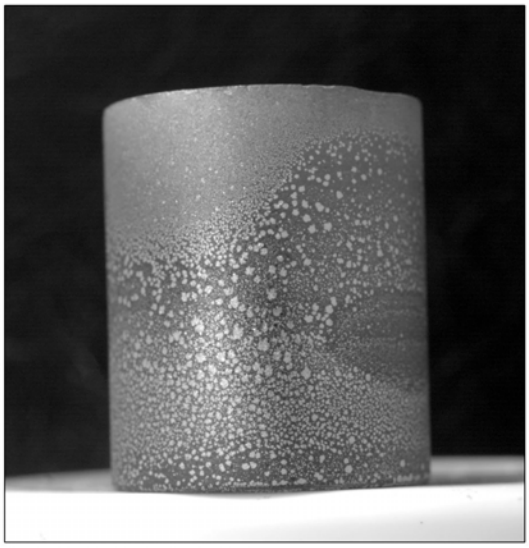

Crucible #14 without Y_2O_3 disc.
Melt duration 102s
(isothermal time 93s)

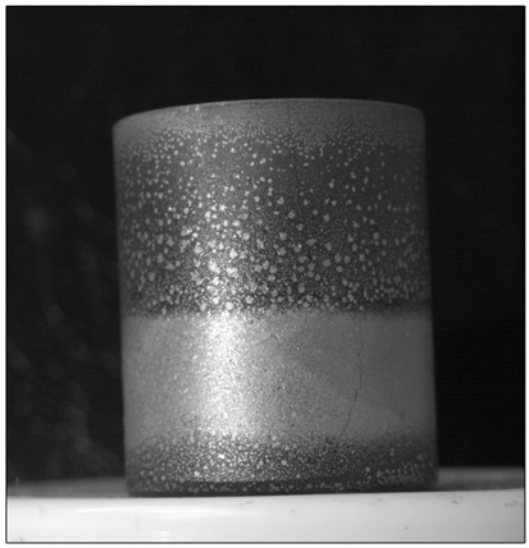

Crucible #12 without Y_2O_3 disc.
Melt duration 587s
(isothermal time 552s)

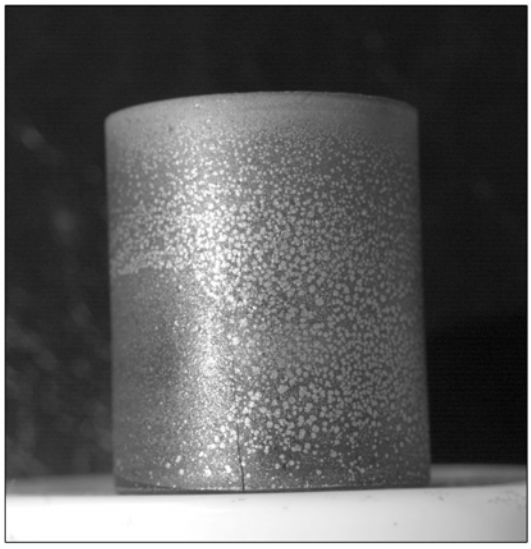

Crucible #13 with Y_2O_3 disc.
Melt duration 106s
(isothermal time 85s)

Fig. 15: Crucibles #12..#14 after dissolution tests at 2200°C

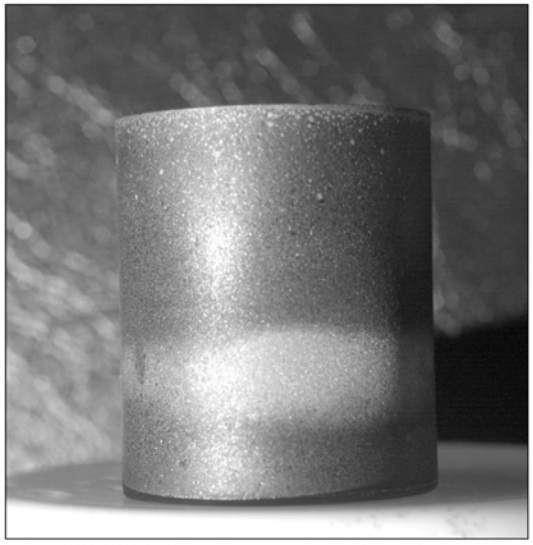

Crucible #24 without Y_2O_3 disc.
Melt duration 121s
(isothermal time 67s)

Fig. 16: Crucible after dissolution test at 2300°C

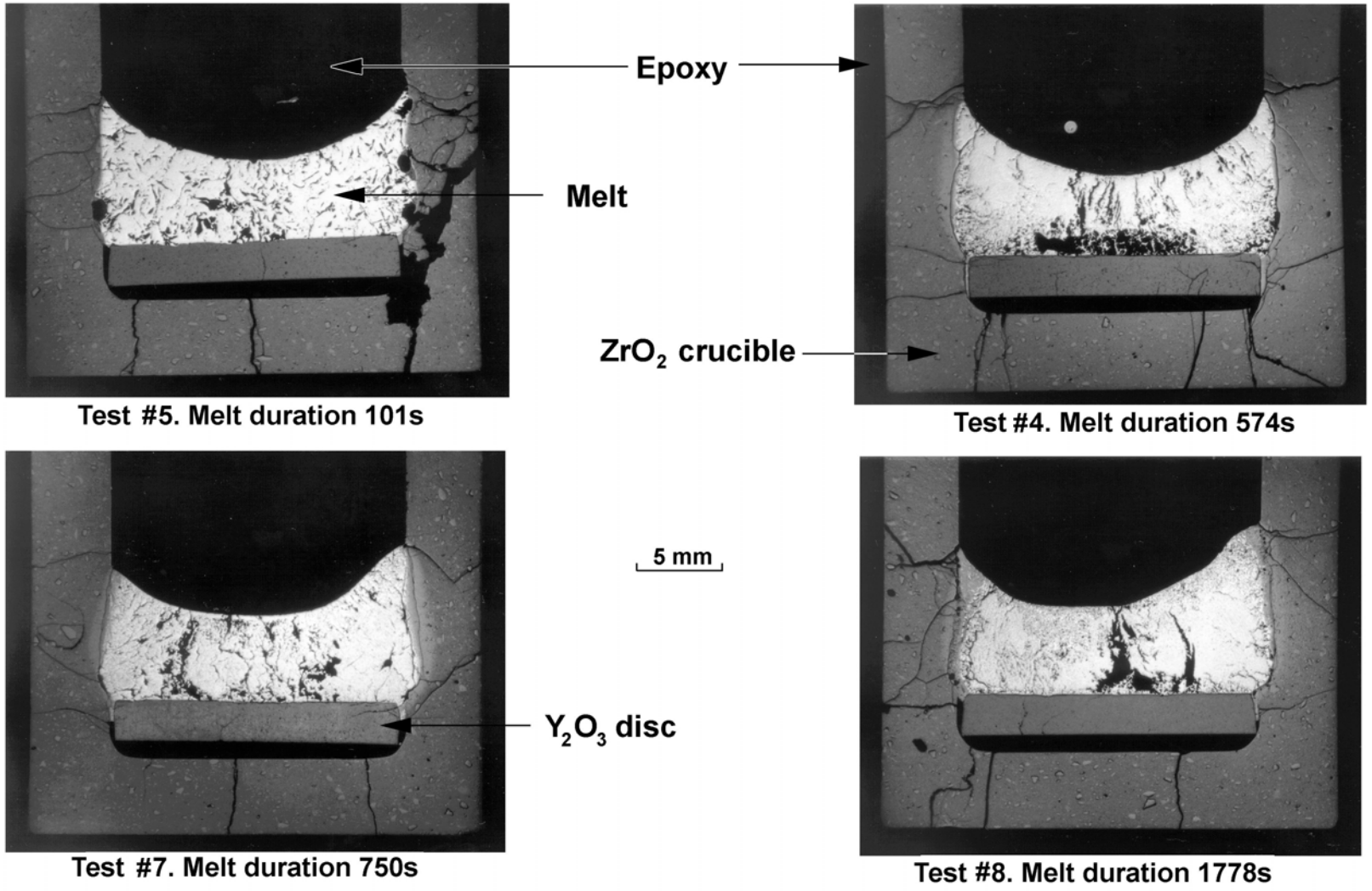

Fig. 17: Optical view (vertical illumination) of longitudinal crucible cross-sections after dissolution tests at 2100°C

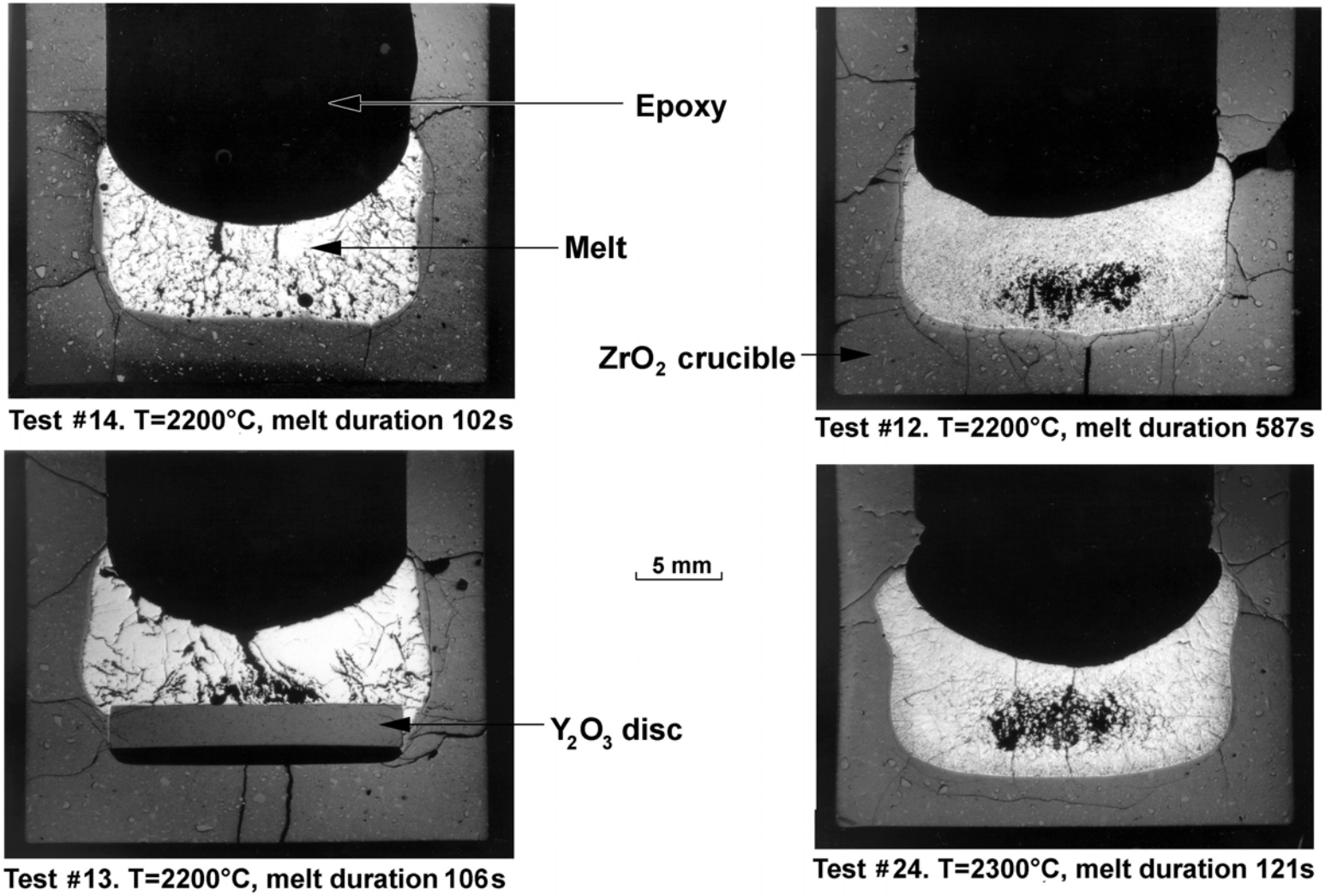

Fig. 18: Optical view (vertical illumination) of longitudinal crucible cross-sections after dissolution tests at 2200°C and 2300°C

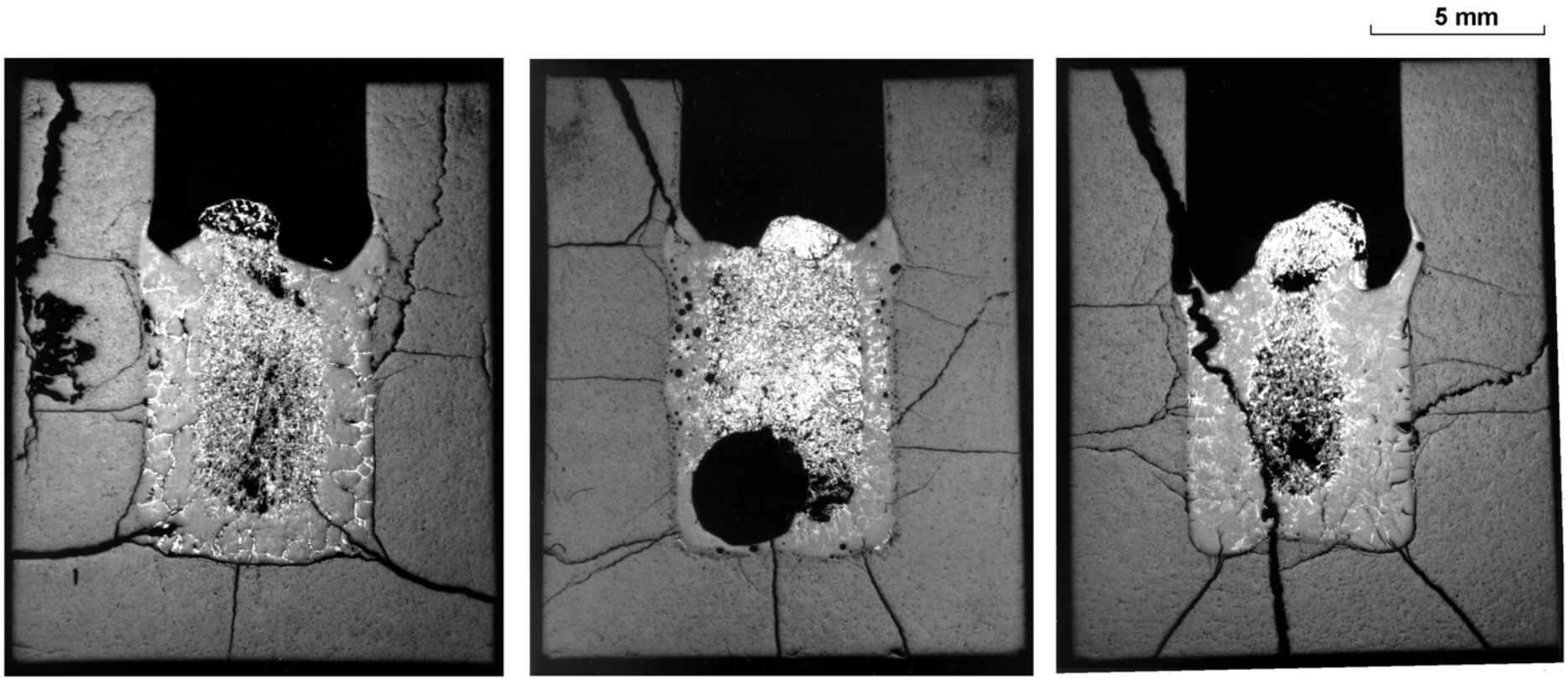

Test FA3. 2200°C, 20min.
Transition layer thickness 1.5 mm

Test FA2. 2100°C, 10min.
Transition layer thickness 1 mm

Test FA1. 2100°C, 33min.
Transition layer thickness 2.2 mm

Fig.19. FZK tests with AECL crucibles.
Interaction area to the liquid Zry volume ratio: S/V=765 m^{-1}

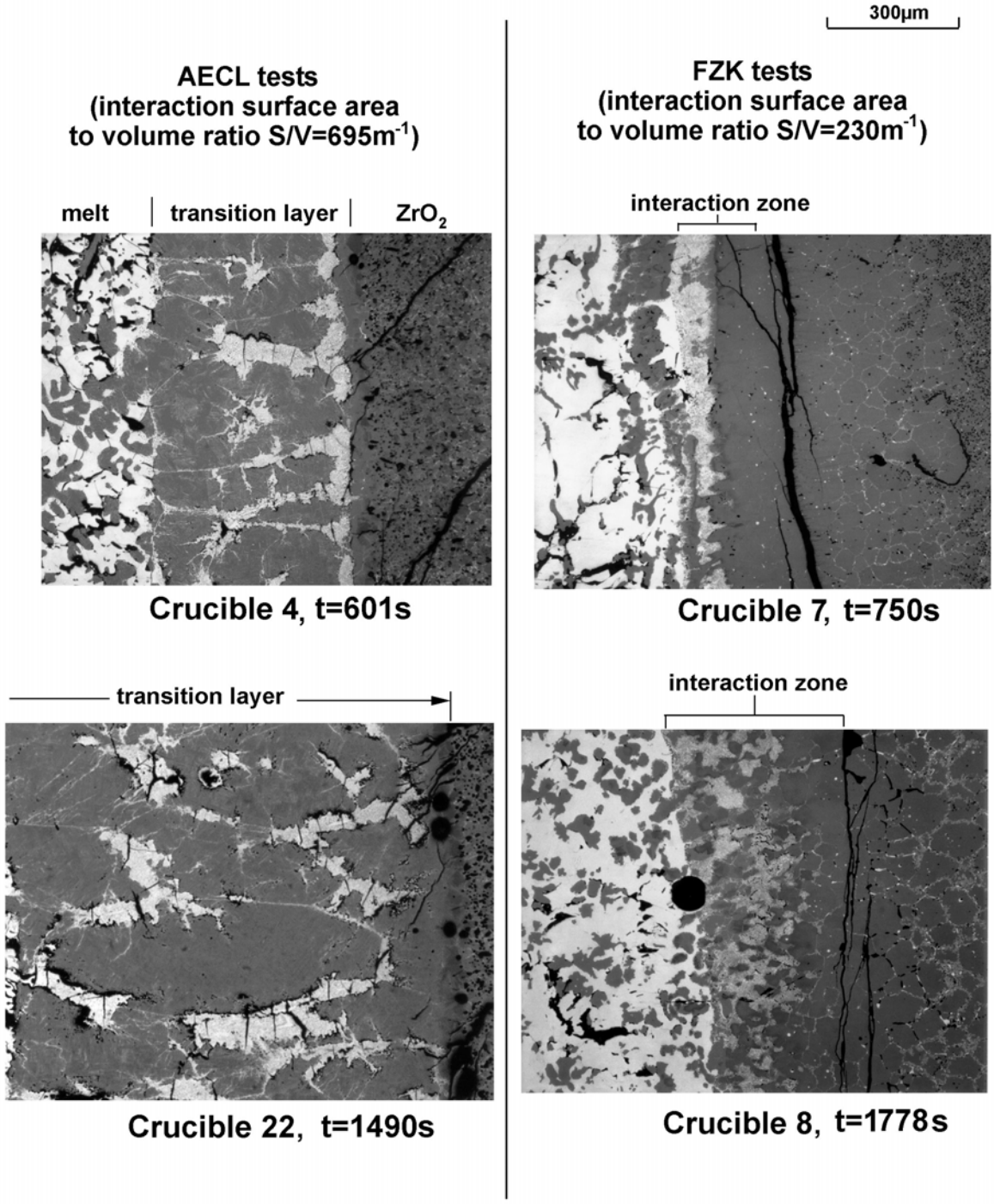

Fig. 20: Interface boundary between melt and crucible wall at 2100°C

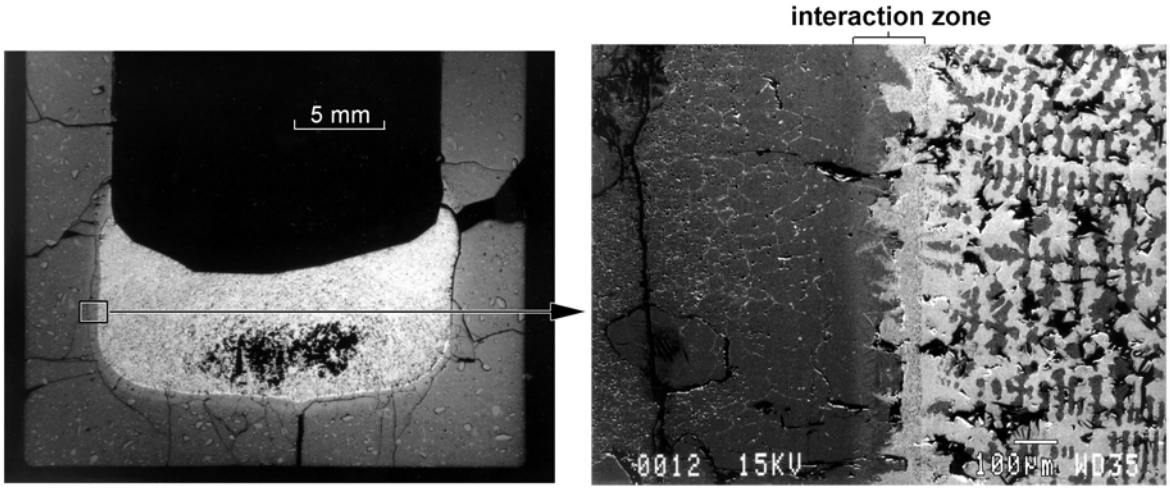

FZK test #12. Melt duration 587s

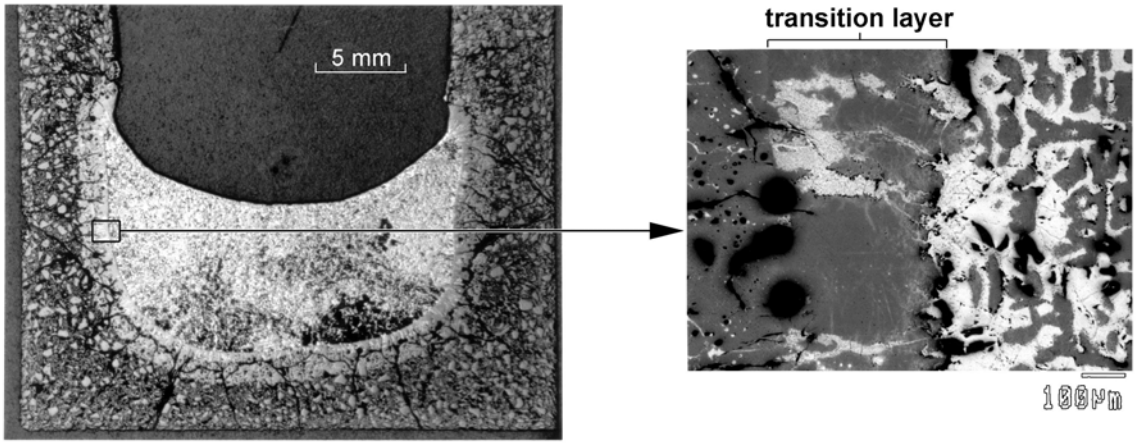

KfK test #LV122. Melt duration 600s

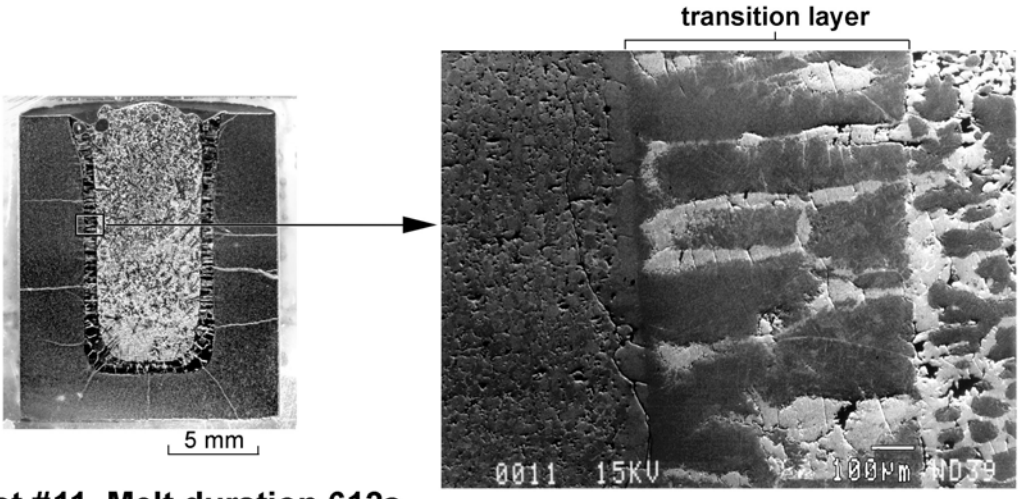

AECL test #11. Melt duration 612s

Fig. 21: Transition layer formation at 2200°C in different type of crucible tests (FZK, KfK, AECL)

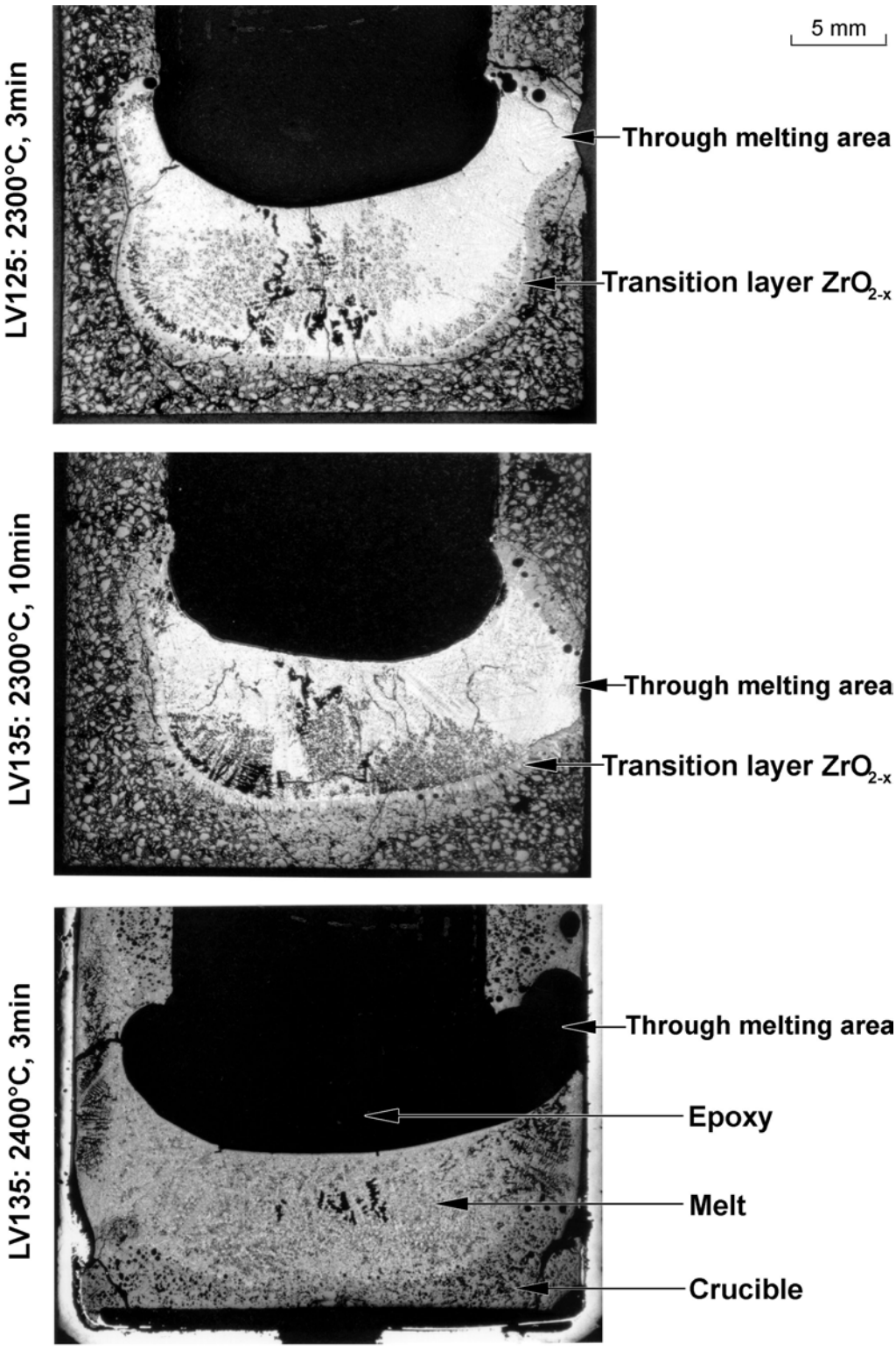

Fig. 22: Longitudinal cross-sections of failed crucibles in earlier KfK tests

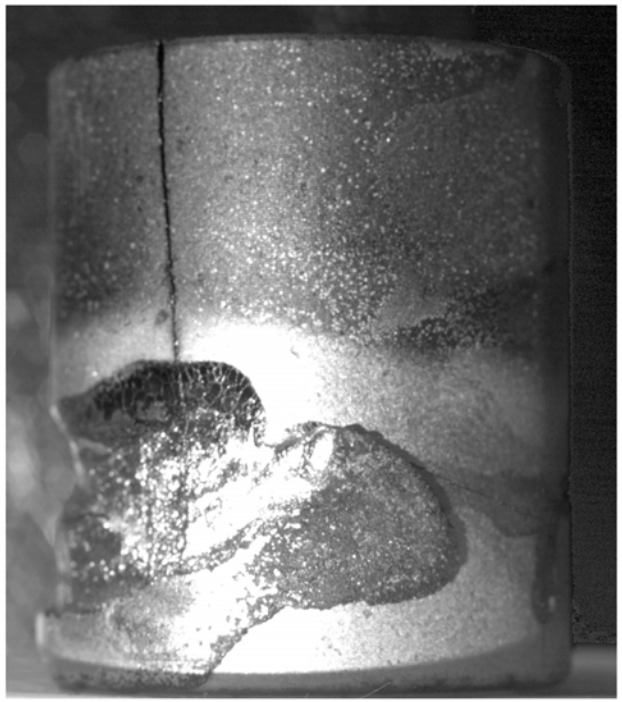

Crucible #19 without Y_2O_3 bottom isolation
after the dissolution test at 2200°C, 1830s
(outer appearance)

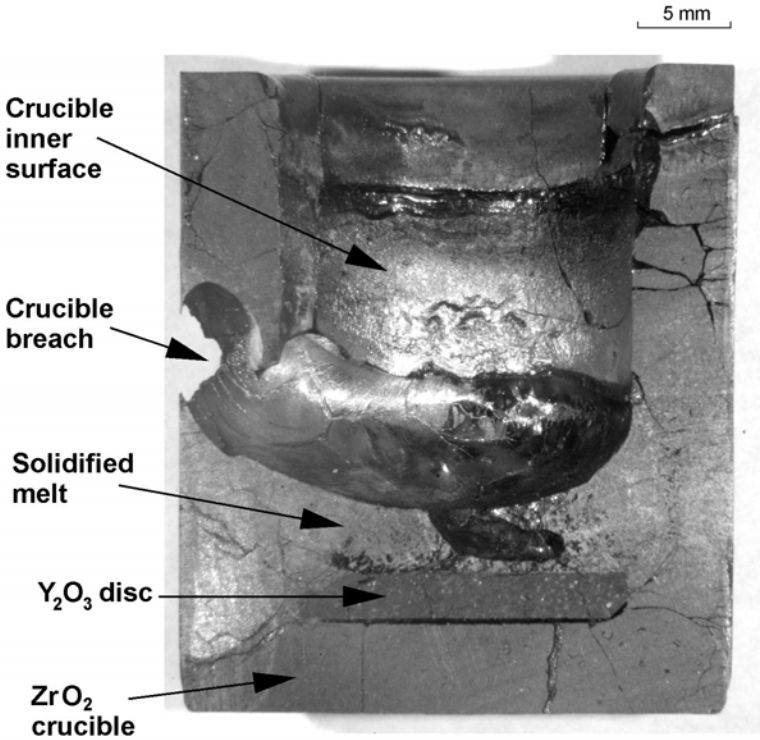

Longitudinal section
of a failed crucible 18 (2200°C, 610s)

Fig. 23: Examples of failed FZK crucibles

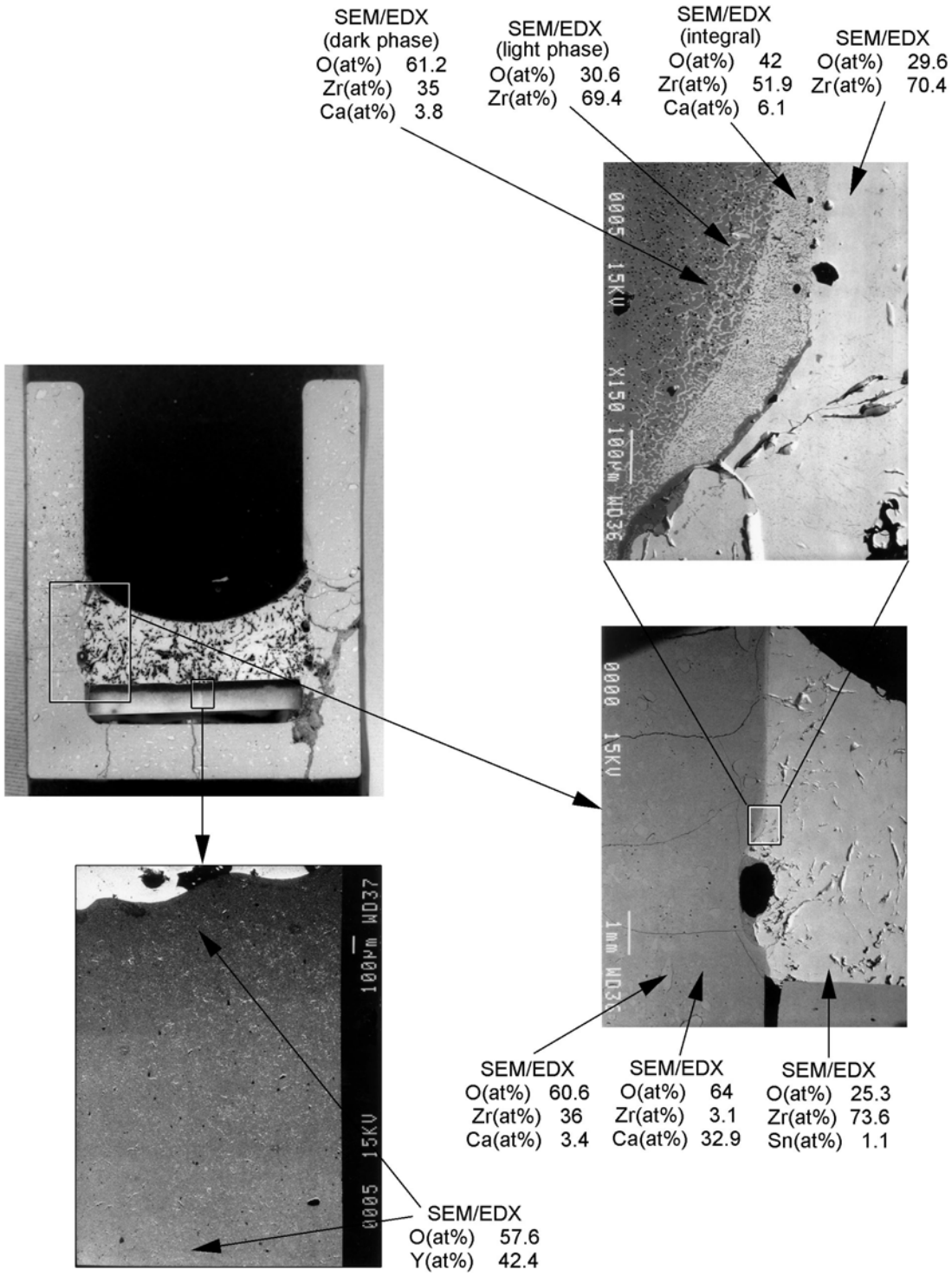

Fig. 24: Crucible #5 (2100°C, 101s)
SEM/EDX analysis of interaction areas melt-zirconia wall and melt-yttria bottom

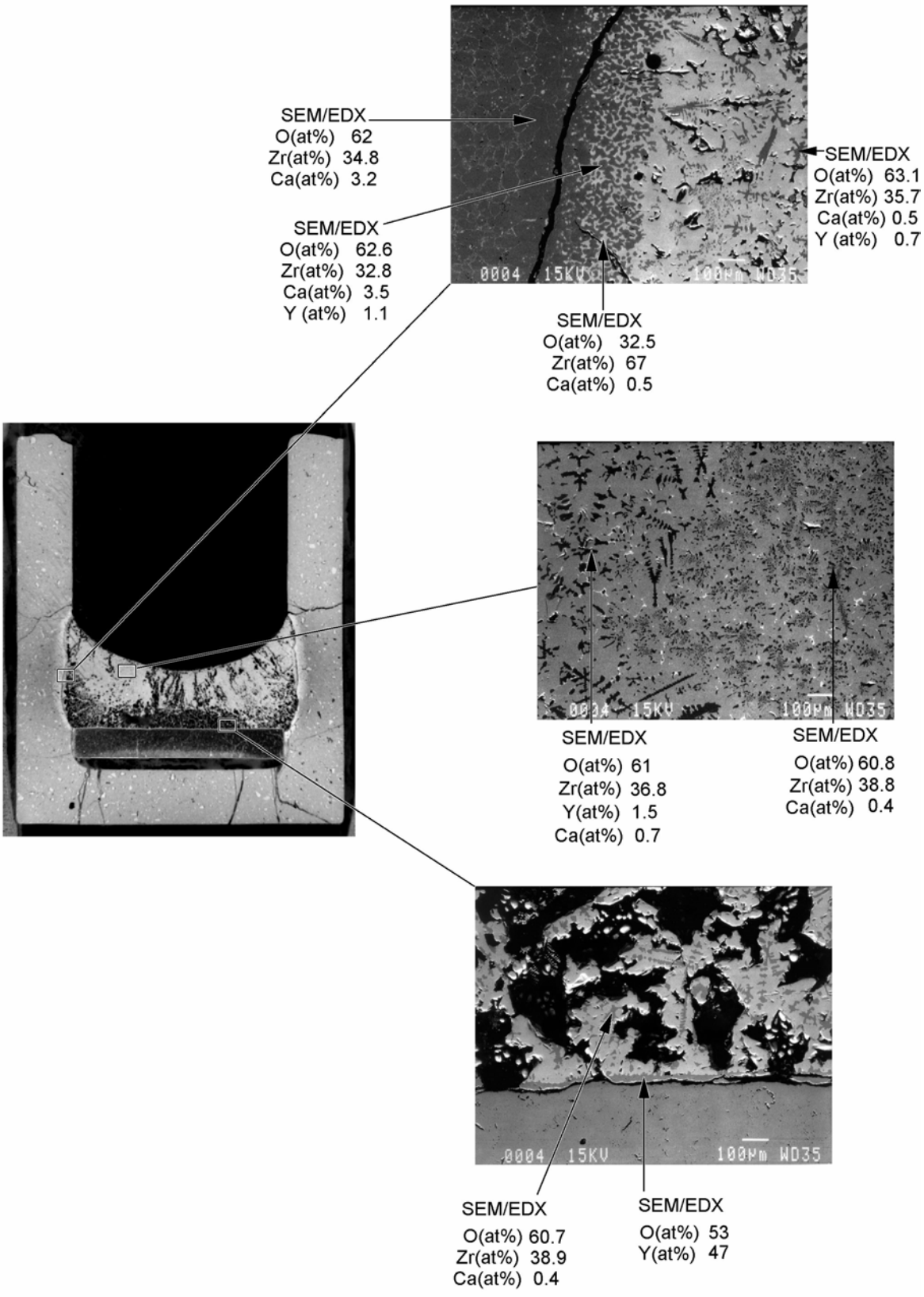

Fig. 25: Crucible 4 (2100°C, 574s)
SEM/EDX analysis

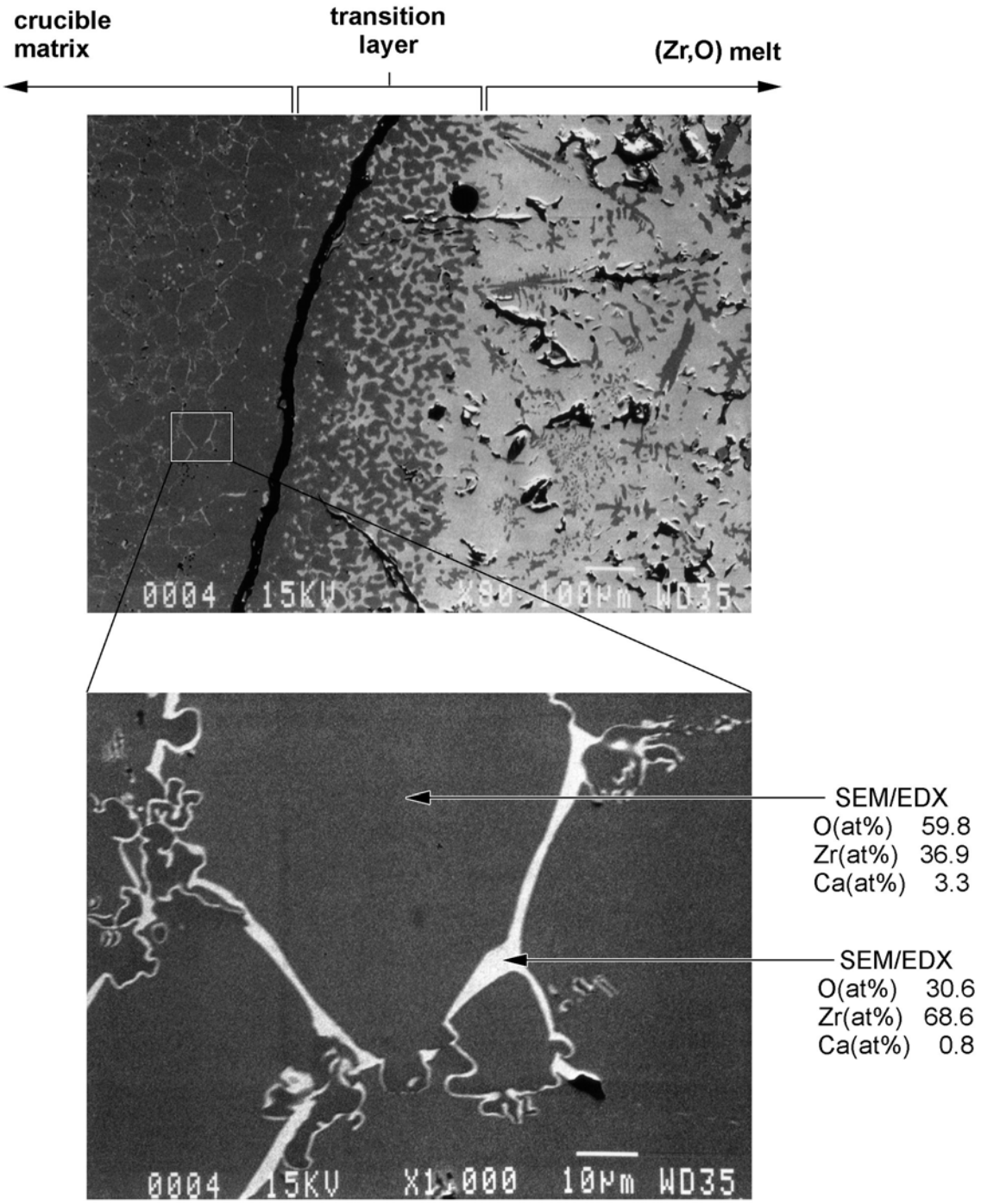

formation of α-Zr(O) along a grain boundary

Fig. 26: Crucible #4 (2100°C, 574s)
Formation of once molten "α-Zr(O) channels"
along the ZrO_2 grain boundaries

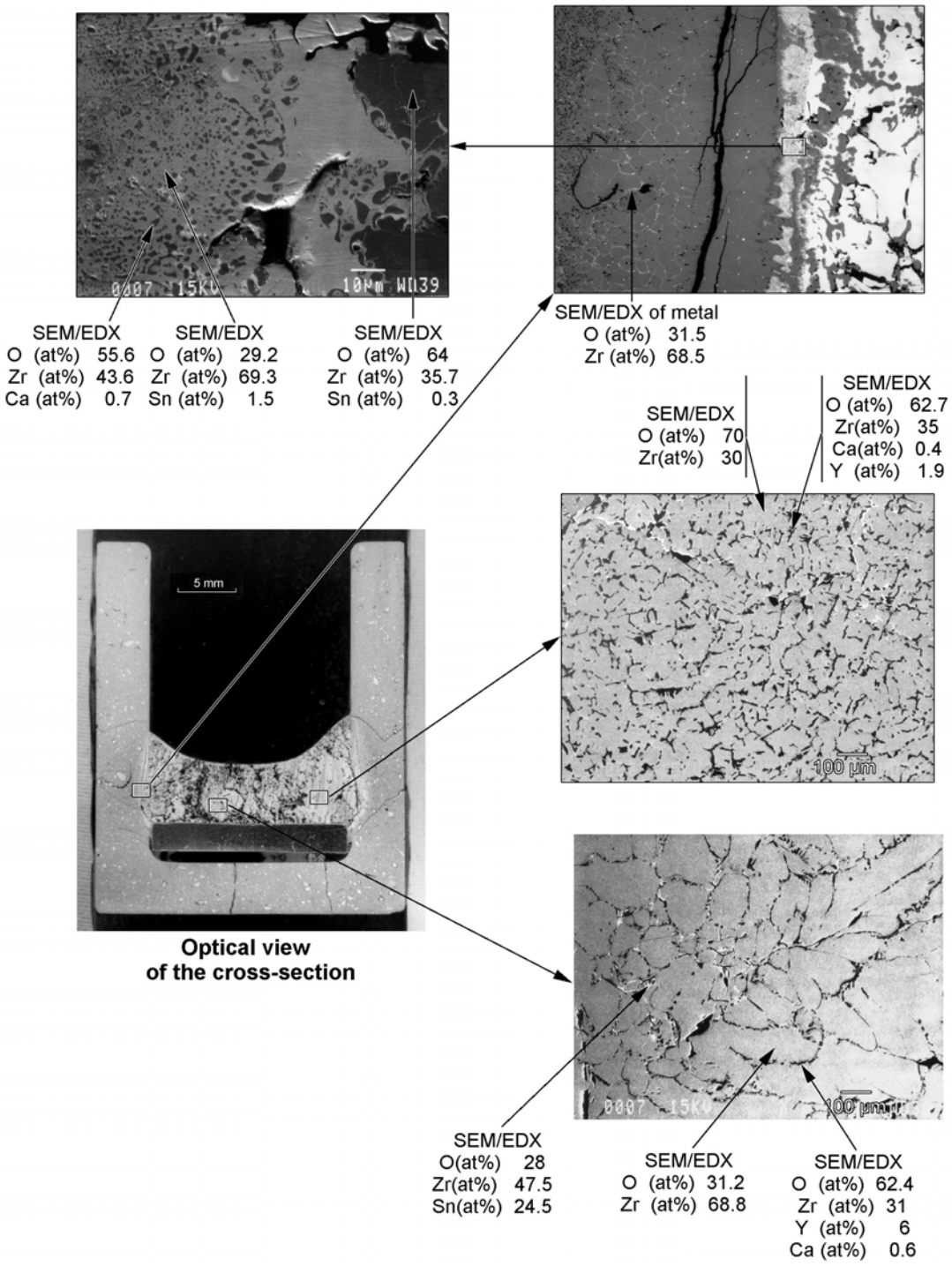

Fig. 27: Crucible #7 (2100°C, 750s)
SEM/EDX analysis

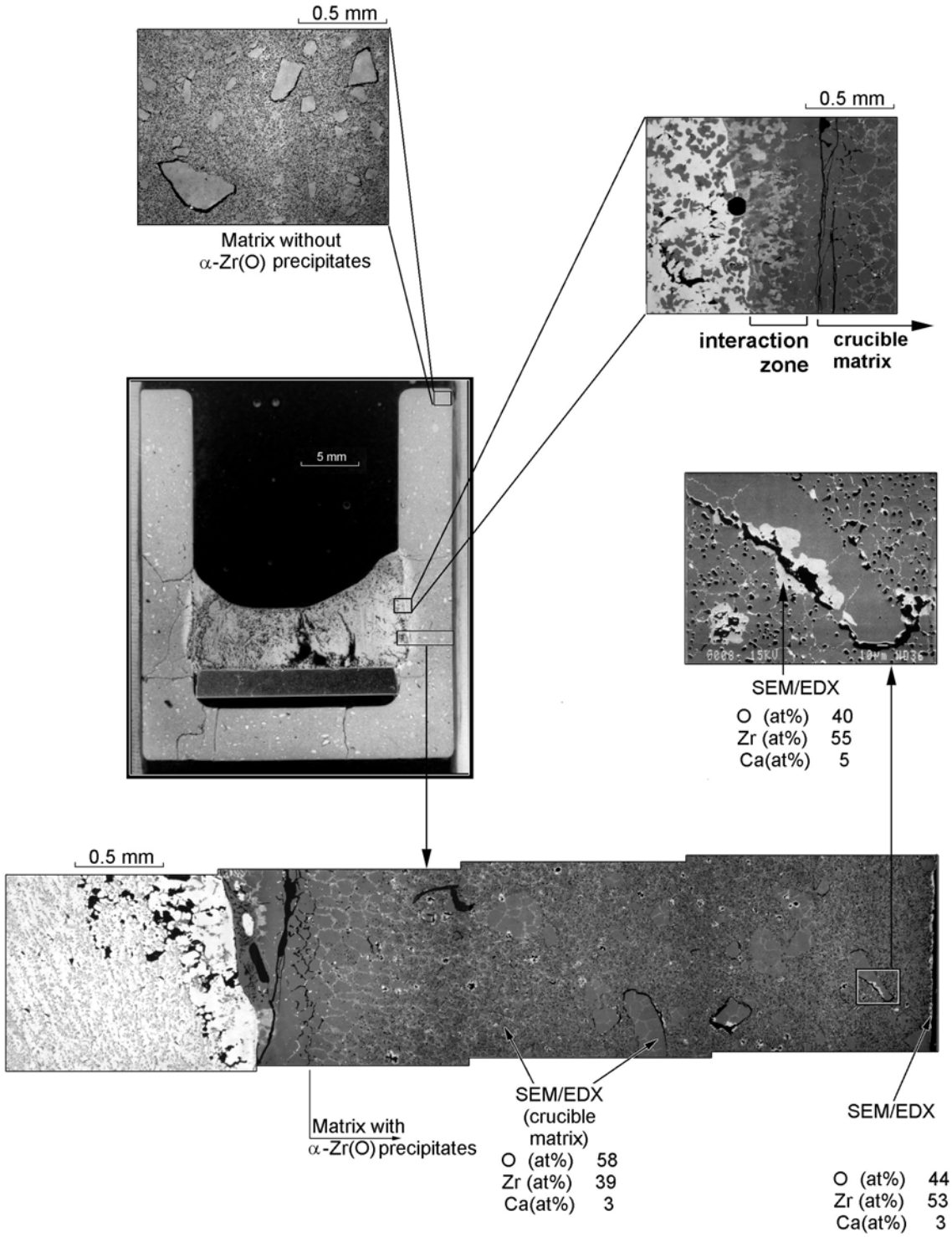

Fig. 28: Crucible #8 (2100°C, 1778s).
Formation of α-Zr(O) precipitates in the crucible wall matrix by O-diffusion along the grain boundaries to the melt

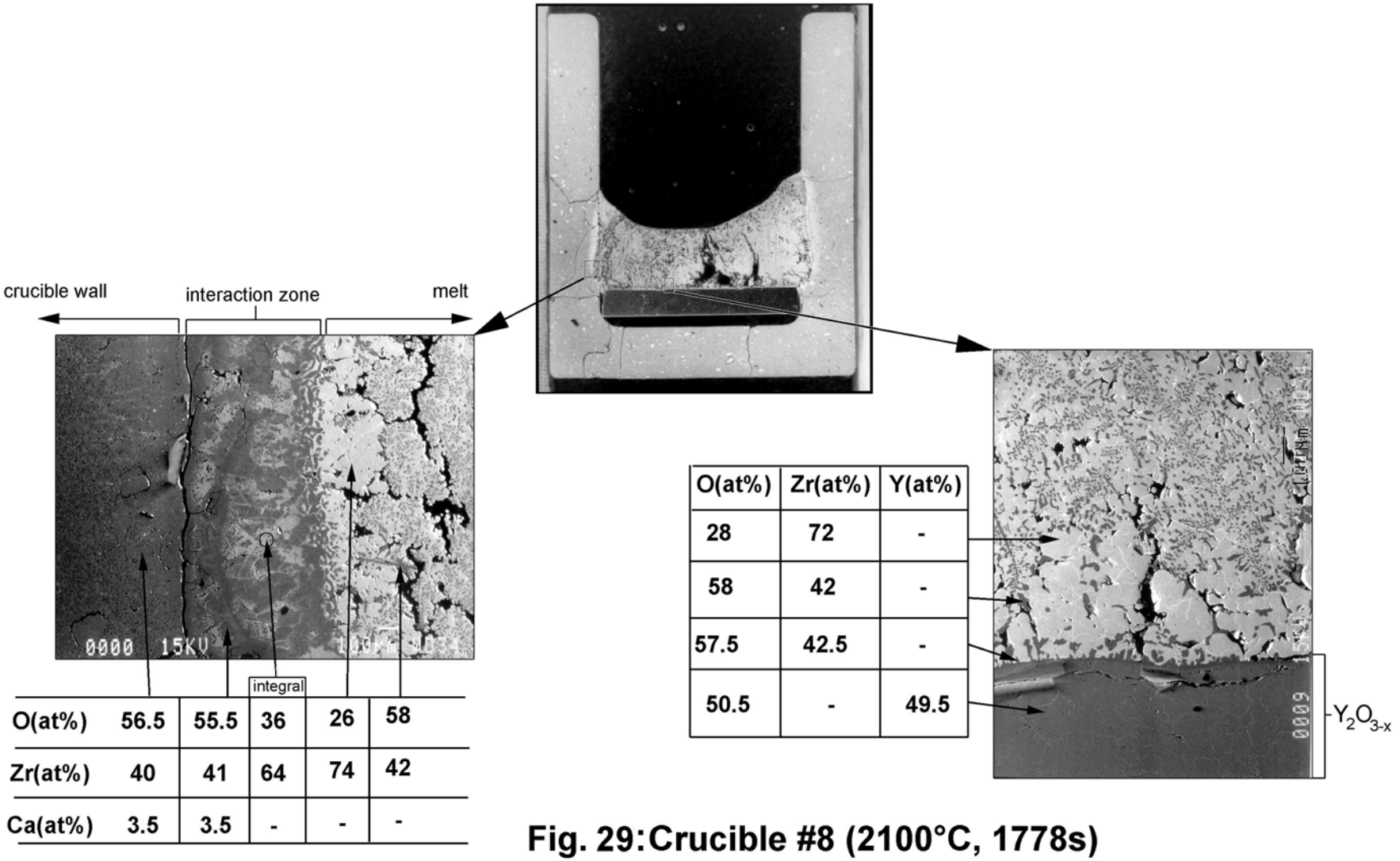

Fig. 29: Crucible #8 (2100°C, 1778s)

SEM/EDX analysis of the interaction areas melt - zirconia wall and melt - yttria bottom

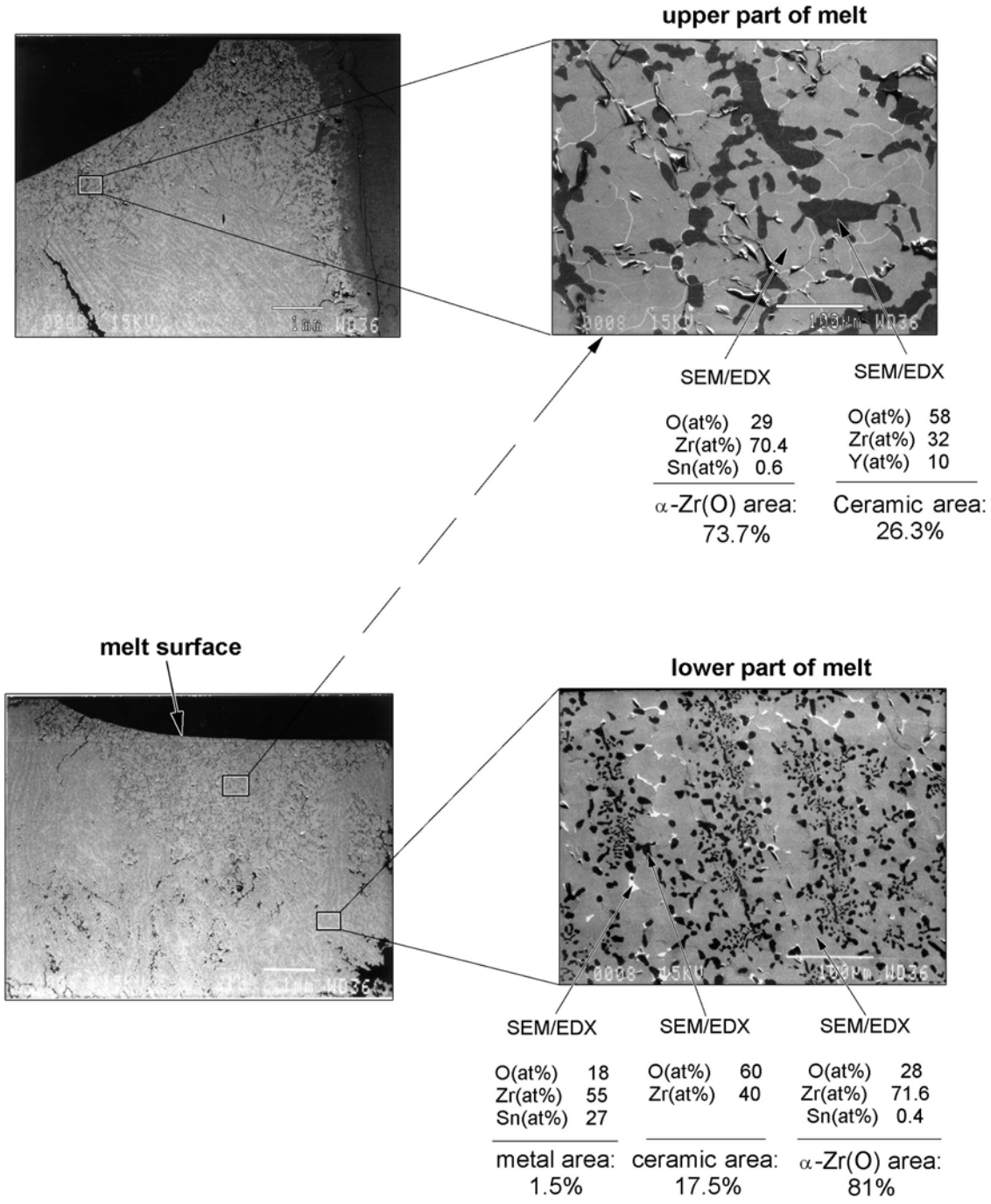

Fig. 30: Crucible #8 (2100°C, 1778s)
Element and phase area analysis of the melt

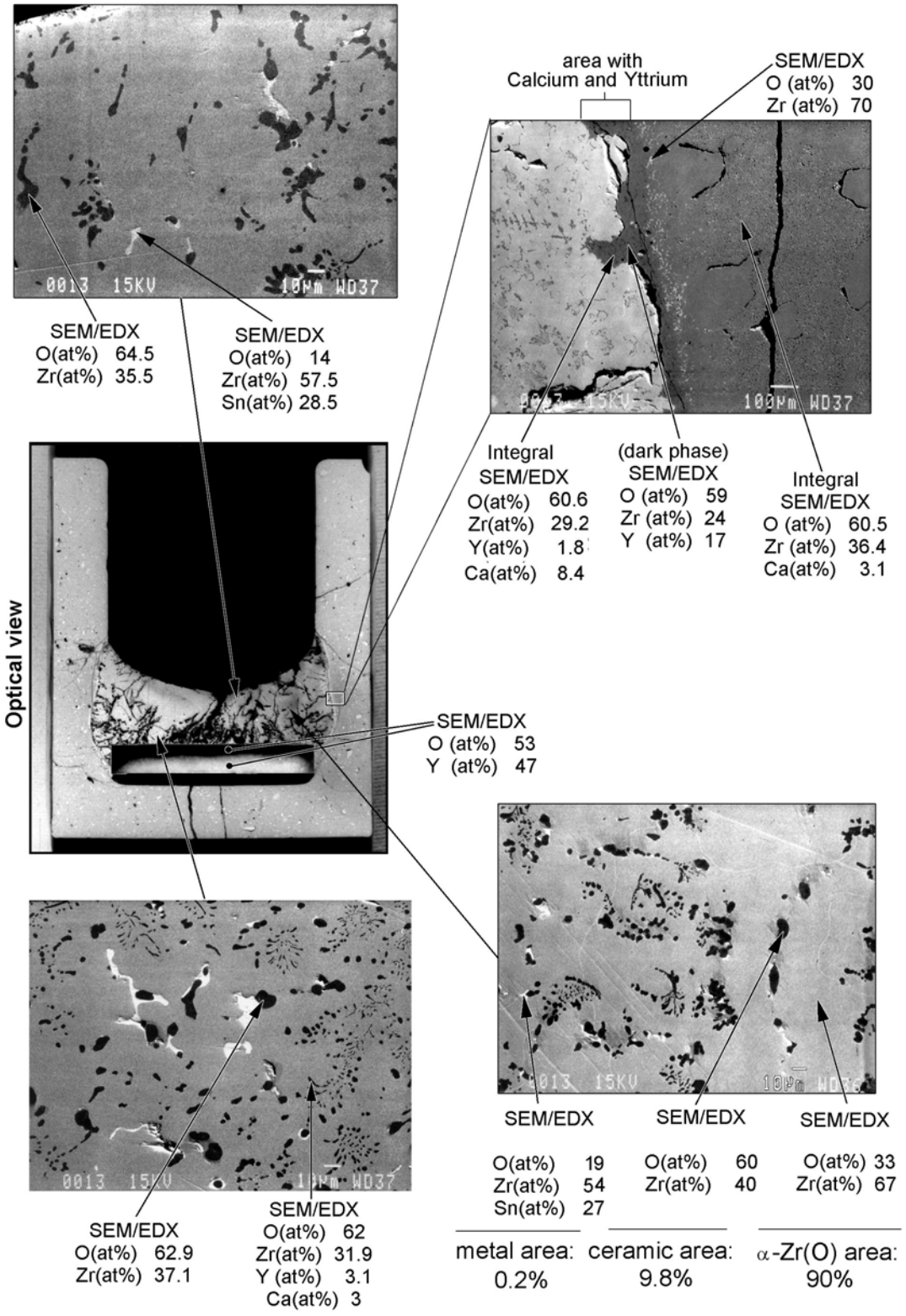

Fig. 31: Crucible #13 (2200°C, 106 s)
Element and phase area analysis of the melt
Yttrium traces in transition layer between melt and crucible wall

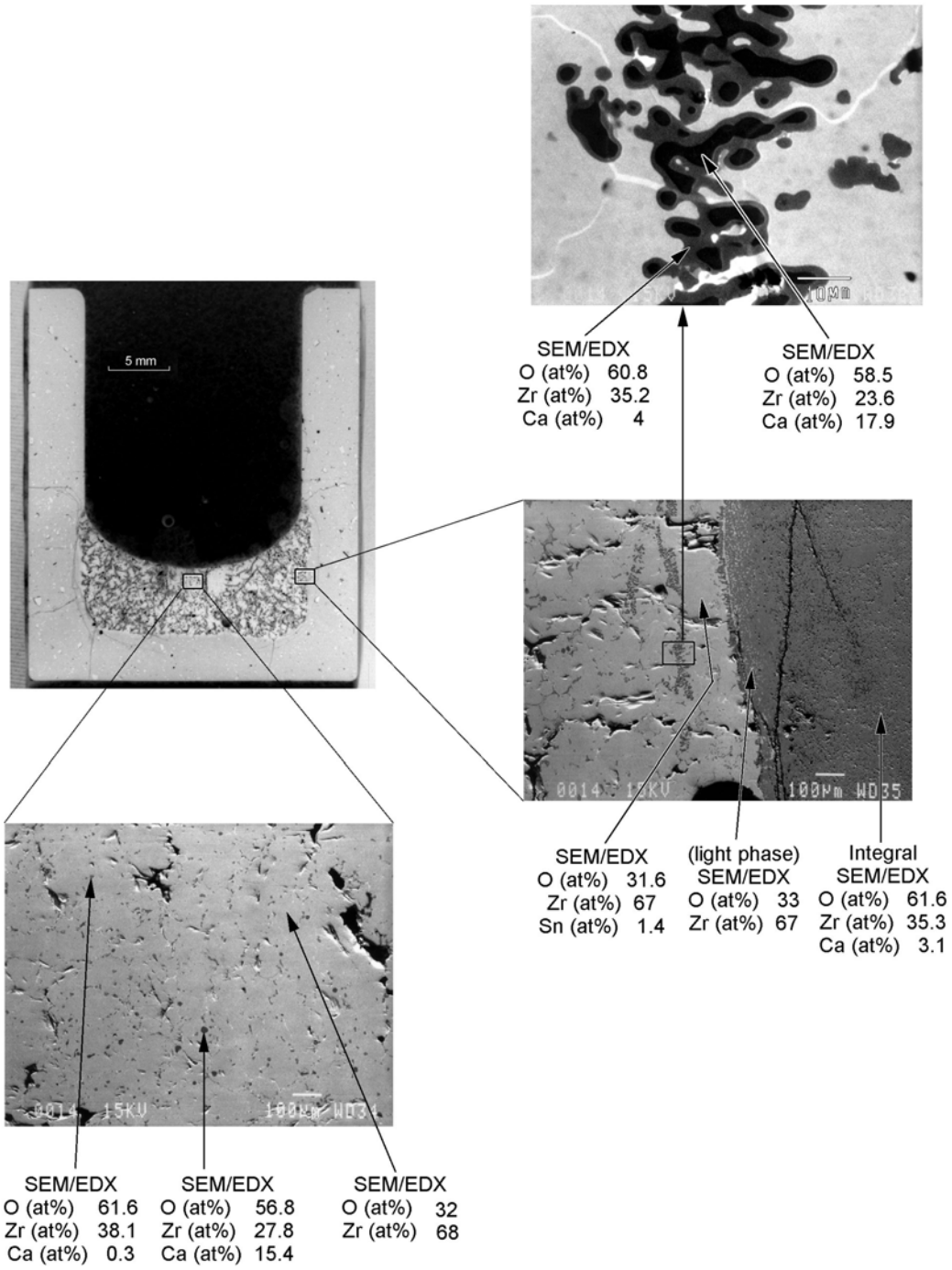

Fig. 32: Crucible #14 (2200°C, 102s)
SEM/EDX analysis

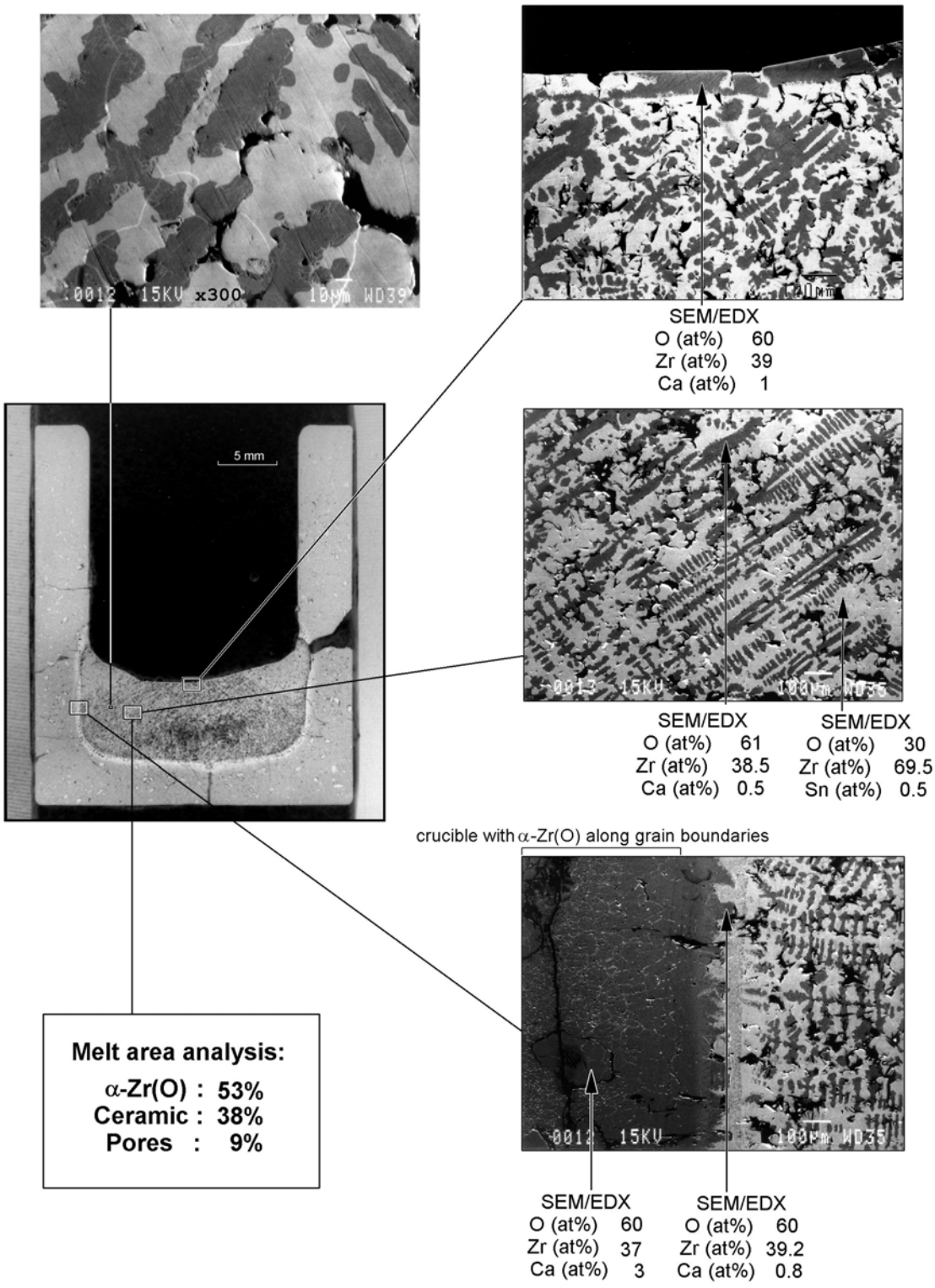

Fig. 33: Crucible #12 (2200°C, 587s)
Element and phase area analysis

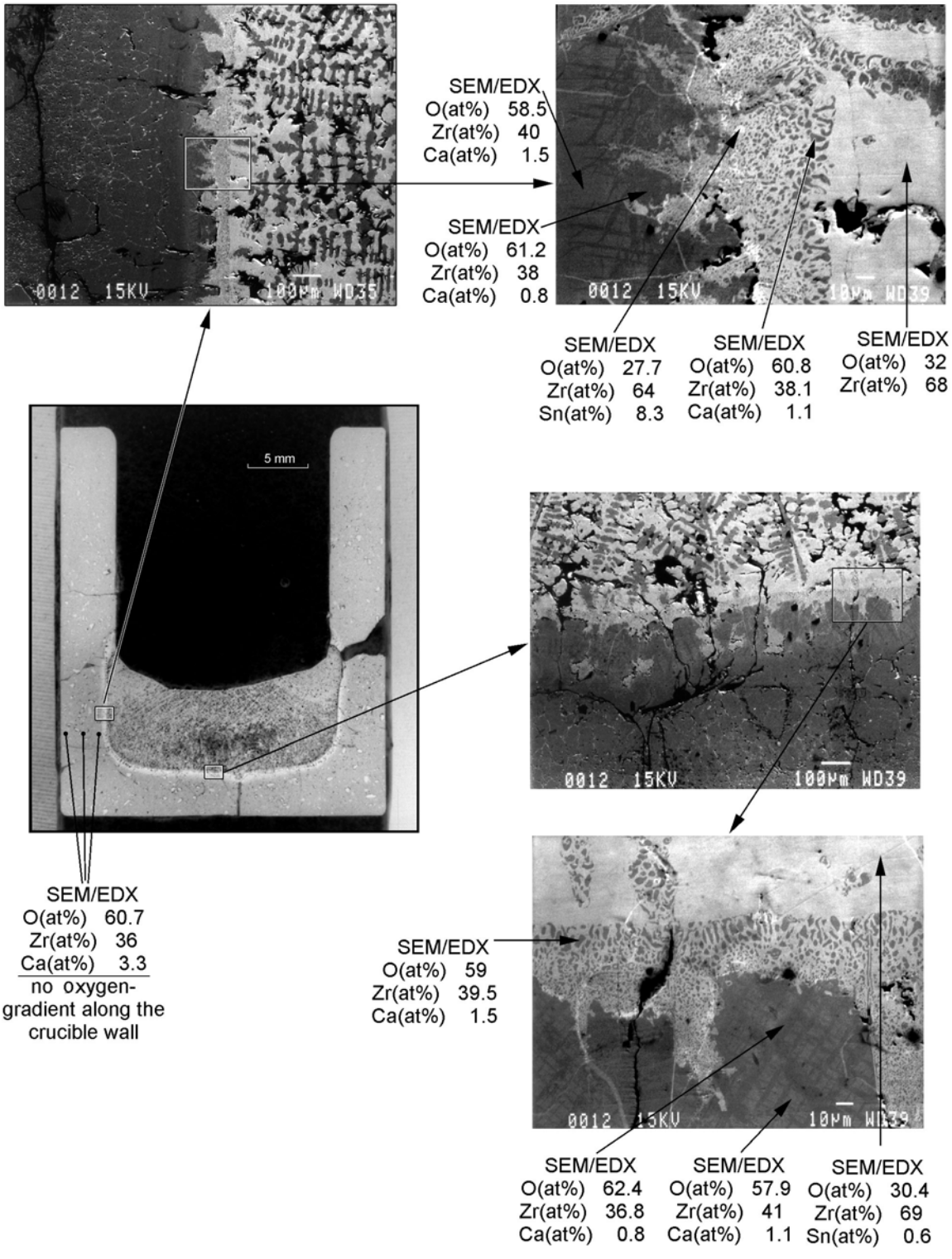

Fig. 34: Crucible #12 (2200°C, 587s). SEM/EDX analysis of the melt-crucible interaction zone

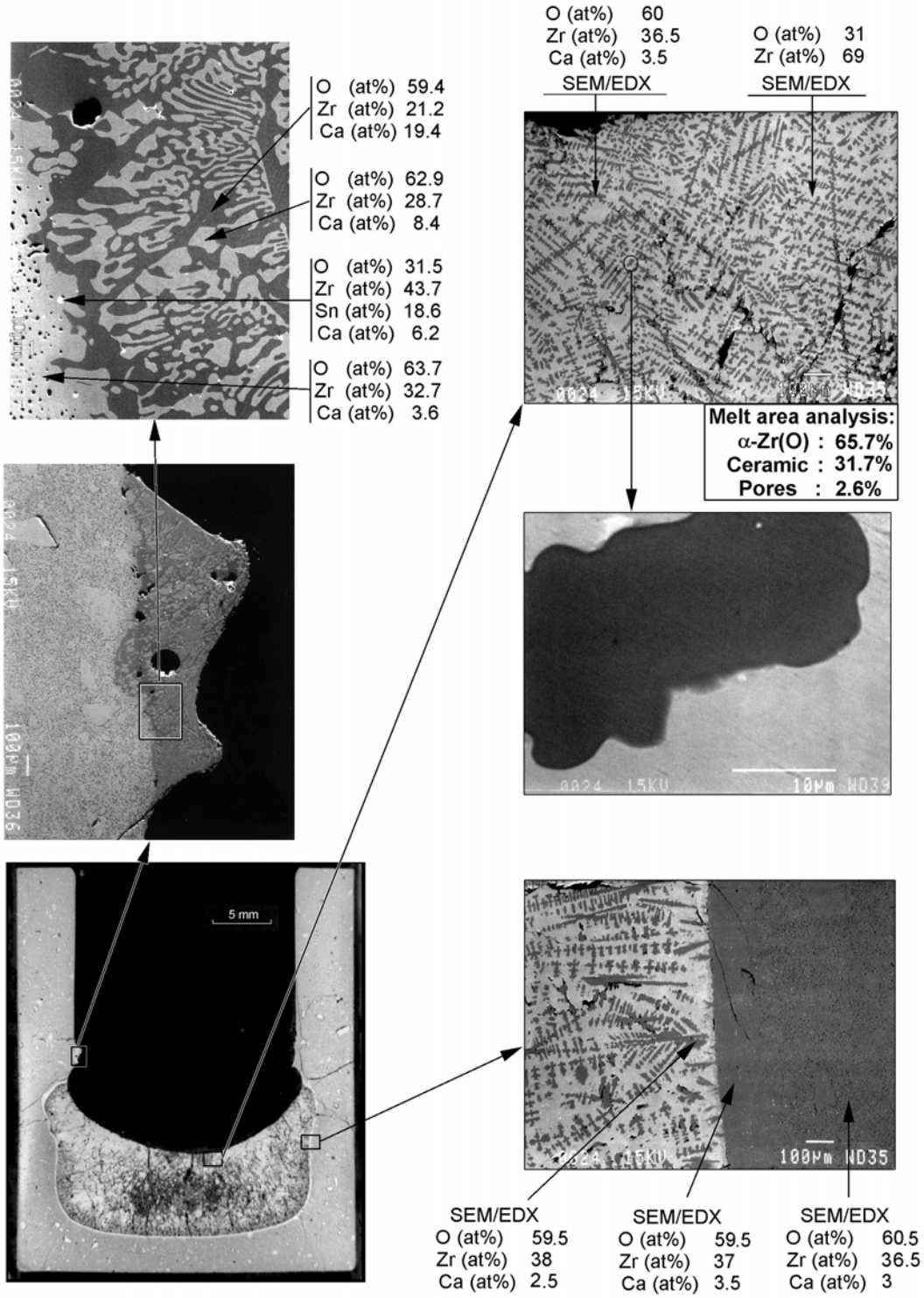

Fig. 35: Crucible #24 (2300°C, 121s)
Element and phase area analysis

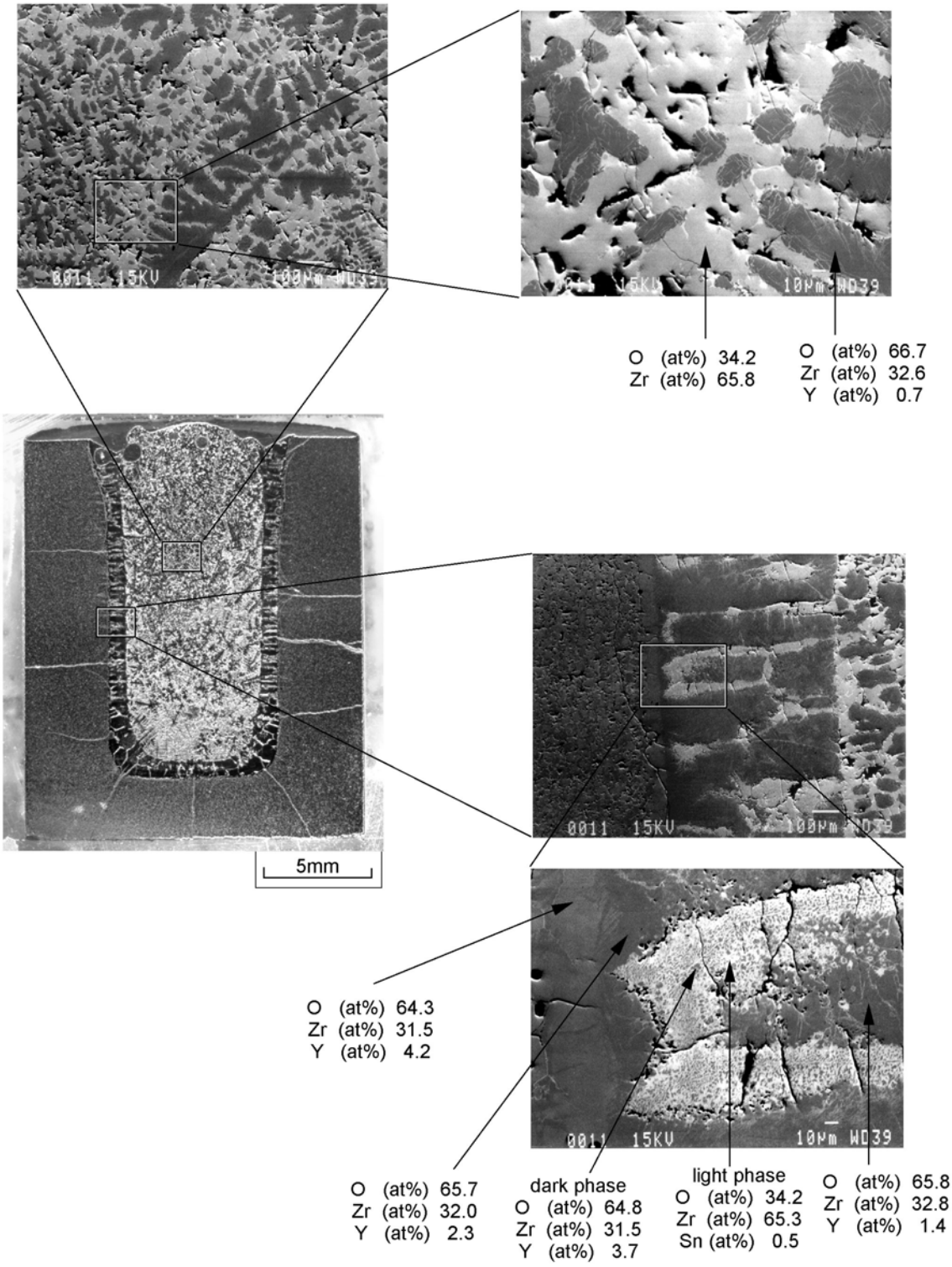

Fig.36: Crucible Z-11 (Canada)
T=2200°C, melt duration 612s. SEM/EDX analysis

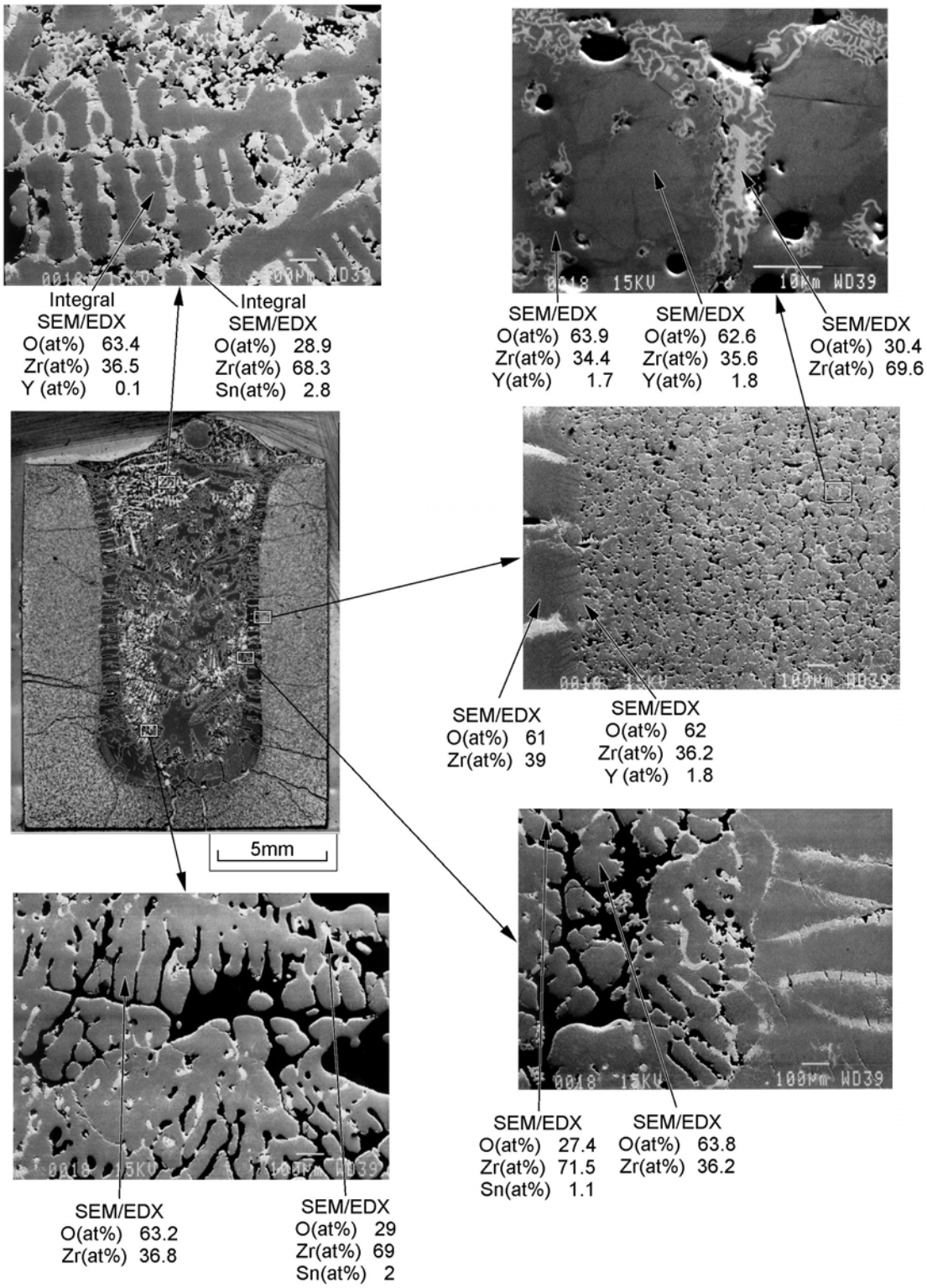

Fig. 37: Crucible Z-18 (Canada)
T=2300°C, melt duration 1195s. SEM/EDX analysis

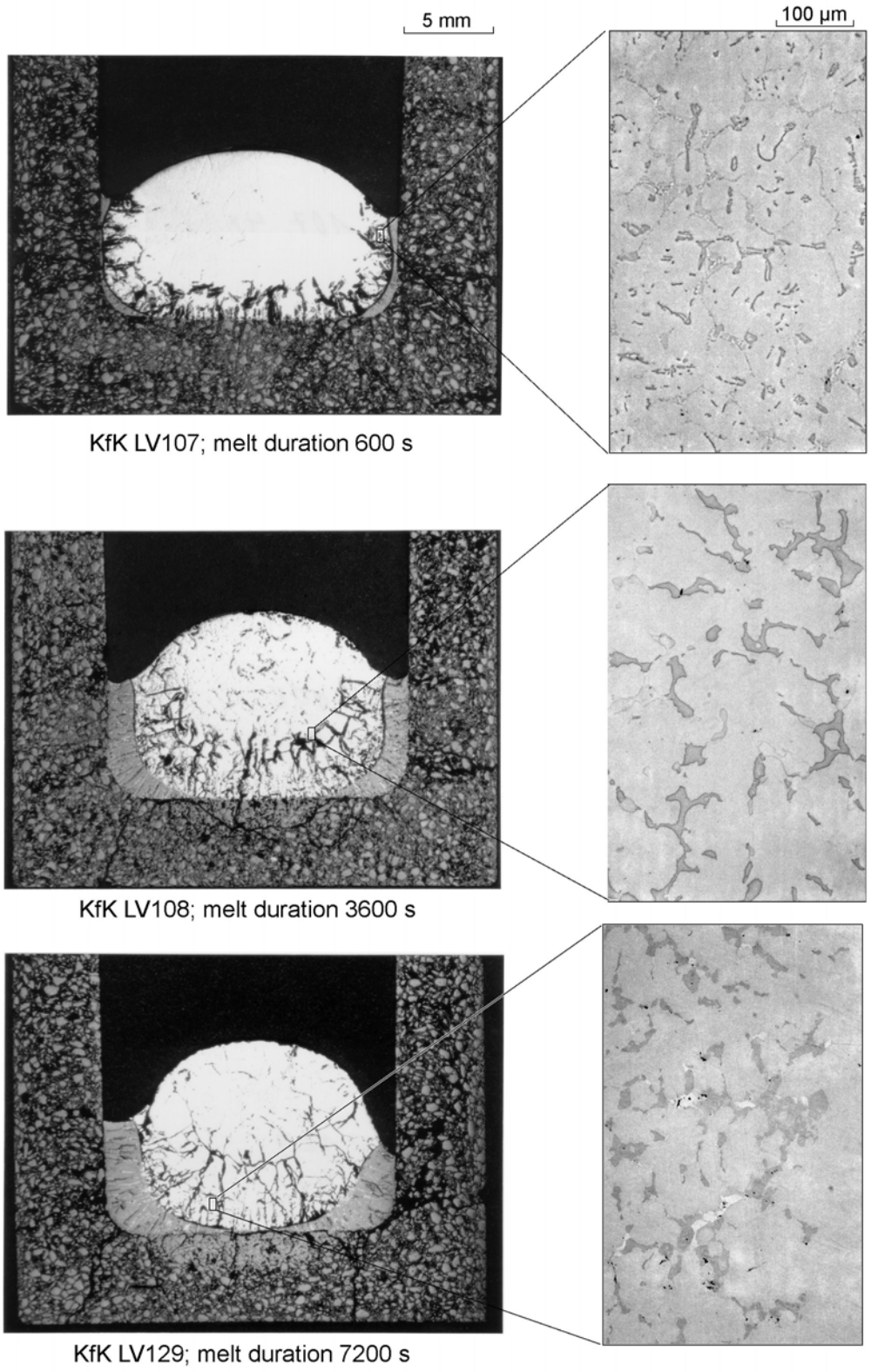

Fig. 38: Formation of precipitates in (Zr,O) melt at 1900°C in the KfK tests

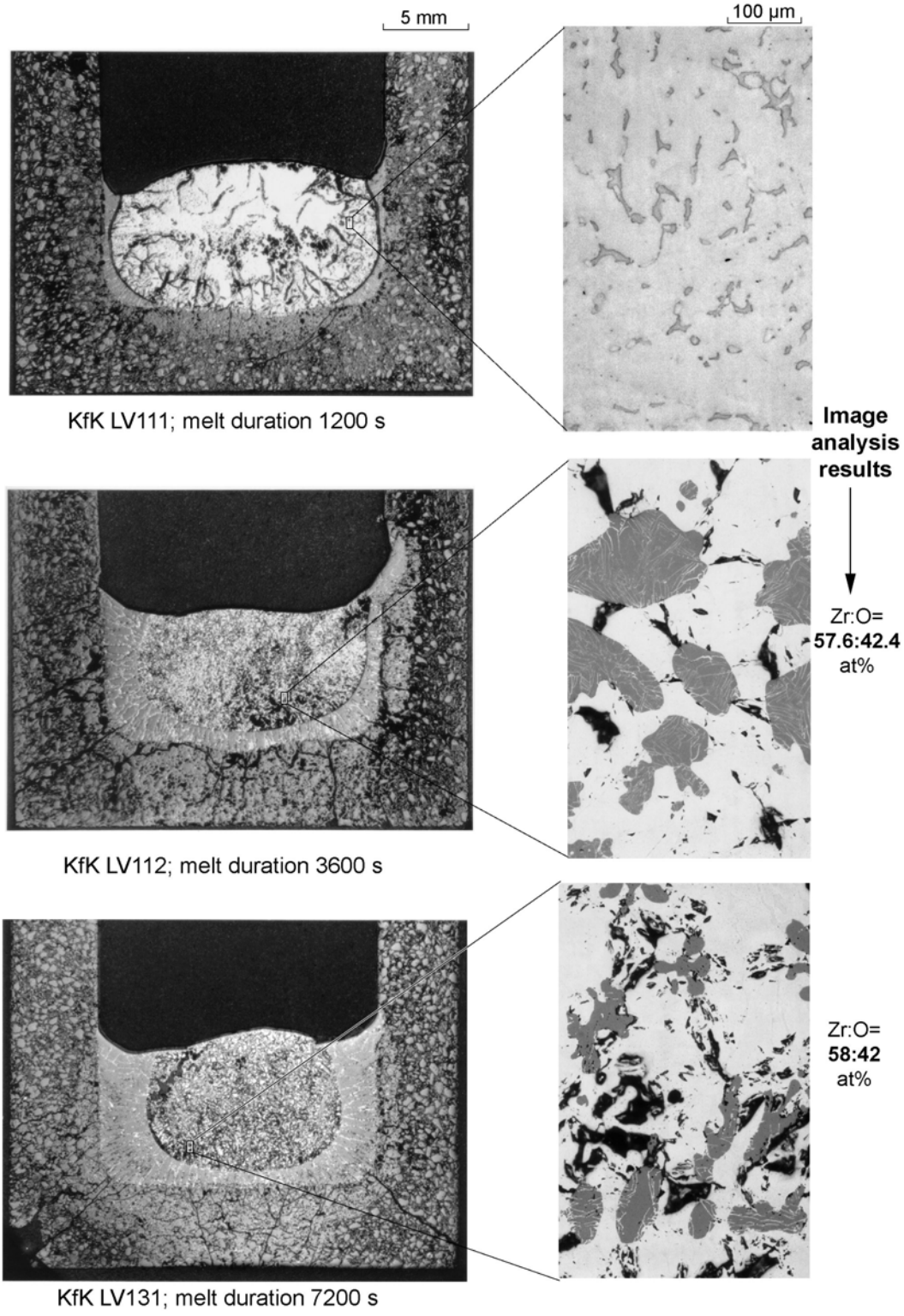

Fig. 39: Formation of precipitates in (Zr,O) melt at 2000°C in the KfK tests

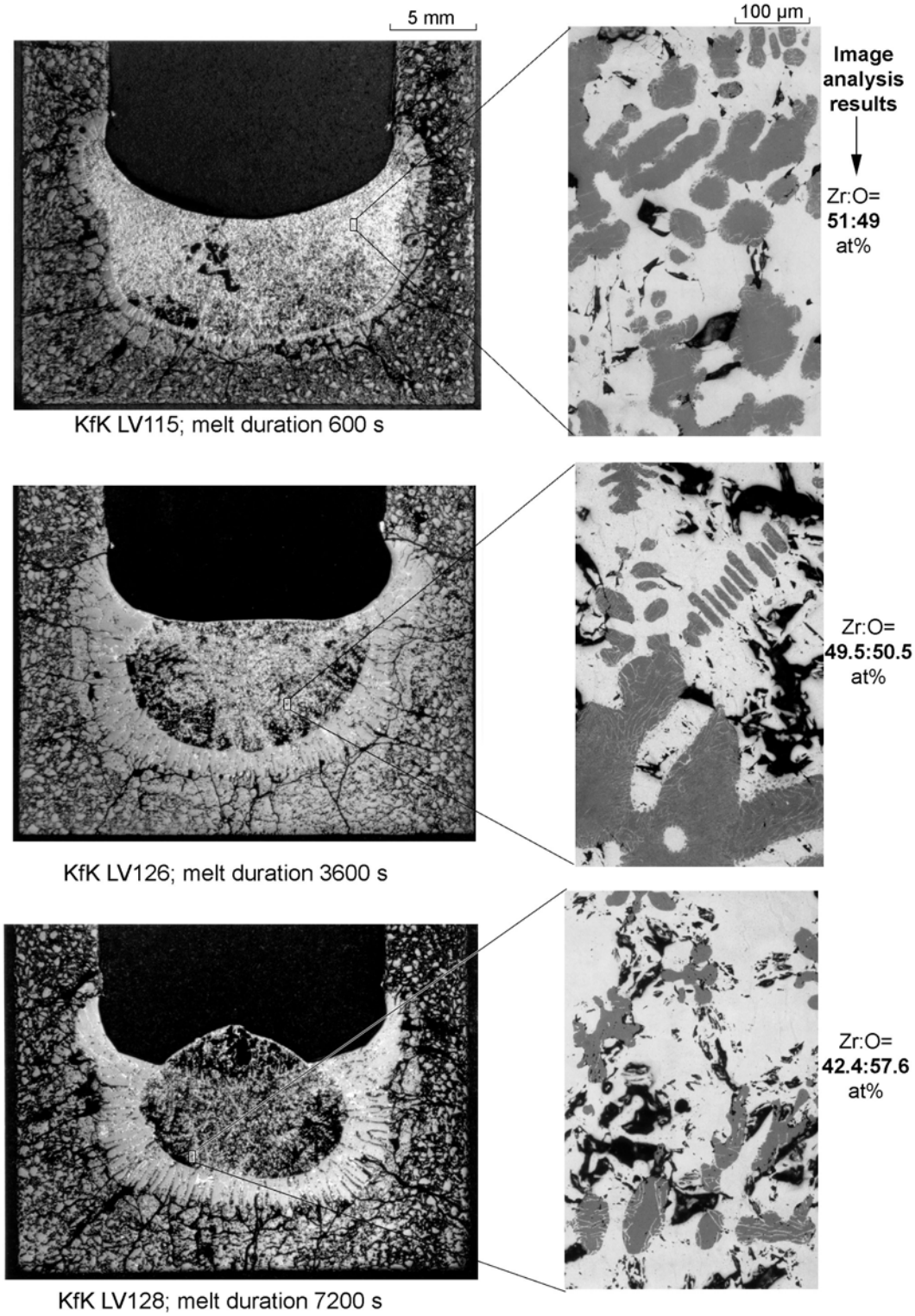

Fig. 40: Formation of precipitates in (Zr,O) melt at 2100°C in the KfK tests

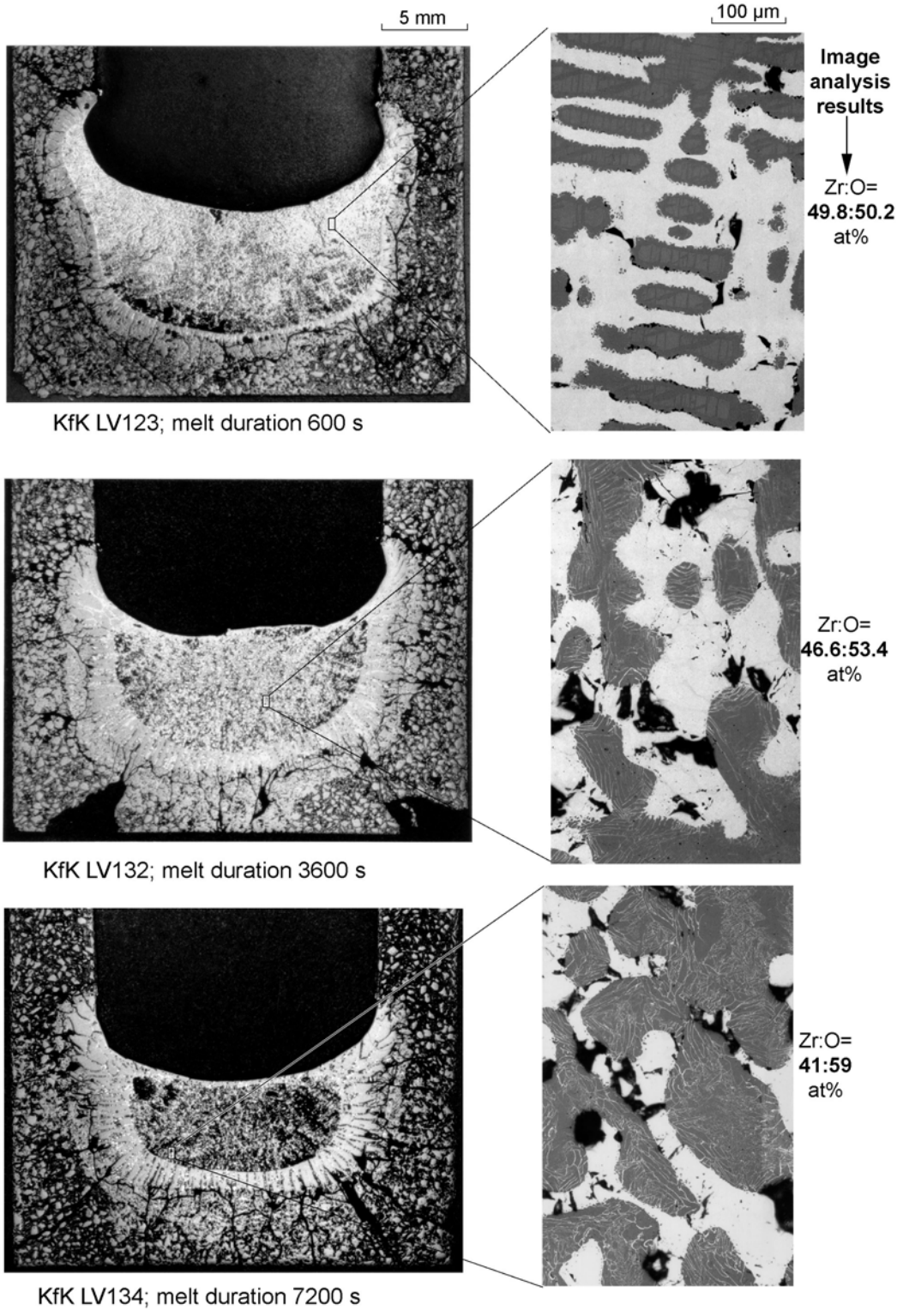

Fig. 41: Formation of precipitates in (Zr,O) melt at 2200°C in the KfK tests

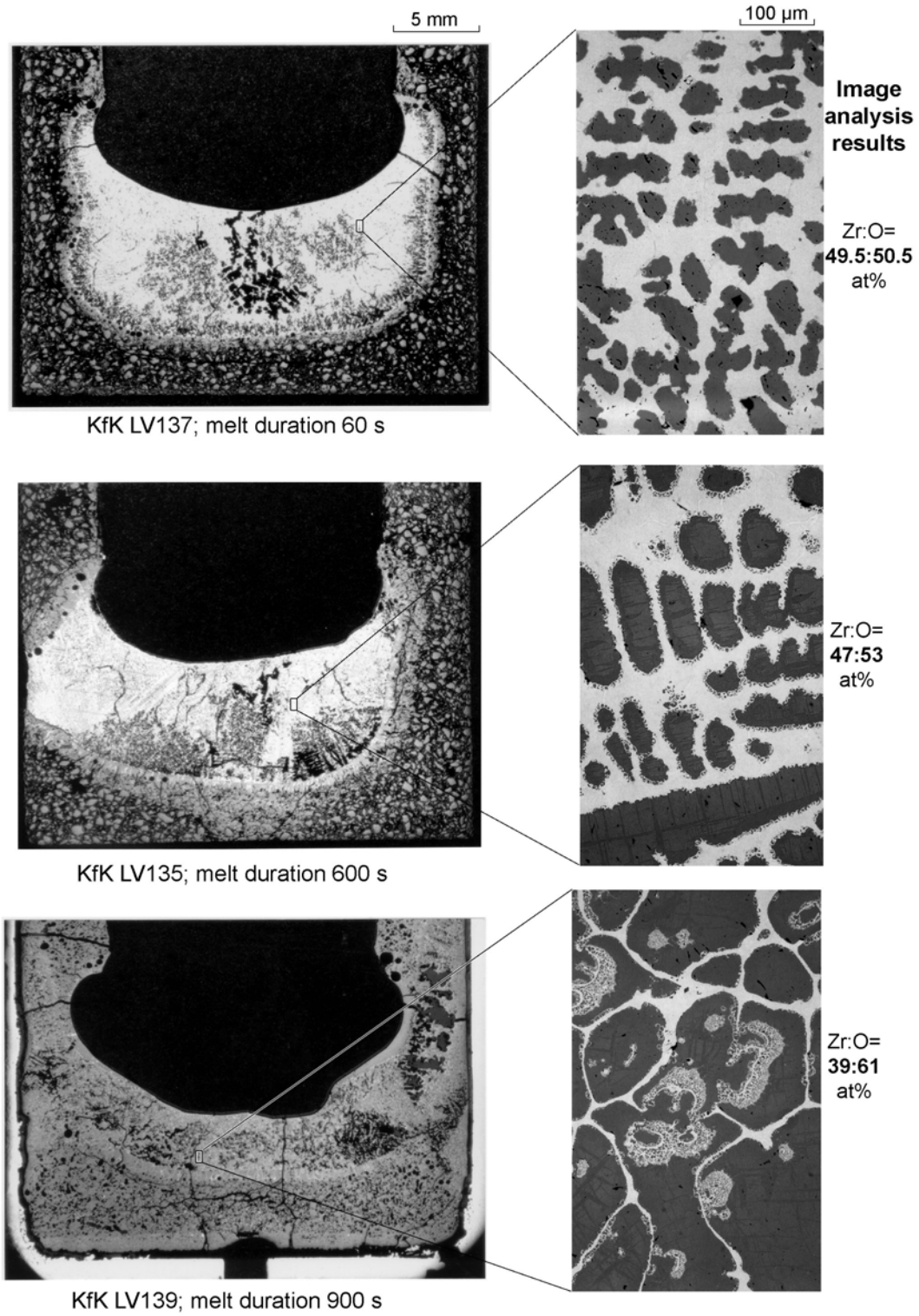

Fig. 42: Formation of precipitates in (Zr,O) melt at 2300°C in the KfK tests

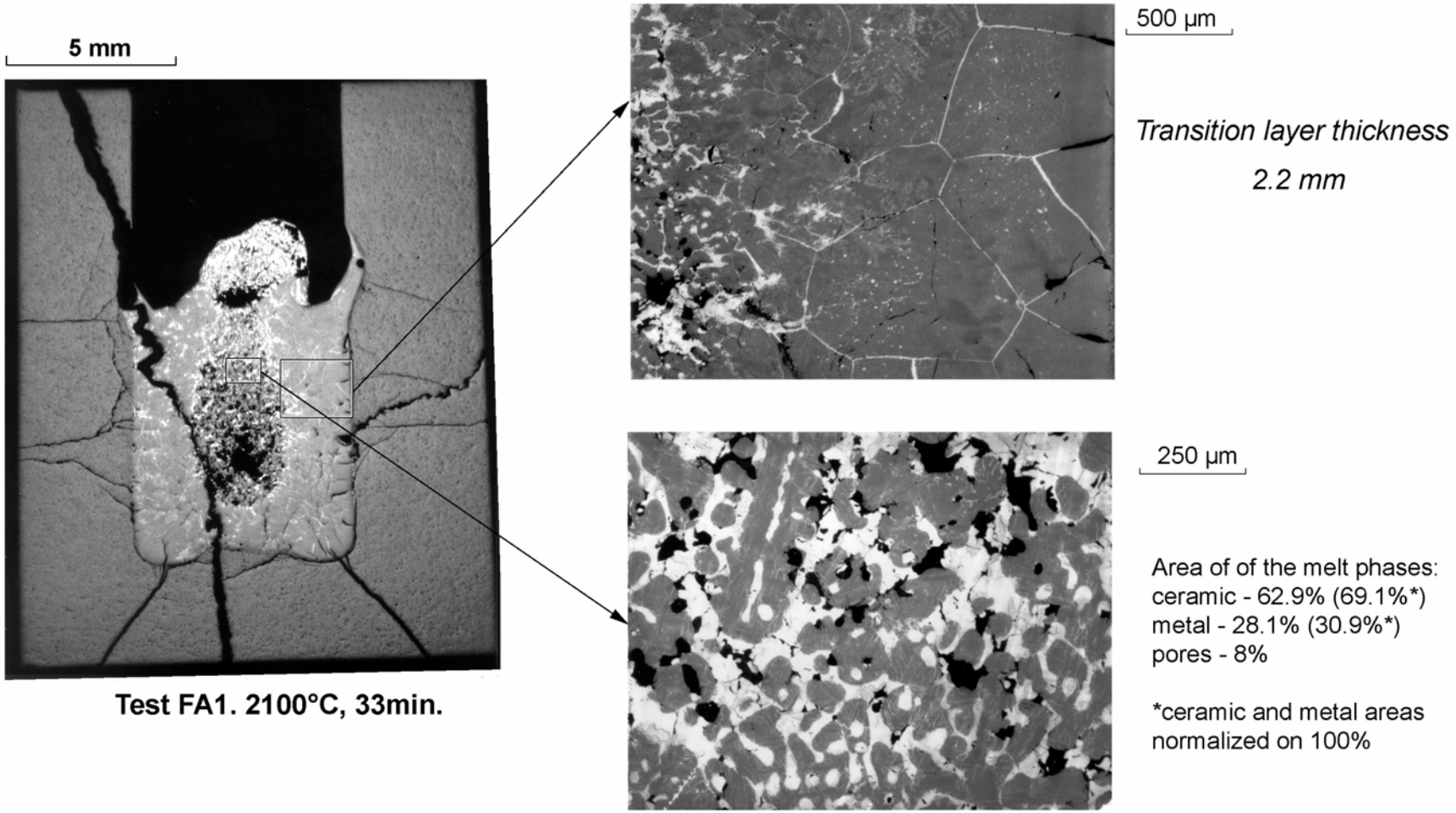

Fig. 43: FZK experiment FA1 with AECL crucible

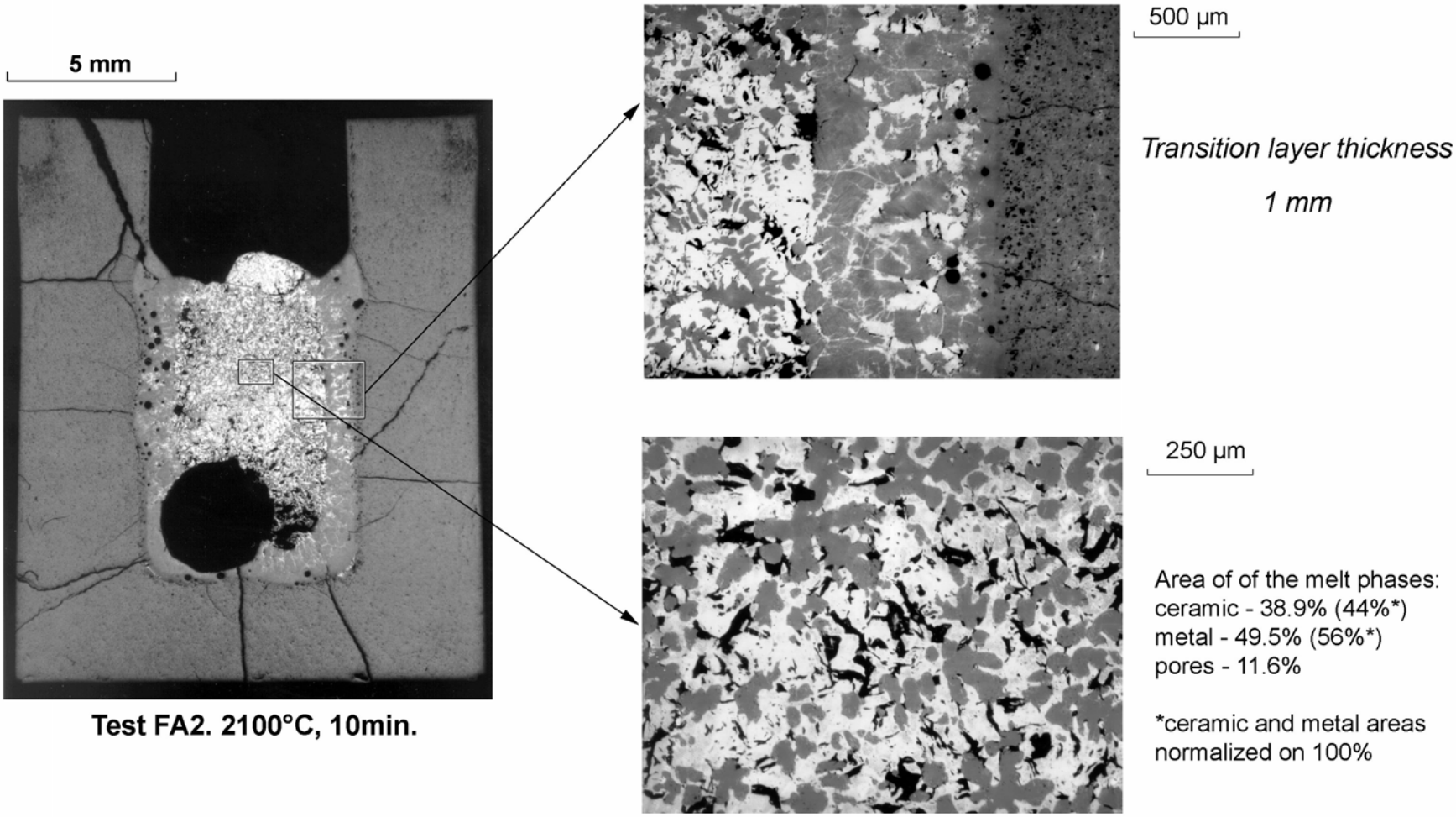

Fig. 44: FZK experiment FA2 with AECL crucible

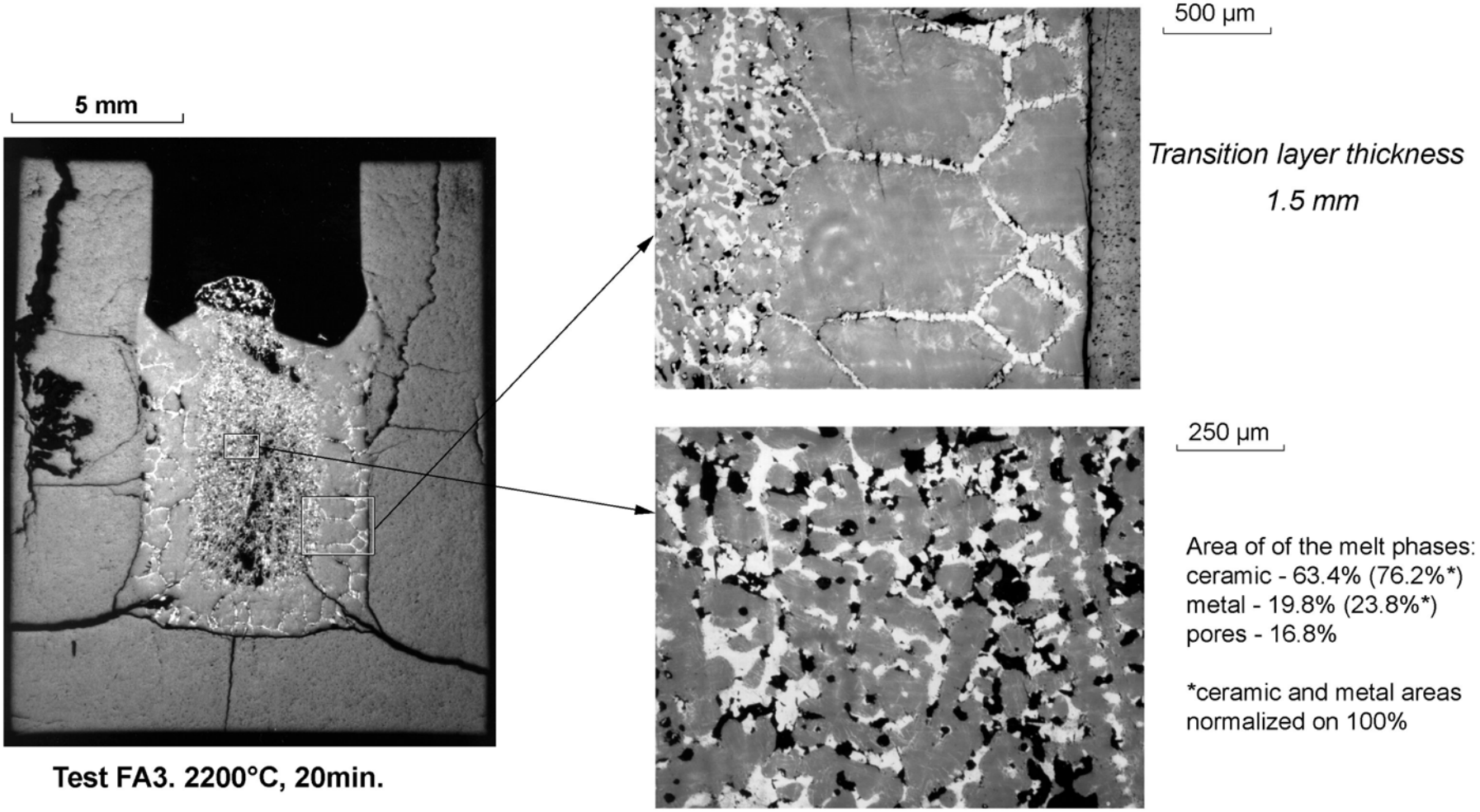

Fig. 45: FZK experiment FA3 with AECL crucible

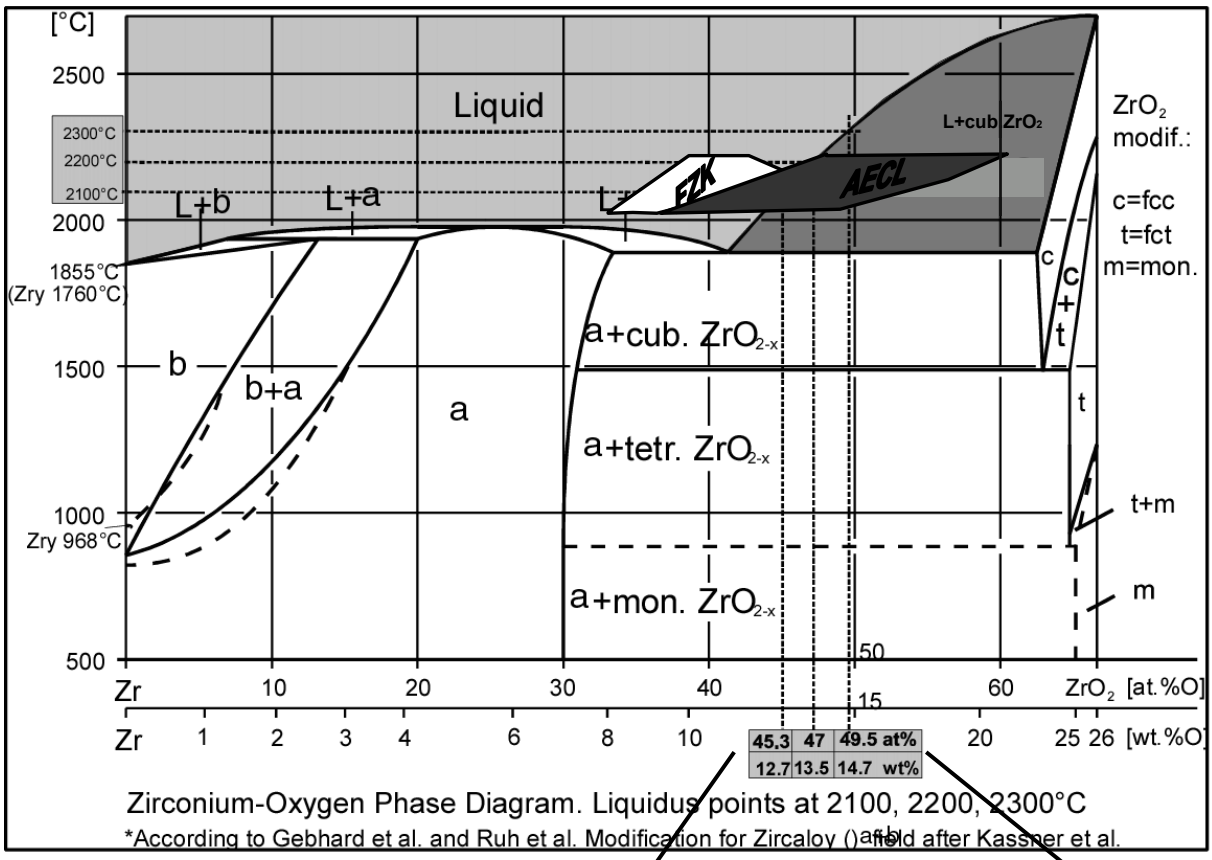

Zirconium-Oxygen Phase Diagram. Liquidus points at 2100, 2200, 2300°C

*According to Gebhard et al. and Ruh et al. Modification for Zircaloy () after Kassner et al.

Comparison of experimental results with the liquidus line of the Zr-O on a phase diagram

FZK

Nr	T °C	Melt duration s	Isoth. time s	Crucible bottom	**Ceramic phase %**	**Oxygen in the melt* wt%**
5	2100	101	90	Y_2O_3		
4	2100	574	570	Y_2O_3	**14**	**8.9**
7	2100	750	740	Y_2O_3	**13**	**8.7**
8	2100	1778	1770	Y_2O_3	**19**	**9.8**
13	2200	106	85	Y_2O_3	**10**	**8.2**
14	2200	102	93	no Y_2O_3	**4**	**7.1**
12	2200	587	552	no Y_2O_3	**41,8**	**14.1**
24	2300	121	67	no Y_2O_3	**32,5**	**12.4**

AECL

Nr	T °C	Melt duration s	Isoth. time s	**Ceramic phase %**	**Oxygen in the melt* wt%**
6	2100	116	41	**20**	**10.0**
4	2100	601	497	**38**	**13.4**
22	2100	1490	1384	**48**	**15.2**
23	2100	3585	3522	**68**	**18.9**
15	2200	136	64	**35**	**12.8**
11	2200	612	515	**46**	**14.9**
12	2200	1197	919	**61**	**17.6**
21	2200	1787	1692	**75**	**20.2**
19	2300	187	75	**53**	**16.2**
20	2300	599	485	**66**	**18.6**
18	2300	1195	1081	**86**	**22.3**
16	2300	1798	1662	**80**	**21.2**

In the column “Oxygen in the melt” the experiments with one-phase melts (liquid (Zr,O)) are presented as light-gray squares, the experiments with two-phase melts (liquid with precipitates of cubic ZrO_2) – as dark-gray squares. Numerical results in this columns are calculated results in accordance with the empirical formula O=0.26[(S+34)/1.4)], where S is the ceramic phase area (%) in the melt. The formula was derived from the analysis of the ceramic phase content in earlier dissolution experiments with known relationship between ZrO_2 and the resulting amount of ceramic precipitates in the melt.

Fig. 46: ZrO_2 dissolution experiments with one-phase and two-phase melts

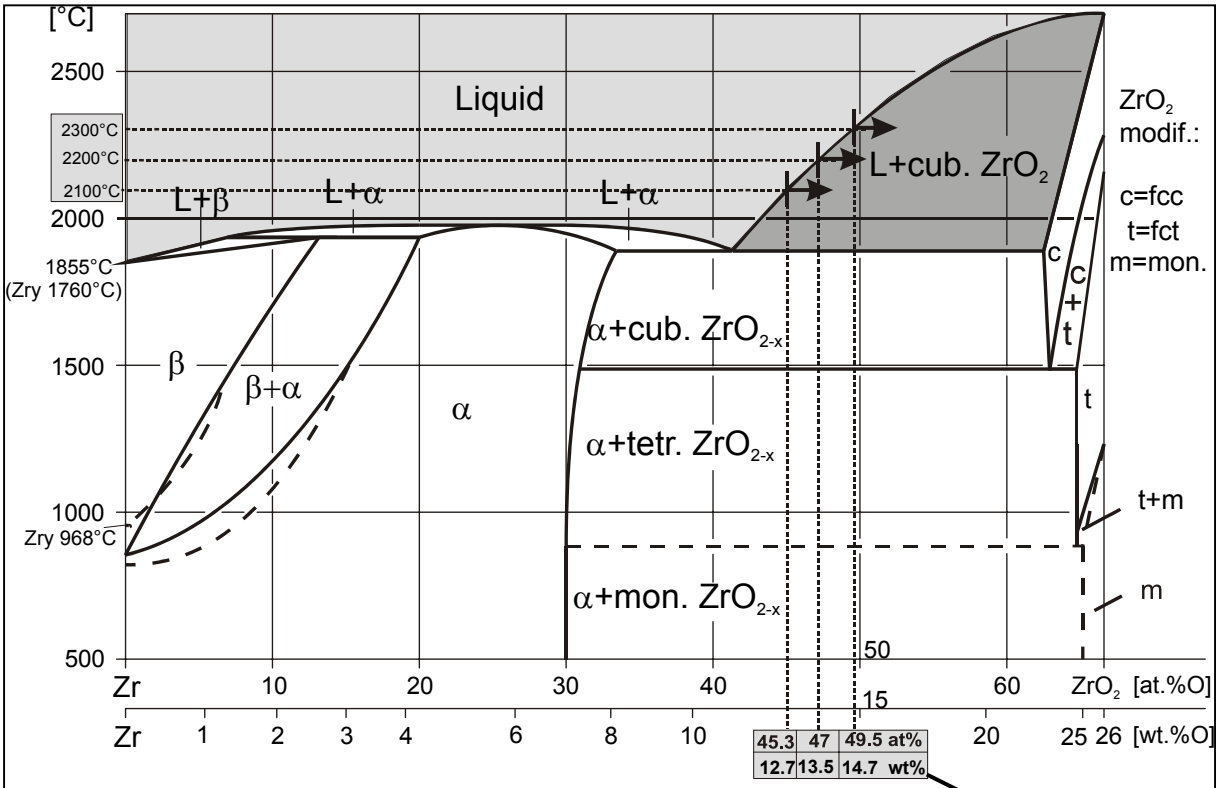

Zirconium-Oxygen Phase Diagram. Liquidus points at 2100, 2200, 2300°C

*According to Gebhard et al. and Ruh et al. Modification for Zircaloy (α+β) field after Kassner et al.

Comparison of experimental results with the liquidus line of the Zr-O on a phase diagram

No	T°C	t, s	α-Zr(O), %	microvoids, %	ceramic, %	Oxygen, wt%
LV112d	2000	3600	67.8	5.9	26.3	11.20
LV131	2000	7200	63.9	12.4	23.7	10.72
LV113	2100	60	89	0.6	10.4	8.25
LV114	2100	180	76.7	0.03	23.27	10.64
LV115	2100	600	53.9	4.2	41.9	14.10
LV127	2100	1800	50.2	8.3	41.5	14.02
LV126	2100	3600	45.2	14.11	40.69	13.87
LV128	2100	7200	27.3	11.2	61.5	17.74
LV133	2200	60	87.8	5	7.2	7.65
LV121	2200	180	65.6	0.4	34	12.63
LV123	2200	600	51.8	1.7	46.5	14.95
LV124	2200	1800	33.6	6.1	60.3	17.51
LV132	2200	3600	39.8	9.4	50.8	15.75
LV134	2200	7200	22.6	7.6	69.8	19.28
LV137	2300	60	36.9	20	43.1	14.32
LV137	2300	60	50.9	1.2	47.9	15.21
LV125	2300	180	44.5	1.1	54.4	16.42
LV135	2300	600	43.6	0.2	56.2	16.75
LV139	2300	900	17.3	0.5	82.2	21.58
LV141	2400	180	20	1	79	20.99

*In the column “Oxygen in the melt” the experiments with one-phase melts (liquid (Zr,O)) are presented as light-gray squares, the experiments with two-phase melts (liquid with precipitates of cubic ZrO_2) – as dark-gray squares.

Fig. 47: KfK experiments with and without precipitates in the melt

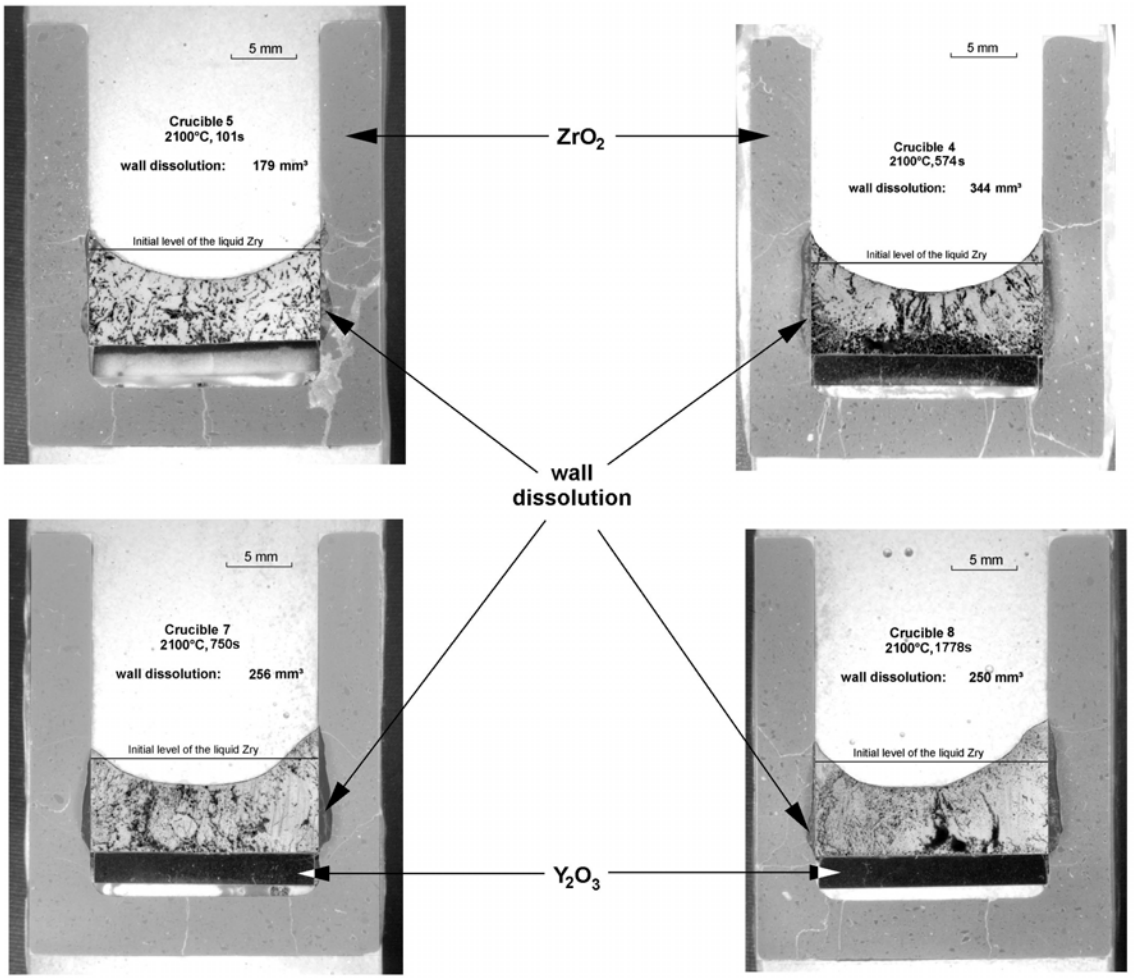

Fig. 48: Dissolved areas of crucibles after dissoluton tests at 2100°C

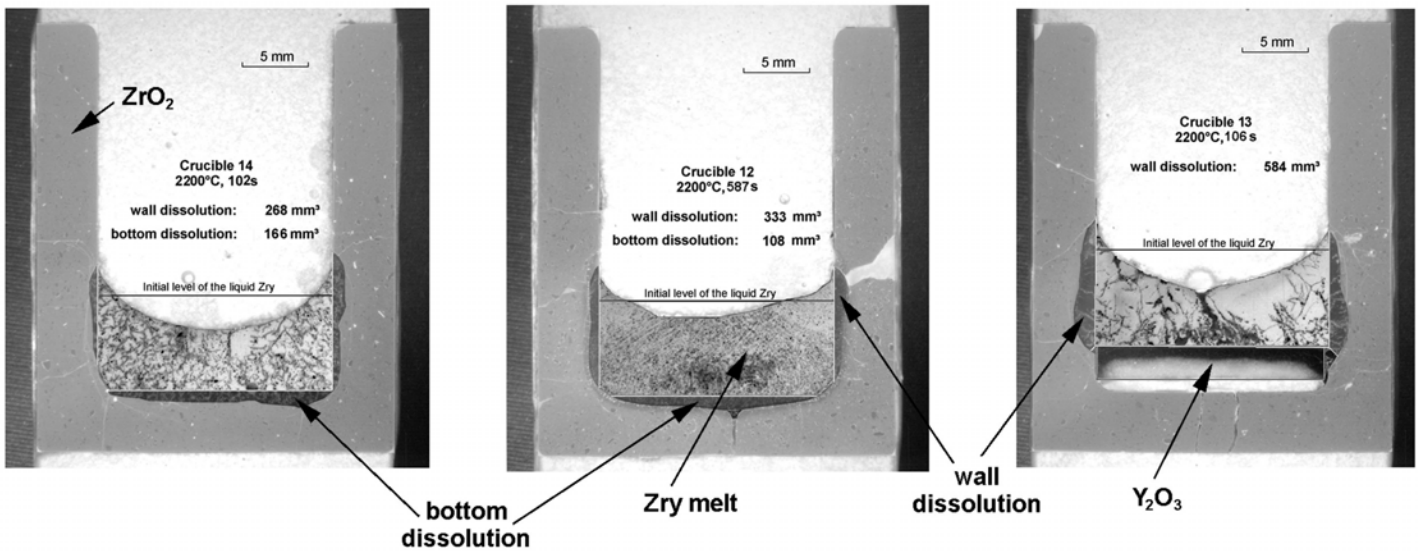

Fig. 49: Dissolved areas of crucibles after dissoluton tests at 2200°C

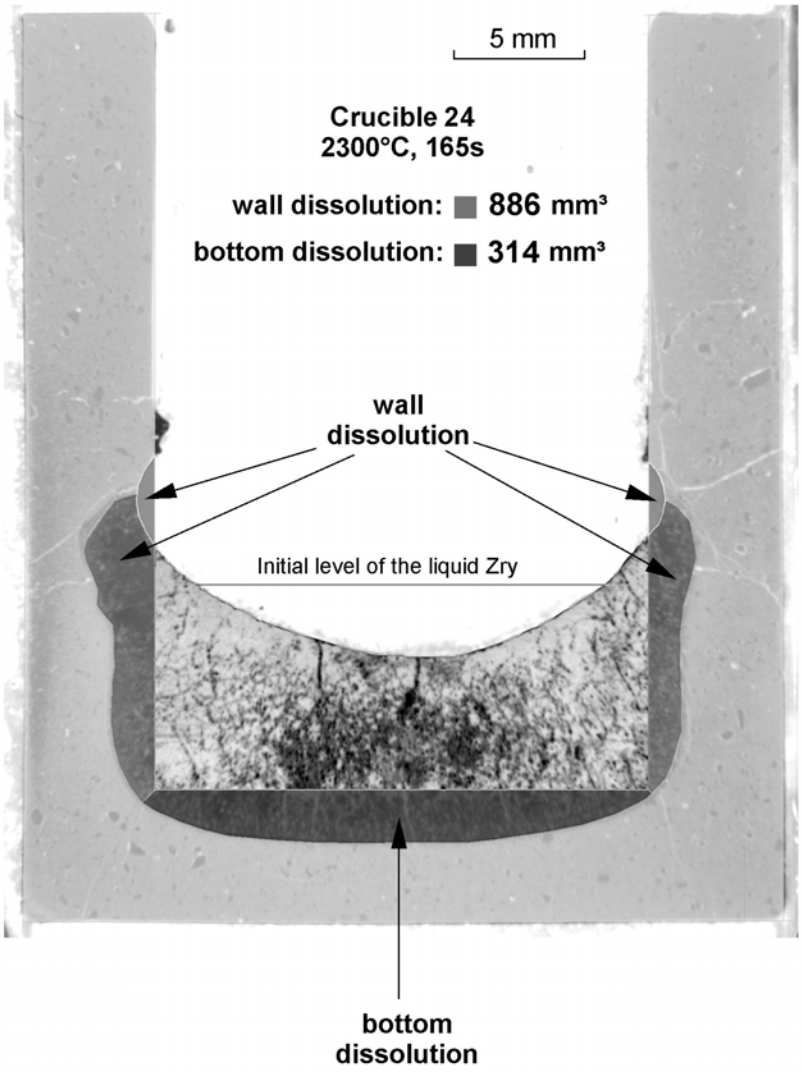

Fig. 50: Dissolved areas of crucible after dissoluton test at 2300°C

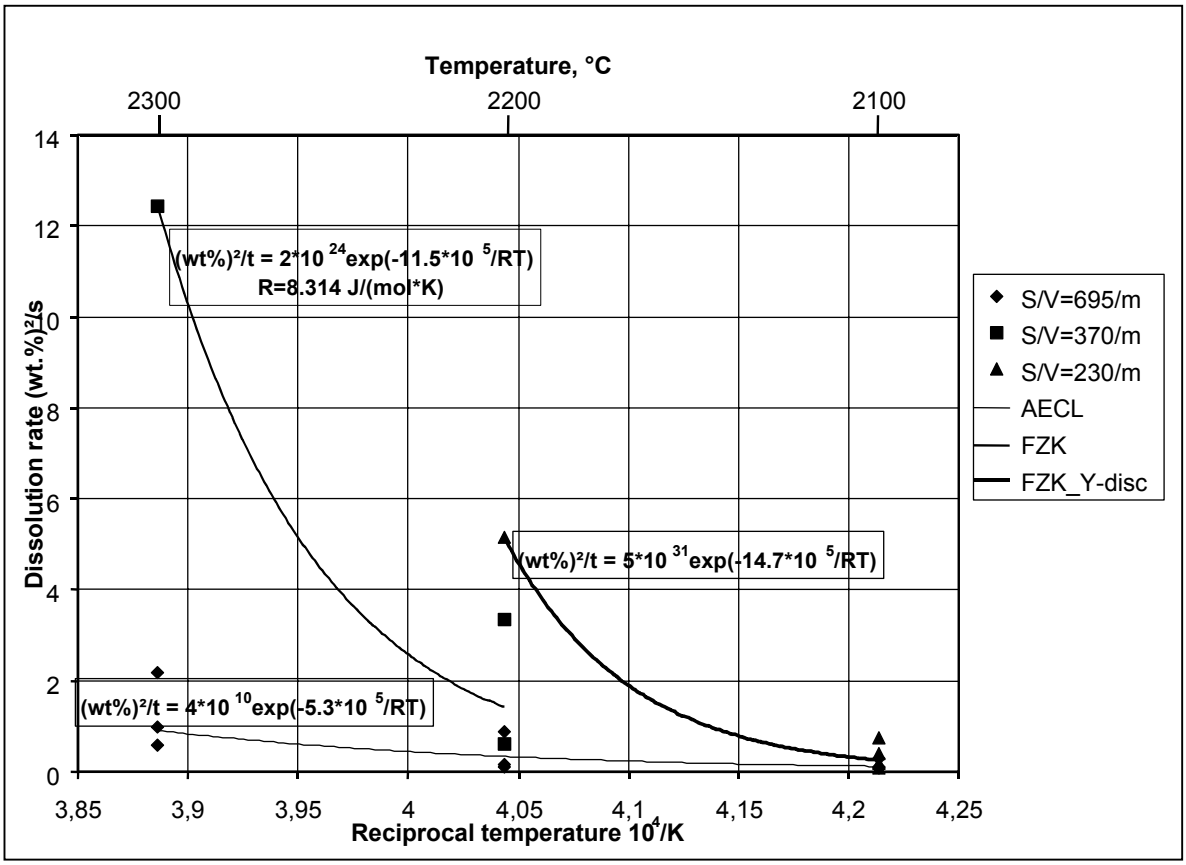

Fig. 51: Arrhenius representation of the ZrO_2 dissolution rate by molten Zircaloy

Oxygen content in the melt, wt%

Crucible	#4	#7	#8	#14	#13	#12	#24
Image anal.	8.9	8.7	9.8	7.1	8.2	14.1	12.4
Chemistry	9.81±0.26		11.27±1	7.30±0.22	8.57±0.06	13.25±0.82	12.4±0.45

Image analysis errror: ±0.8wt%.

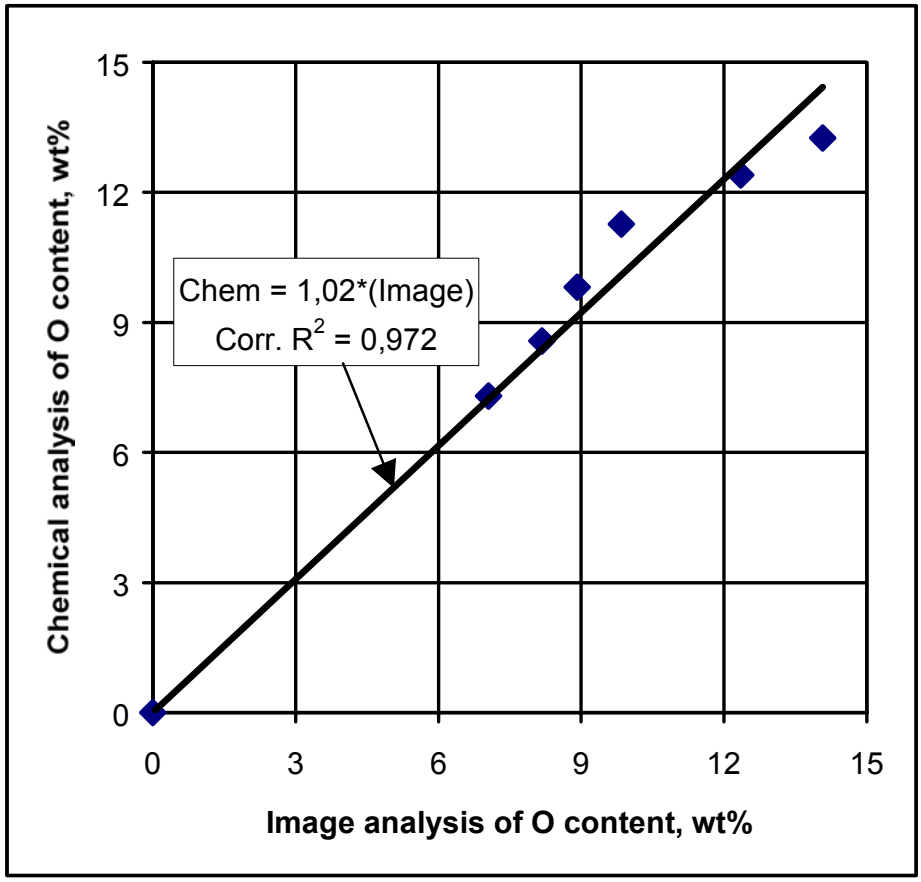

Fig. 52: Comparison between 2 methods of oxygen content determination in the melt

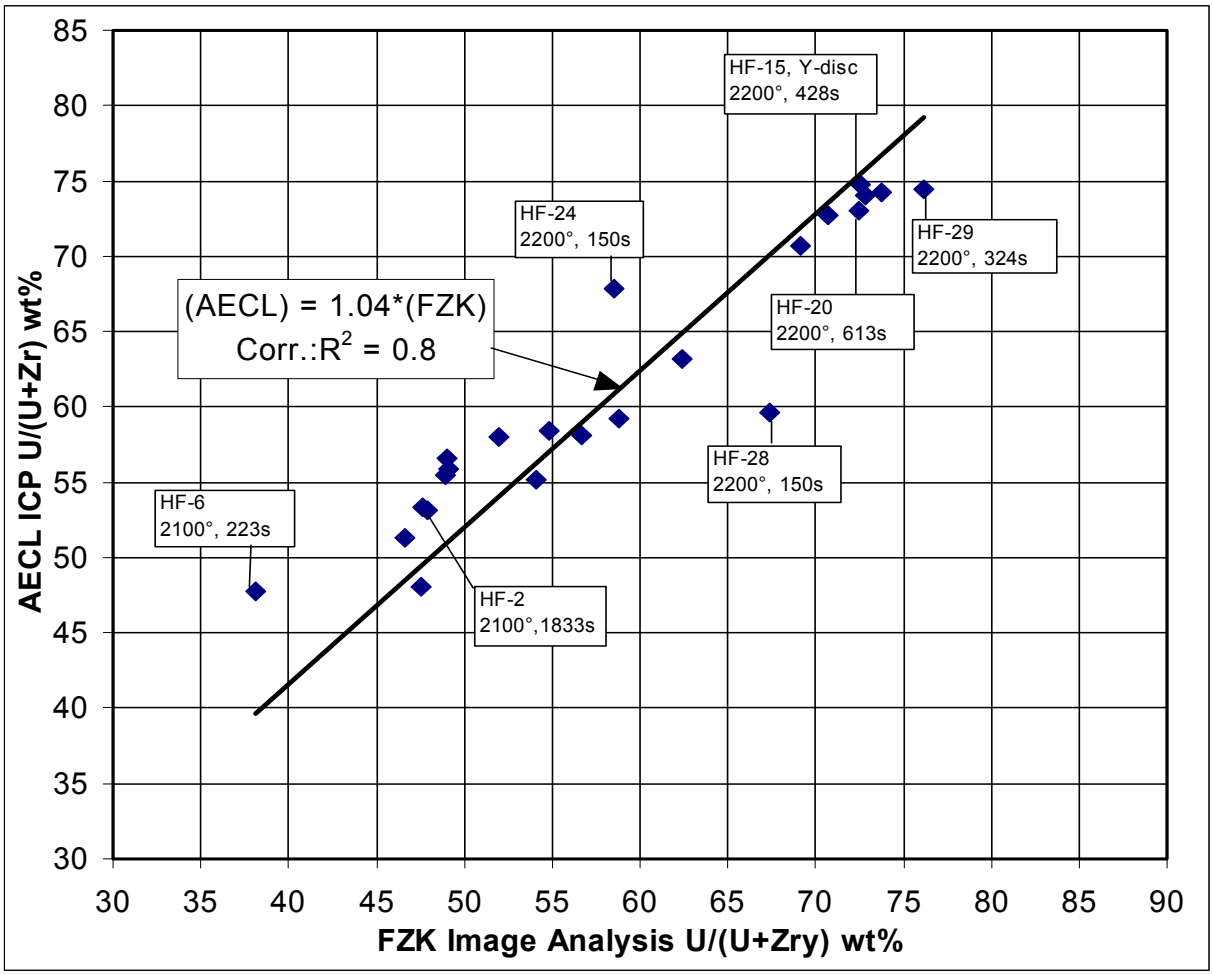

Fig. 53: Comparison between the chemical analysis results and the image analysis estimation of uranium content in the melt for UO_2 dissolution tests

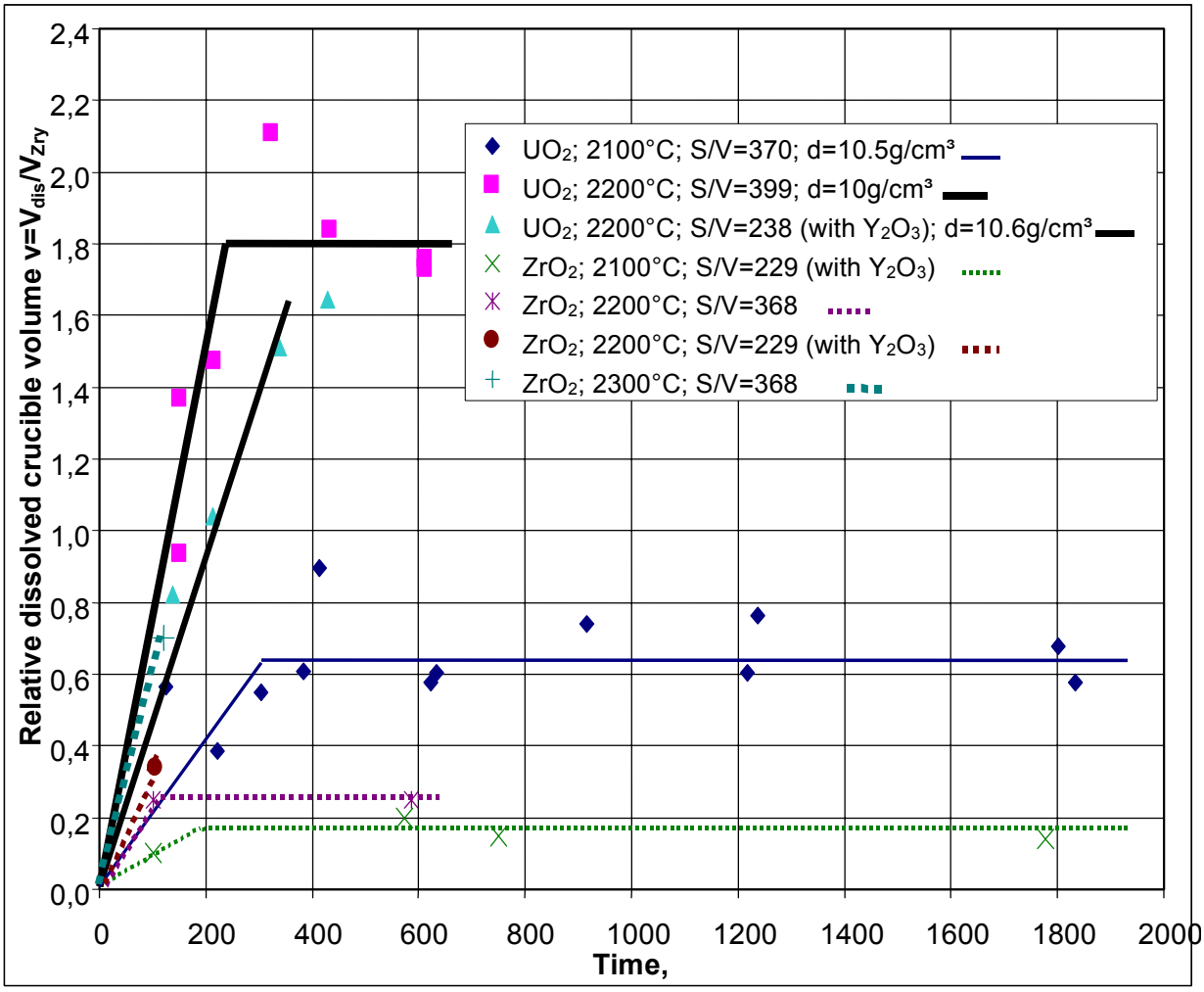

Fig. 54: Comparison of the results of dissolution tests
with ZrO_2 and UO_2 crucibles

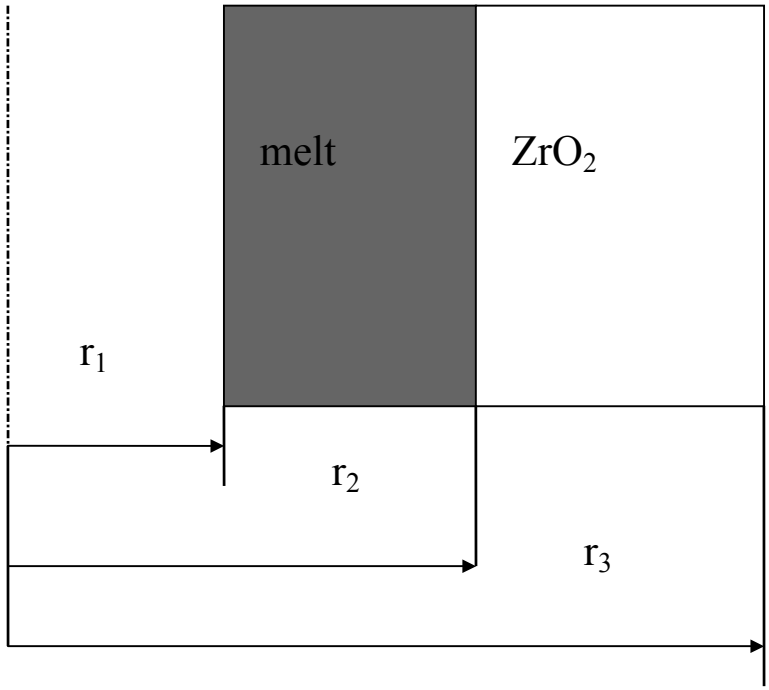

Fig. 55: Schematic representation of the two interaction layers in the ZrO_2/(molten Zry) system

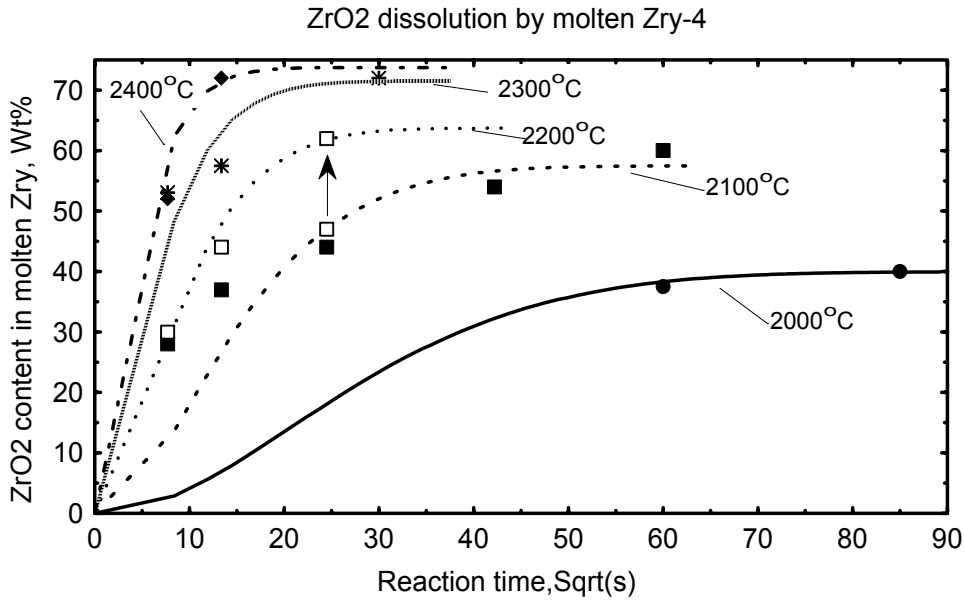

Fig. 56: ZrO_2 weight content in the liquid phase.
Validation of the model against KfK test data, corrected by the new FZK post-test analysis (arrow at 2200°C).

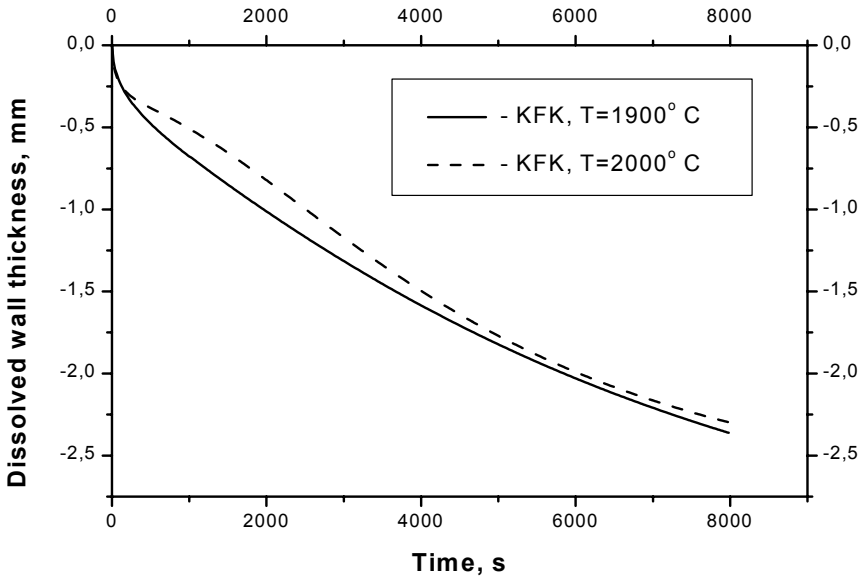

Fig. 57: Simulations of KfK tests on ZrO_2 crucible dissolution by molten Zry: growth of the interface oxide layer at 1900 and 2000°C

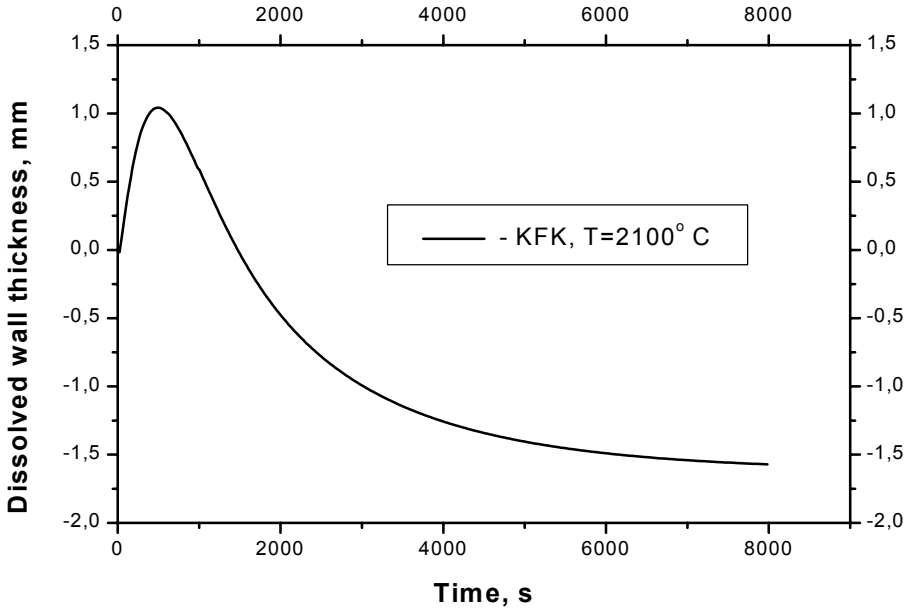

Fig. 58: Simulations of KfK tests on ZrO_2 crucible dissolution by molten Zry: erosion (dissolution) and corrosion (oxide layer growth) at 2100°C

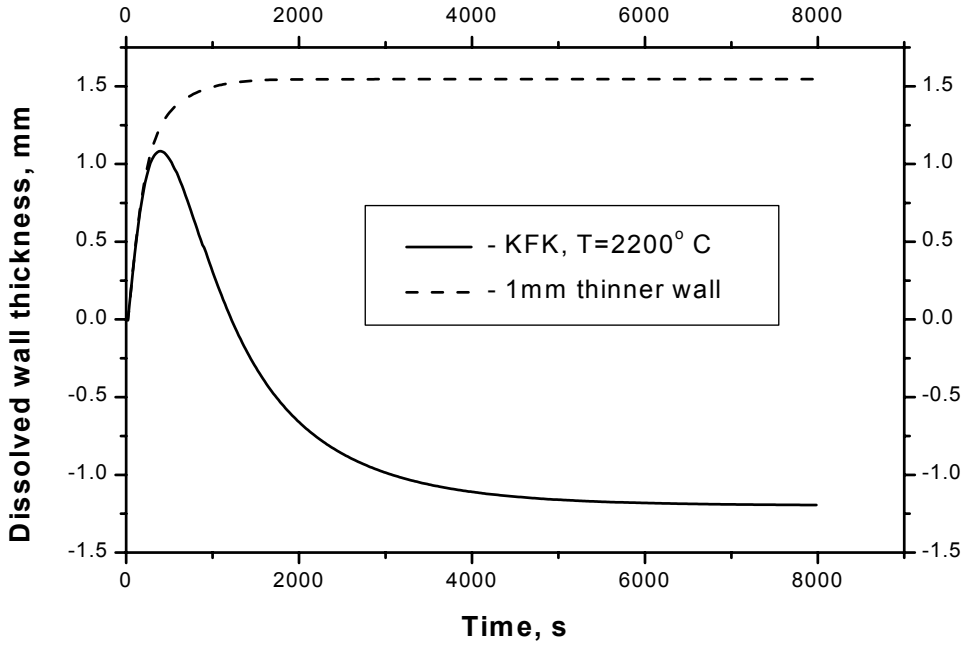

Fig. 59: Simulations of KfK tests on ZrO_2 crucible dissolution by molten Zry: erosion and corrosion at 2200°C. Additional calculation with a thinner crucible wall (4 mm) is presented for comparison.

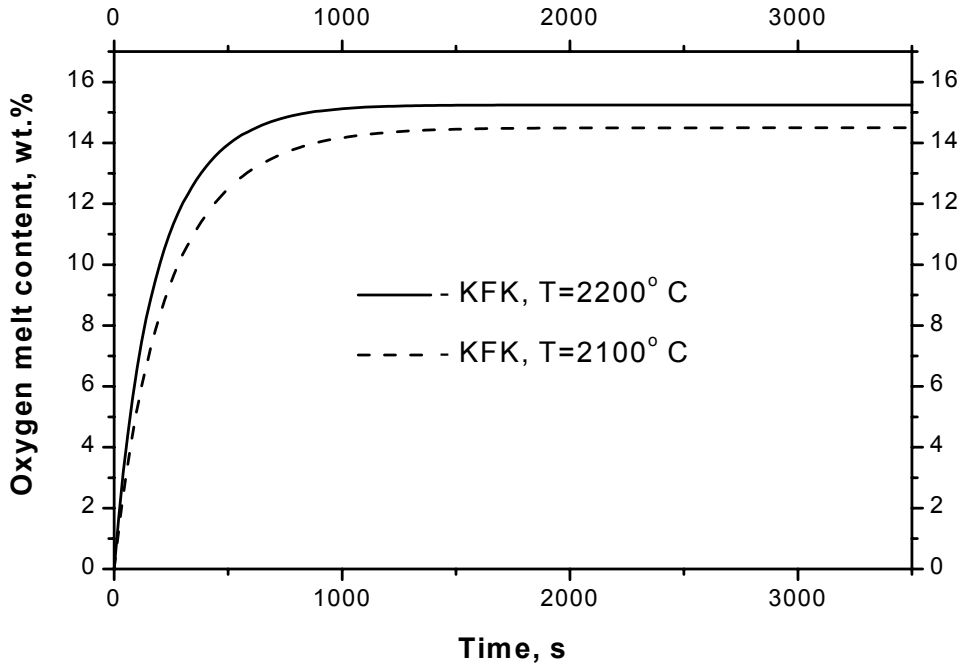

Fig. 60: Simulations of oxygen melt content evolution in KfK tests on ZrO_2 crucible dissolution by molten Zry at 2100 and 2200°C

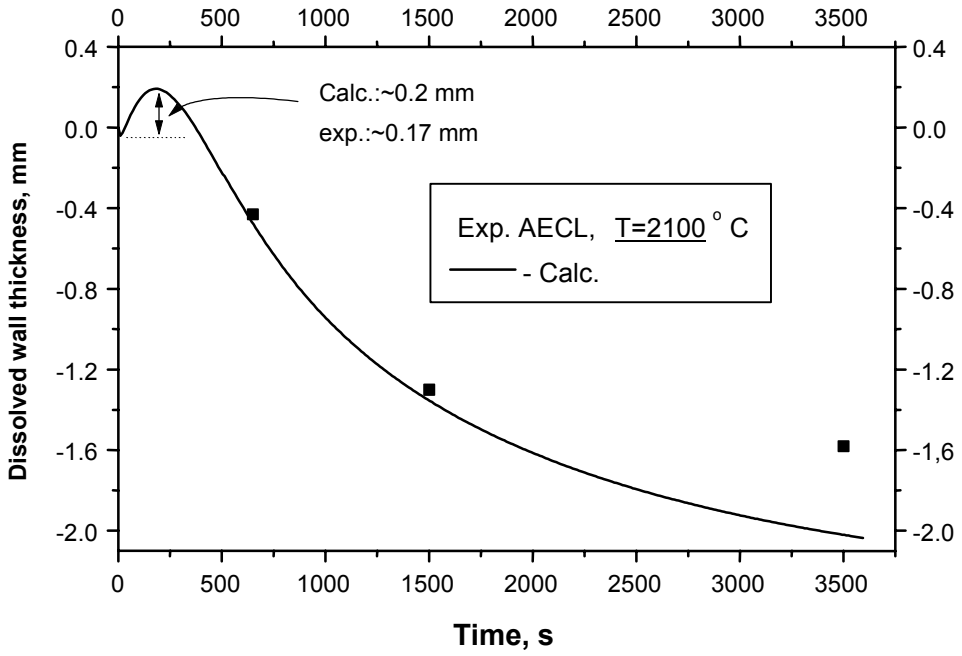

Fig. 61: Simulations of AECL tests on ZrO_2 crucible dissolution by molten Zry: erosion and corrosion at 2100°C

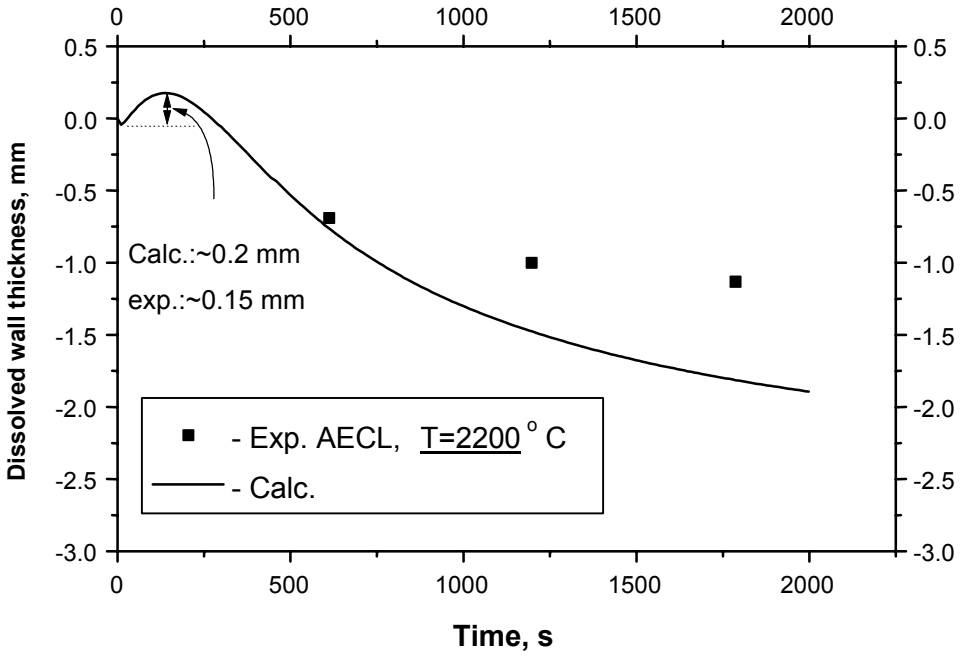

Fig. 62: Simulations of AECL tests on ZrO_2 crucible dissolution by molten Zry: erosion and corrosion at 2200°C

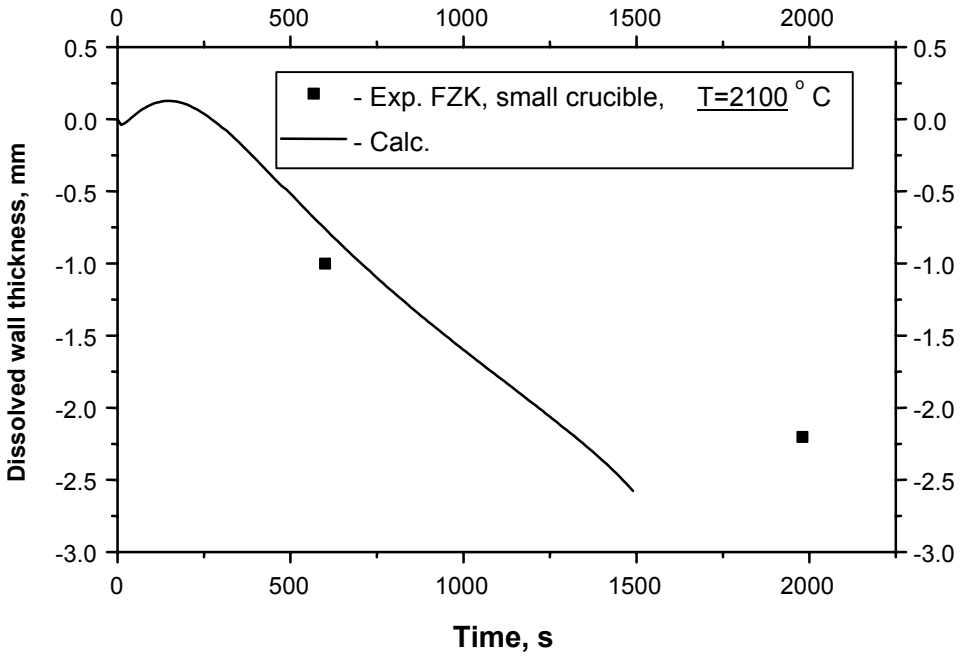

Fig. 63: Simulations of FZK small crucible tests at 2100°C

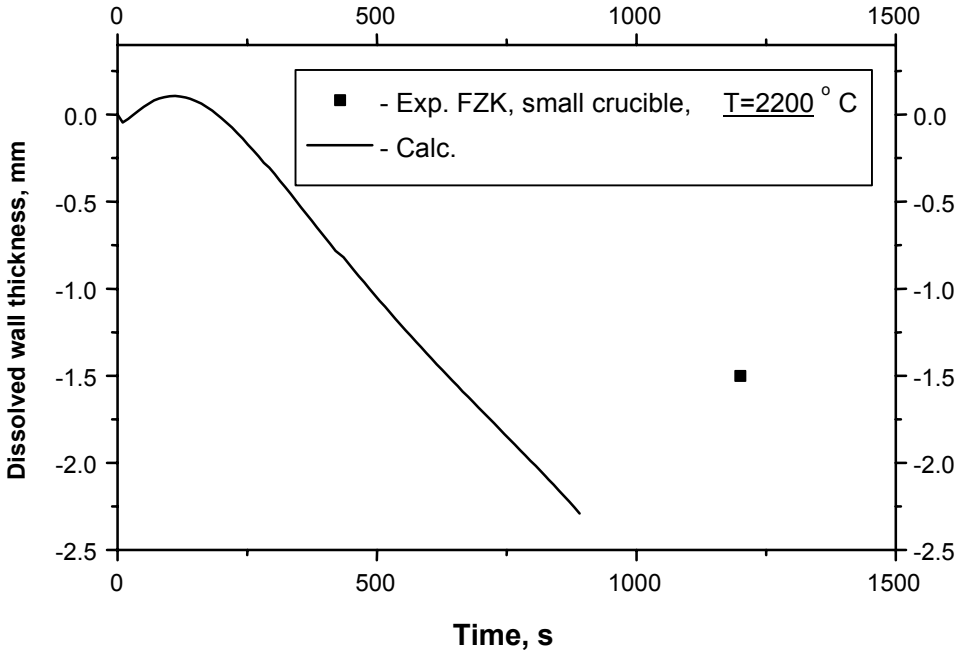

Fig. 64: Simulations of FZK small crucible tests at 2200°C

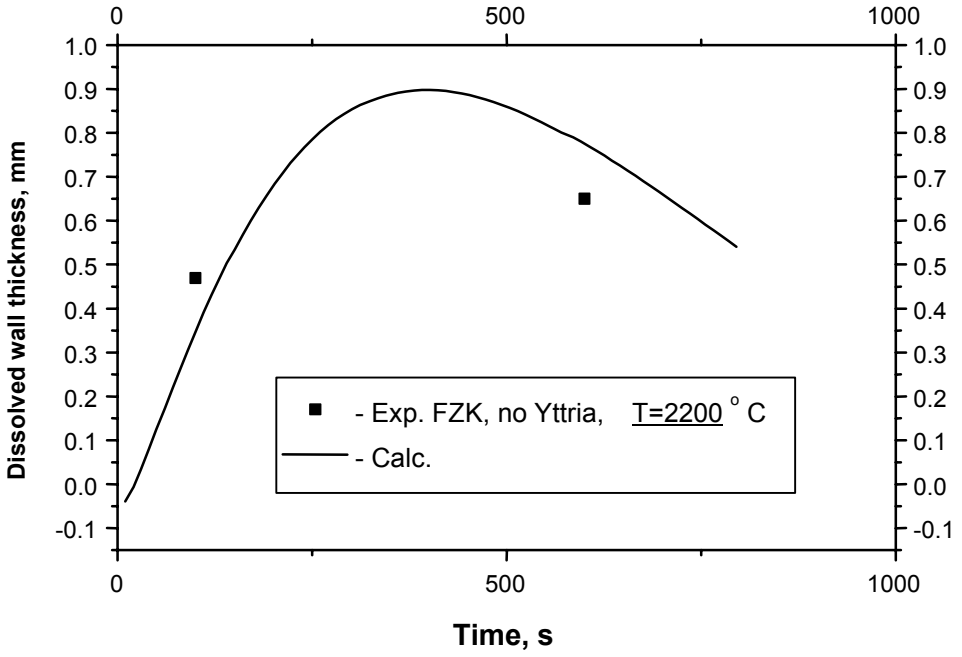

Fig. 65: Simulations of FZK large crucible tests (without bottom isolation) at 2200°C

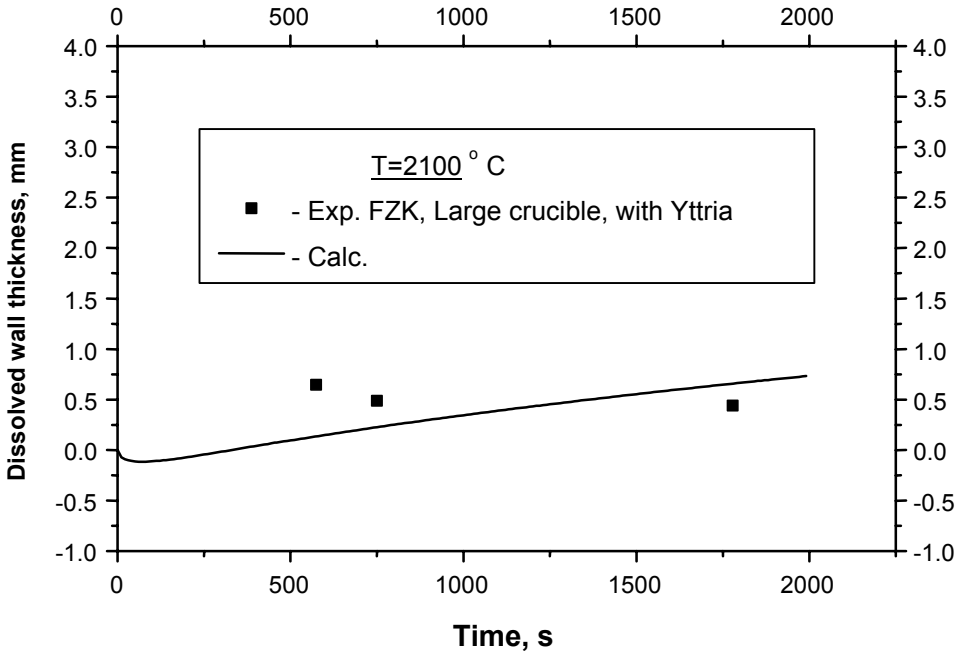

Fig. 66: Simulations of FZK large crucible tests with bottom isolation by yttria disc at 2100°C

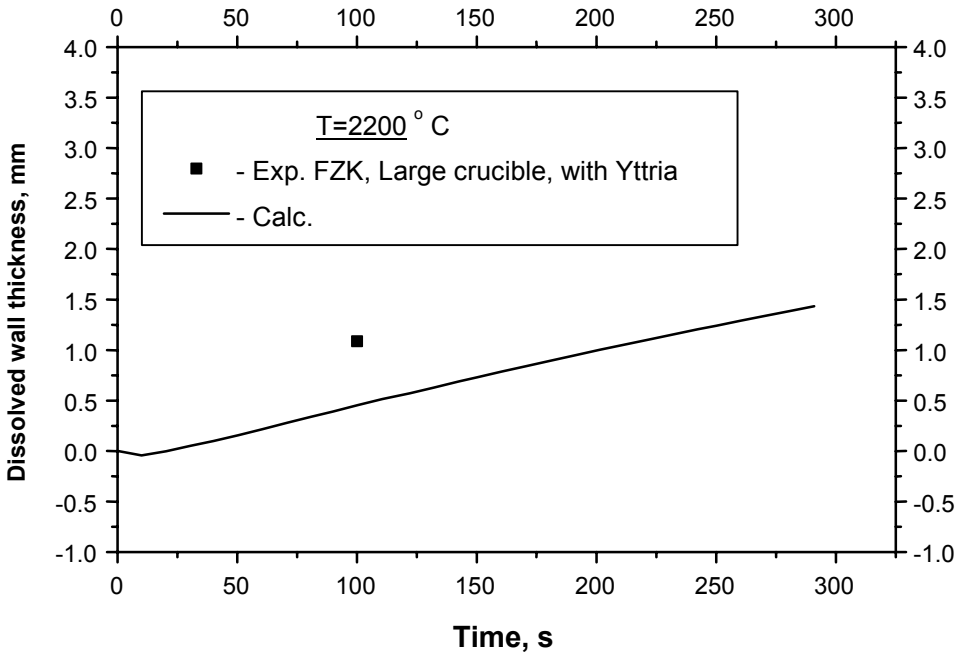

Fig. 67: Simulations of FZK large crucible tests with bottom isolation by yttria disc at 2200°C

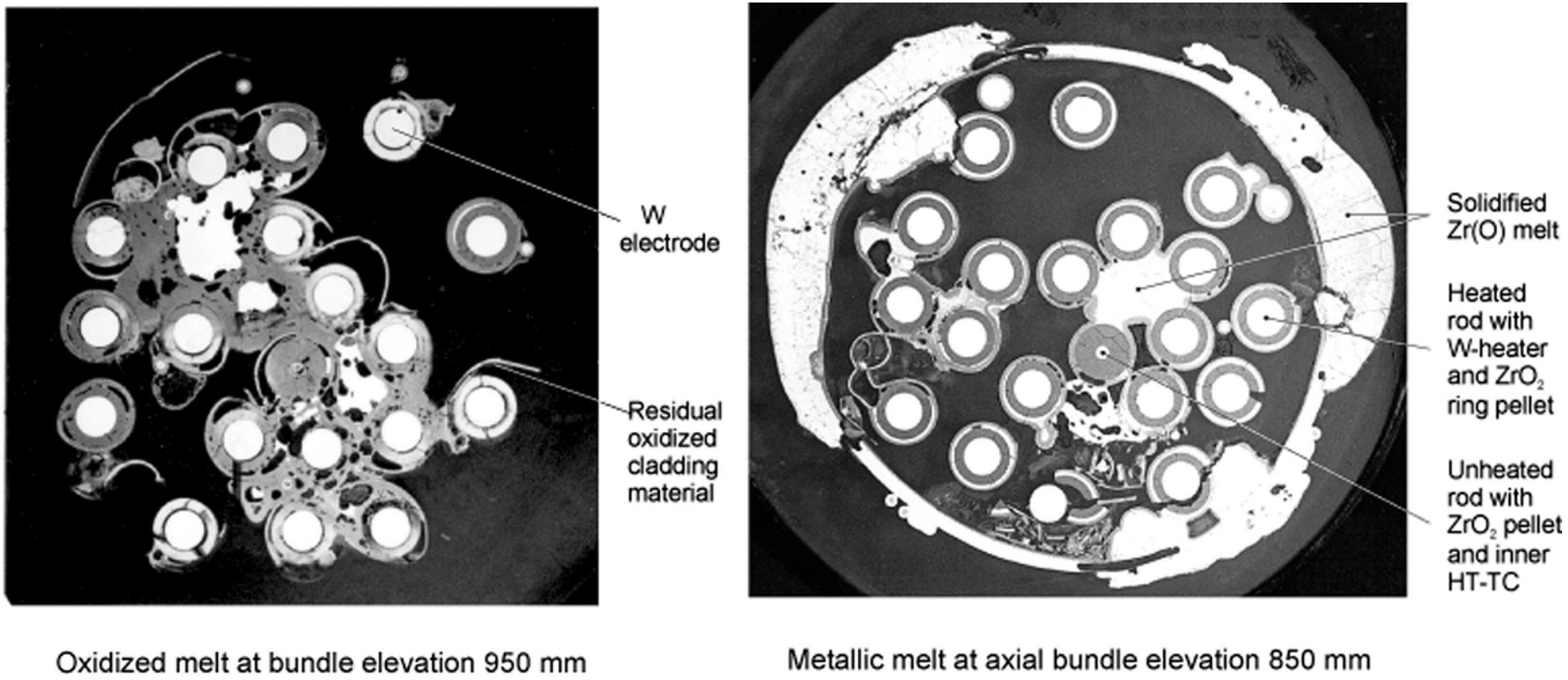

Oxidized melt at bundle elevation 950 mm

Metallic melt at axial bundle elevation 850 mm

Fig. 68: QUENCH-02. Relocated melt at two axial bundle elevations

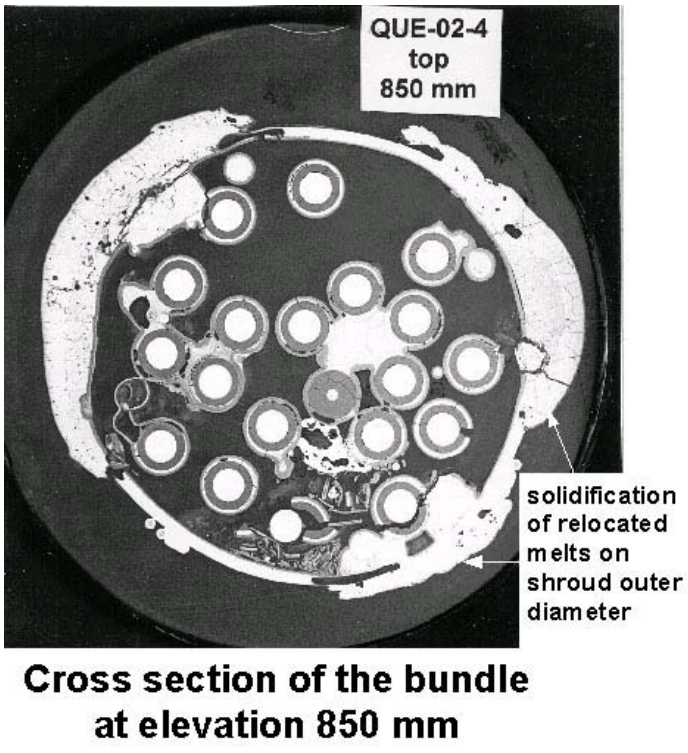

Cross section of the bundle at elevation 850 mm

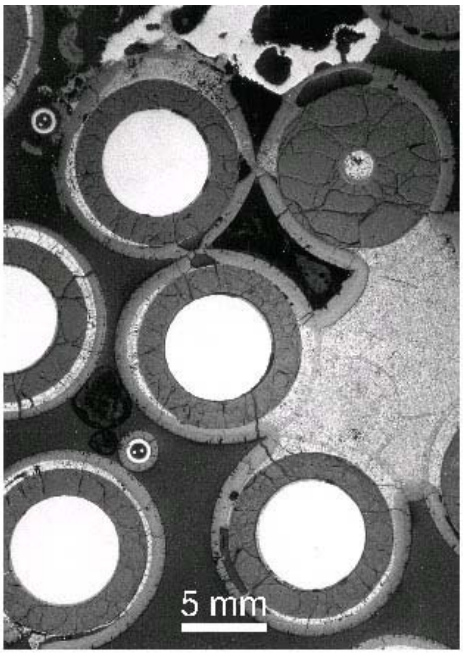

Interaction of relocated melt with ZrO_2 shells

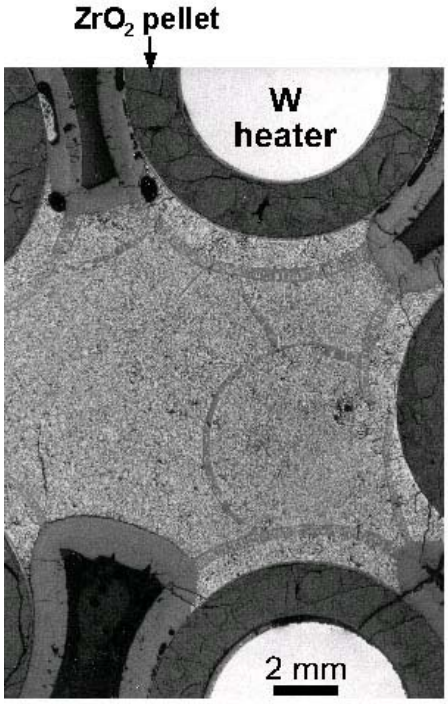

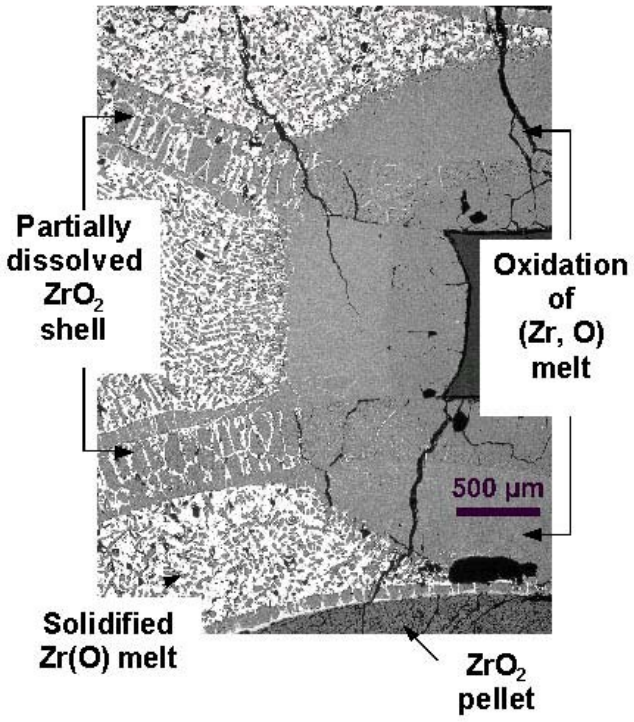

Fig. 69: QUENCH-02. Dissolution of oxide scales by relocated Zr(O) melt

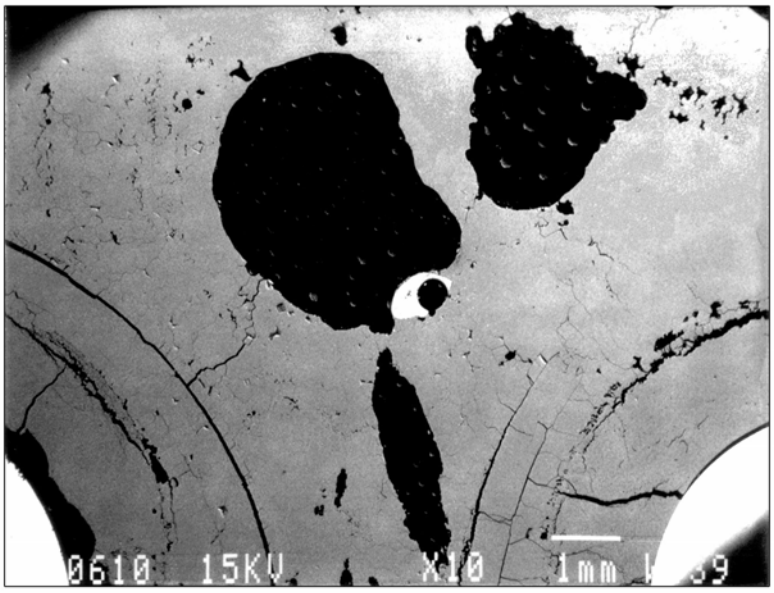

Cross section 950 mm

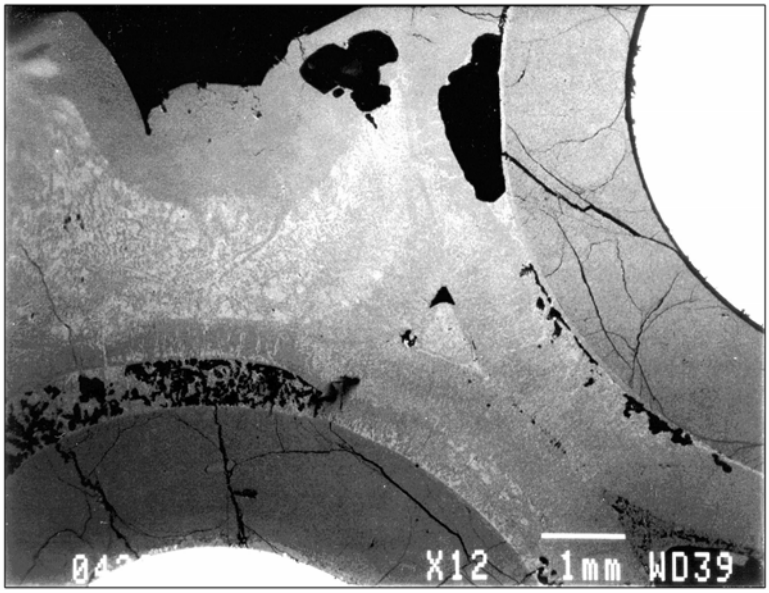

Cross section 850 mm

Fig. 70: Molten pools in bundle QUENCH-02

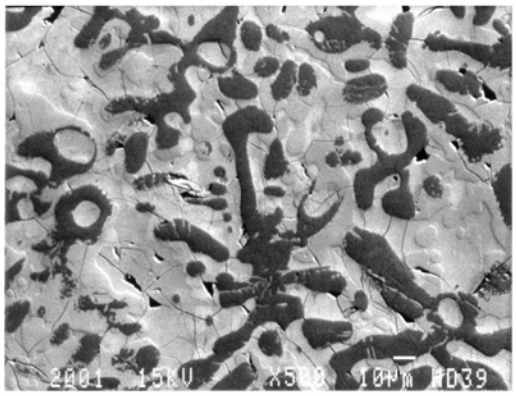

Integral EDX: **Zr:O=49:51 (at%)**
Image analysis: **Zr:O=54:46 (at%)**

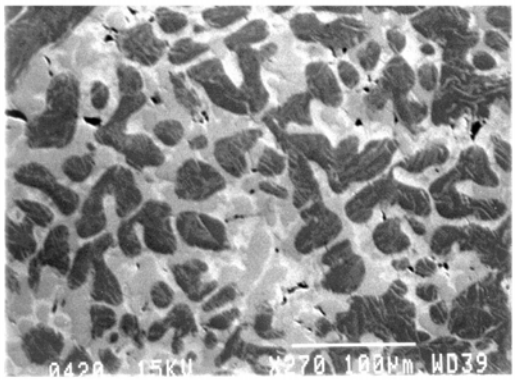

Integral EDX: **Zr:O=45:55 (at%)**
Image analysis: **Zr:O=48:52 (at%)**

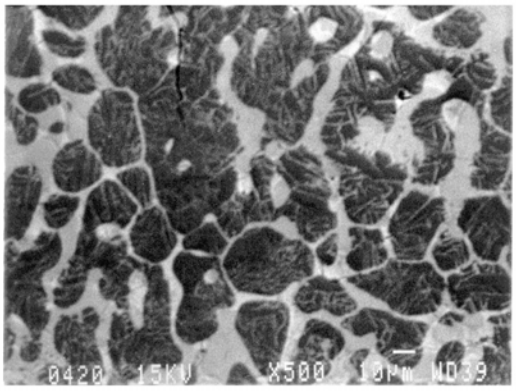

Integral EDX: **Zr:O=42:58 (at%)**
Image analysis: **Zr:O=43:57 (at%)**

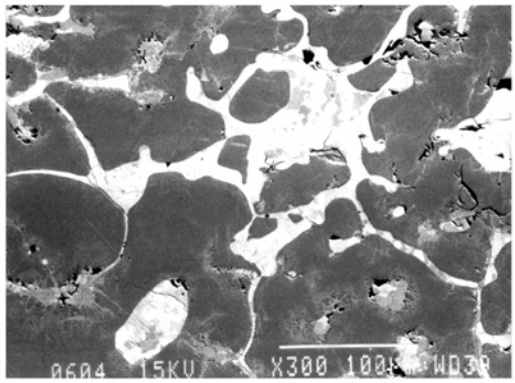

Integral EDX: **Zr:O=36.5:63.5 (at%)**
Image analysis: **Zr:O=40:60 (at%)**

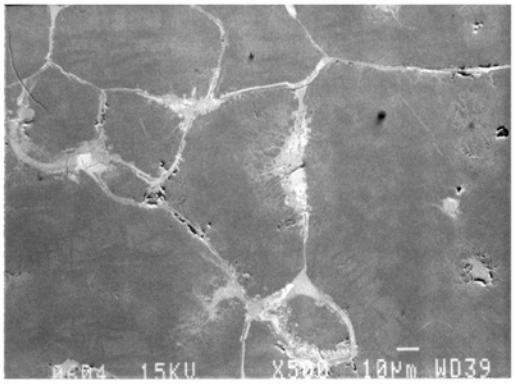

Integral EDX: **Zr:O=35:65 (at%)**
Image analysis: **Zr:O=36:64 (at%)**

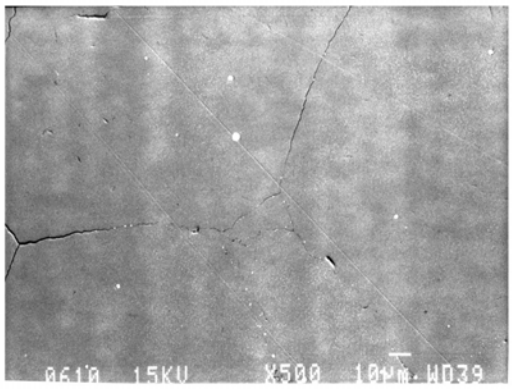

Integral EDX: **Zr:O=32:68 (at%)**

Fig. 71: EDX and image analyses of solidified melts at different positions of the QUENCH-O2 bundle cross-sections

Part II. ZrO_2 Shell Failure: Tests and Analysis

1. Introduction

When the melting temperature of the unoxidized Zircaloy is reached (2033 K), the failure of the cladding and the mechanisms of chemical interaction, which take place between the metallic melts and the solid UO_2 pellet and ZrO_2 layer on the external cladding surface, have great relevance to core degradation, giving the possibility for low-temperature (U,Zr,O) mixture relocation and giving rise to an increased release of fission products from the liquefied fuel. If a sufficiently thick oxide layer has formed on the outside surface of the cladding tube, the relocation of any molten Zircaloy will be prevented, or limited inside the gap between cladding and fuel pellets, because of a "crucible" effect due to the high melting point of ZrO_2. The oxide layer will remain in place until its melting point is reached, or until it is dissolved by molten Zircaloy, or until it fails mechanically. Depending on the mode of failure and the melting capability of the solid rod by the liquid mixture, the molten material may relocate as rivulets (heat transfer process).

Analyses of the results of the integral tests on the severe accident behaviour of the fuel bundles under the loss of coolant conditions show that the oxide scale failure strongly influences the accident progression. The cladding failure usually occurs after the burst or local melting of the cladding which lead to the internal overpressure disappearance and the onset of the inner cladding surface oxidation. Under the further temperature escalation the metal phases of Zircaloy melt and the oxide scale prevents the molten Zircaloy from relocation. After the oxide scale failure an intensive oxidation of the melt occurs at a high temperature region of a bundle and a blockage forms at lower and more cold parts of the bundle. These can lead to the further sharp temperature increase due to reduction of the bypass flow and heat release due to the melt oxidation.
The oxide scale failure at high temperatures occurs as a wall breach formation and is termed “flowering” due to increase of a distance between breach edges which allows melt relocation.

Knowledge of cladding failure mechanisms above the Zircaloy melting temperature is currently lacking. Only simple parametric models using user-defined parameters are currently available in the code systems. In the assumption currently made, the ZrO_2 layer fails when a certain temperature limit is exceeded (typically 2300 — 2500 K) and the ZrO_2 layer is less than a limiting thickness (the oxide shell is assumed not to break if typically 60 % of the original wall has been completely oxidized); the uncertainty in the break temperature is more significant. The large scatter in the cladding failure parameters used in the code applications is evidence for the lack of understanding in this area, and for the need to develop physically-based models. The development of such models requires an experimental data base.

The objective of the present investigation is to provide such a data base, to study and clarify the possible reasons and criteria of the oxide scale failure (“flowering”) at high temperatures, and to develop a model for its prediction.

2. Experimental data analysis

In the present investigation the available experimental data on the oxide scale failure at high temperatures obtained at the FZKA (Germany) tests [1], are analysed.

2.1 Experimental procedure

Different experimental approaches have been applied to obtain the required data, however, only the experiments in the small-scale QUENCH test apparatus have been successful. The design of the test section for ZrO_2 shell-failure-criteria experiments and specimen are presented in Fig. 1. The tube specimen of a length of 50 mm, filled with ZrO_2 pellets, is suspended inside a quartz tube which is surrounded by an induction heating coil. The specimens were inductively heated up to 1400 °C in an argon-oxygen mixture and were held at this temperature from 2 to 9 minutes. Then the specimens were further inductively heated up with heating rate from 2 to 10 K/s (Fig. 2) up to the onset of cladding failure and release of the molten material. After the detection of the molten material on the outer specimen surface the power supply was shut down and the specimens cooled down.The cladding surface temperature is measured by a pyrometer in the center of the specimen in all tests, in some tests a centerline thermocouple was used additionally.

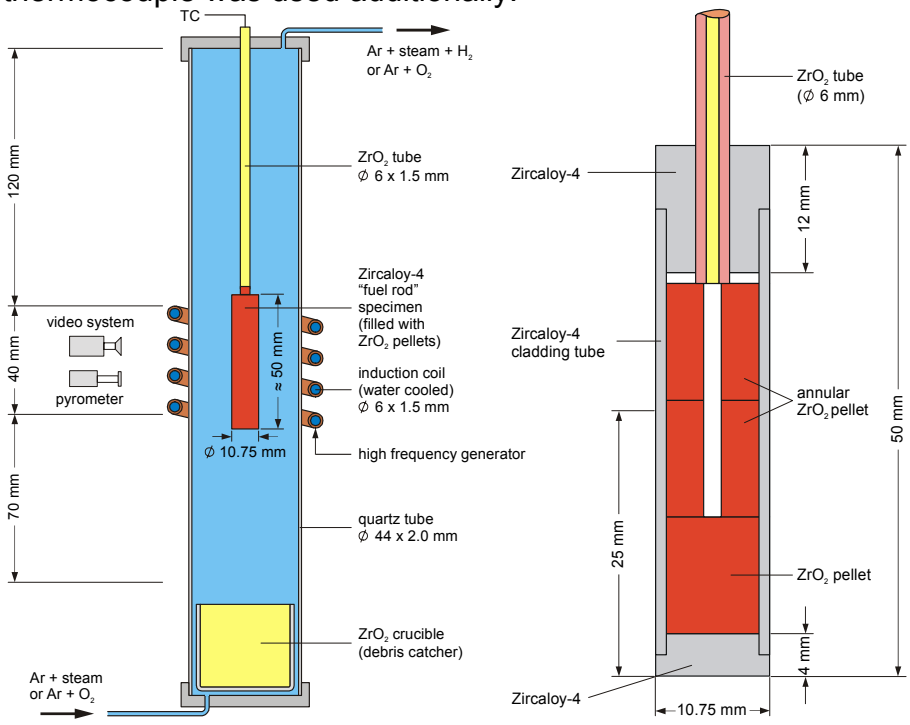

Fig. 1: Test section design and specimen for ZrO_2 shell-failure-criteria experiments.

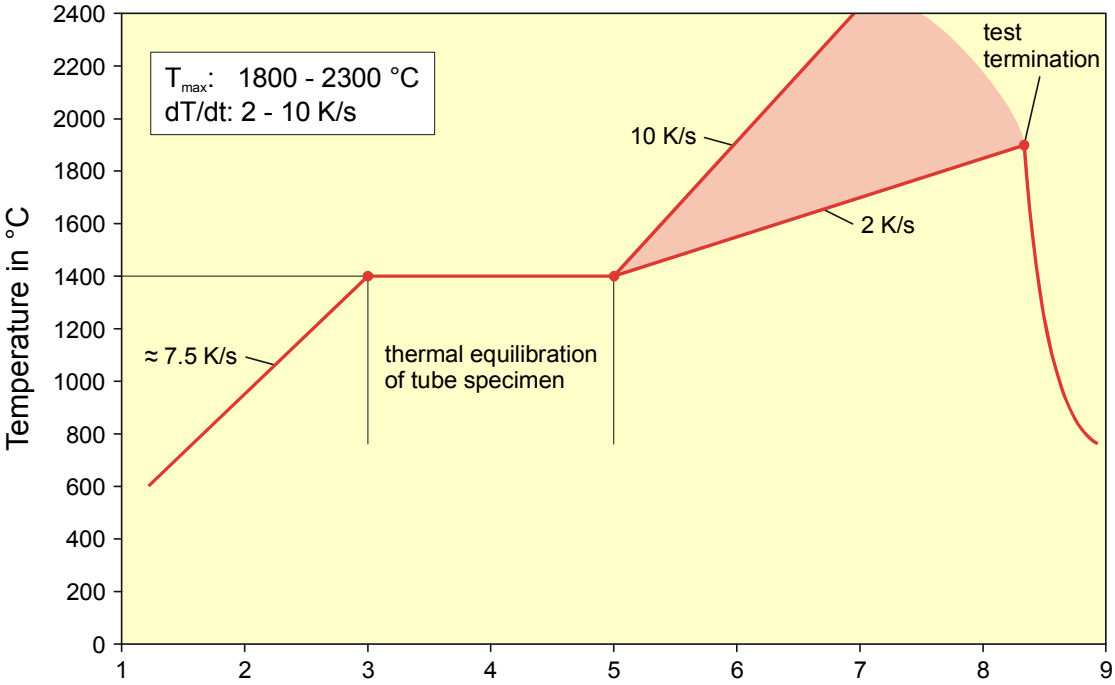

Fig. 2: Test conduct of the ZrO_2 shell-failure-criteria experiments.

2.2 Experimental observations and their interpretation

The essential results of the FZKA experiments with a time of pre-oxidation of 2 min at 1400 °C and different heating rates are presented in Table 1.

Test ID	t_p, min	ΔT, K/s	Temperature at onset of failure		Oxide layer thickness					
			Pyrometer	TC W/Re	h	ΔZrO_2	h	ΔZrO_2	h	ΔZrO_2
19SK	2	4	1950	—	**16.5**	**345**	25	300	35	180
20SK	2	8	2010	—	13	175	**26**	**110**	35	85
21SK	2	8	1980	—	13	180	**24**	**125**	**35**	**90**
22SK	2	2	2010	—	**9.5**	**455**	25	compl.	35	530
23SK	2	3	1800	—	13	270	**25**	**390**	35	230
24SK	2	3	2170	—	**10**	**435**	25	compl.	35	compl.
25SK	2	6	1860	—	13	215	**25**	**200**	35	120
26SK	2	2	1930	—	—					
27SK	2	5	2000	—	13	435	**25**	**380**	**30**	**425**
28SK	2	10	1960	—	12.5	150	**24**	**140**	32	110
29SK	2	5	2020	—	—	—	—	—	—	—
30SK	2	4	2130	2000	17	625	25	510	36	370
31SK	2	6	1930	1859	—					

32SK	2	8	2030	1820	12	210	**25**	**170**	35	120
33SK	2	5	2100	1990	10	345	**24**	**340**	34	320
34SK	2	6	1975	1815	14	250	**26**	**210**	35	140
35SK	2	4	2130	1870	12	580	25	510	**31.5**	**395**
36SK	2	4	2100	2185	13	560	25	550	**31**	**425**
37SK	2	8	1970	1855	—					
38SK	2	6	1880	2010	13	230	25	230	**33**	**175**
39SK	2	4	2130	2180	14	570	26	530	**31.5**	**425**
40SK	2	2	2020	>2300	14	compl.	25	compl.	36	compl.

Table 1: ZrO_2 shell failure-criteria experiments with 50 mm long Zry-4 tube specimens filled with ZrO_2 pellets. The failure positions are marked bold; t_p – time of pre-oxidation at 1400 °C; ΔT – heat-up rate starting from 1400 °C; ΔZrO_2 – oxide layer thickness (µm) at the given elevation h (mm); H – failure position (h and H measured from the bottom of the rod).

The results of the experiments show a clear correlation between the heat-up rate and the oxide shell failure temperature. No failure occurs if a heat-up rate is less than 3 K/s — the cladding completely oxidizes before reaching the melting point of the Zircaloy (Fig. 3). The cladding failure temperature continuously decreases with increasing heat-up rate and after reaching a certain limit (app. 6 K/s) remains constant (Fig. 4).

After the tests the tube specimen was cut at the location where cladding failure occurred and metallographically prepared to determine the thickness of the remaining Zircaloy layer (see examples in Figures 5 - 8). The oxide layer thickness was measured in the different azimuth and, in a few cases axial locations. The oxide layer thickness at onset of failure decrease with increasing heat-up rate starting from 450 µm at 4 K/s and reaching 100 µm at 8 K/s and more.

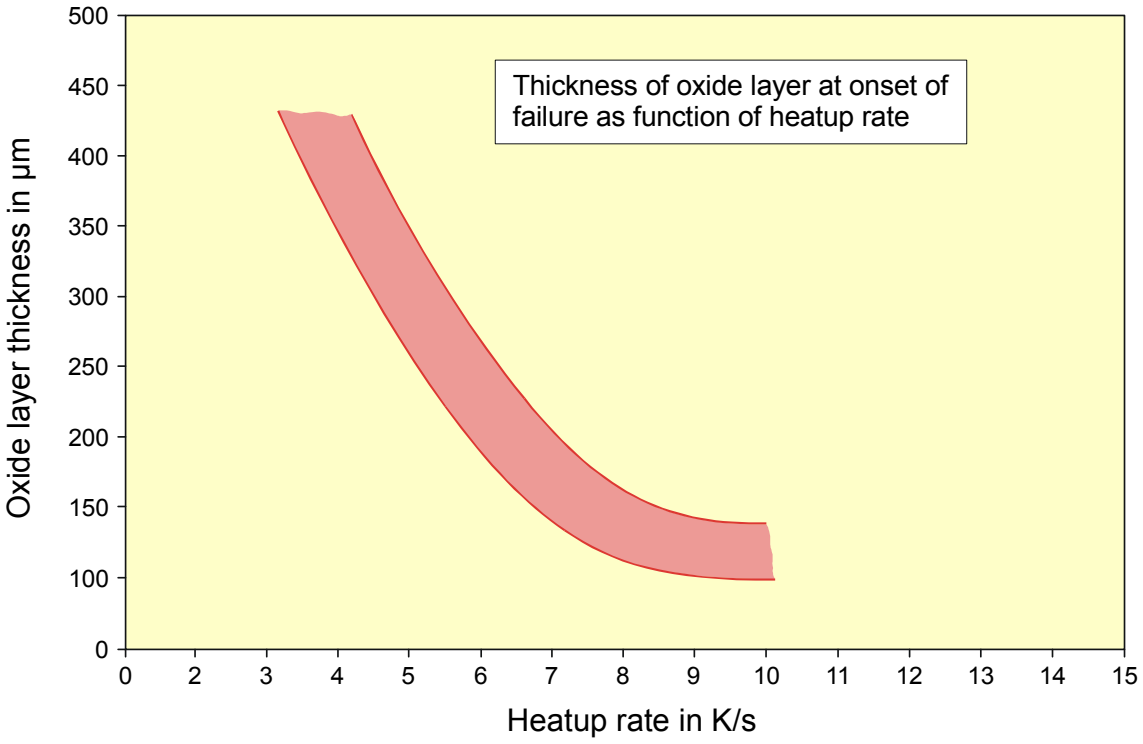

Fig. 3: Dependence of the oxide layer thickness from the heatup rate in ZrO_2 shell-failure-criteria experiments.

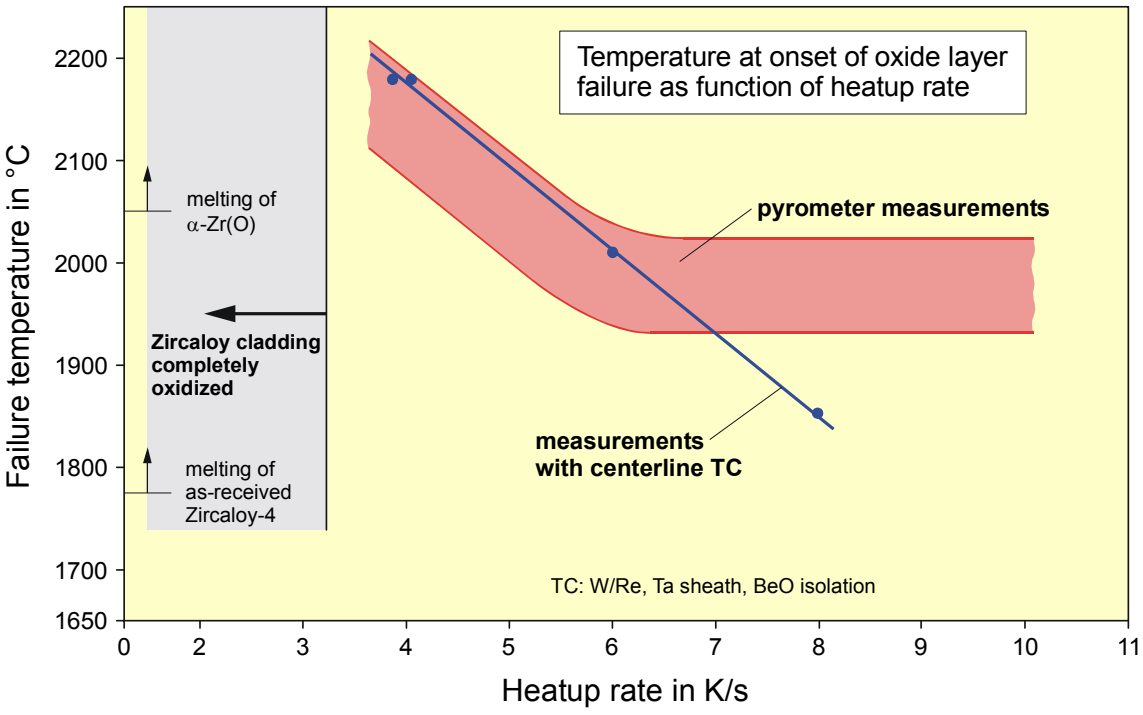

Fig. 4: Dependence of the failure temperature in ZrO_2 shell-failure-criteria experiments.

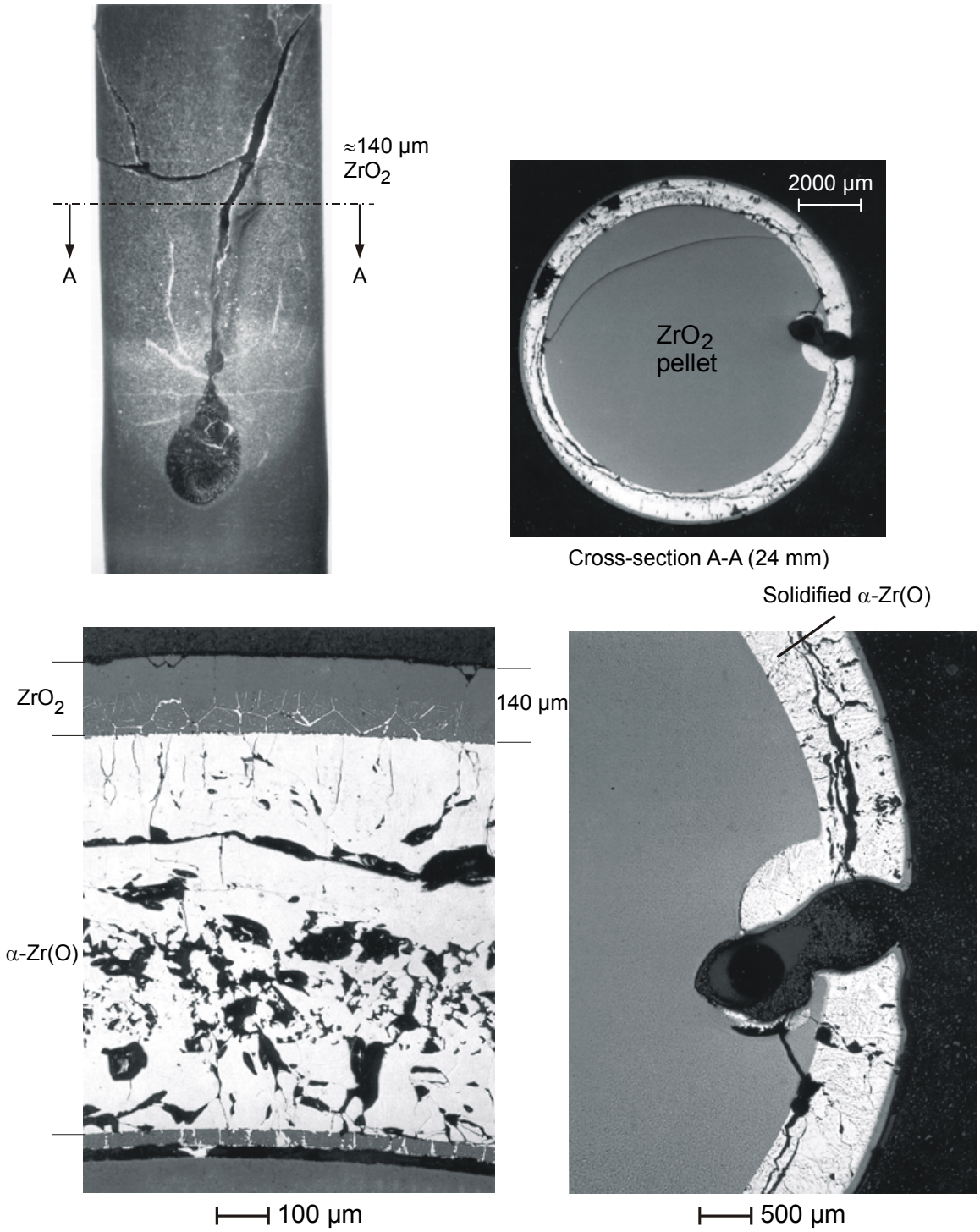

Fig. 5: Test 28SK, Two minutes pre-oxidation at 1400 °C, 10 °K/s heat-up rate, melt-through at 1960 °C (pyrometer). Two upper pictures: outer surface and cross-section of the specimen. Two lower pictures: structure of the layers and breach formed in the oxide layer.

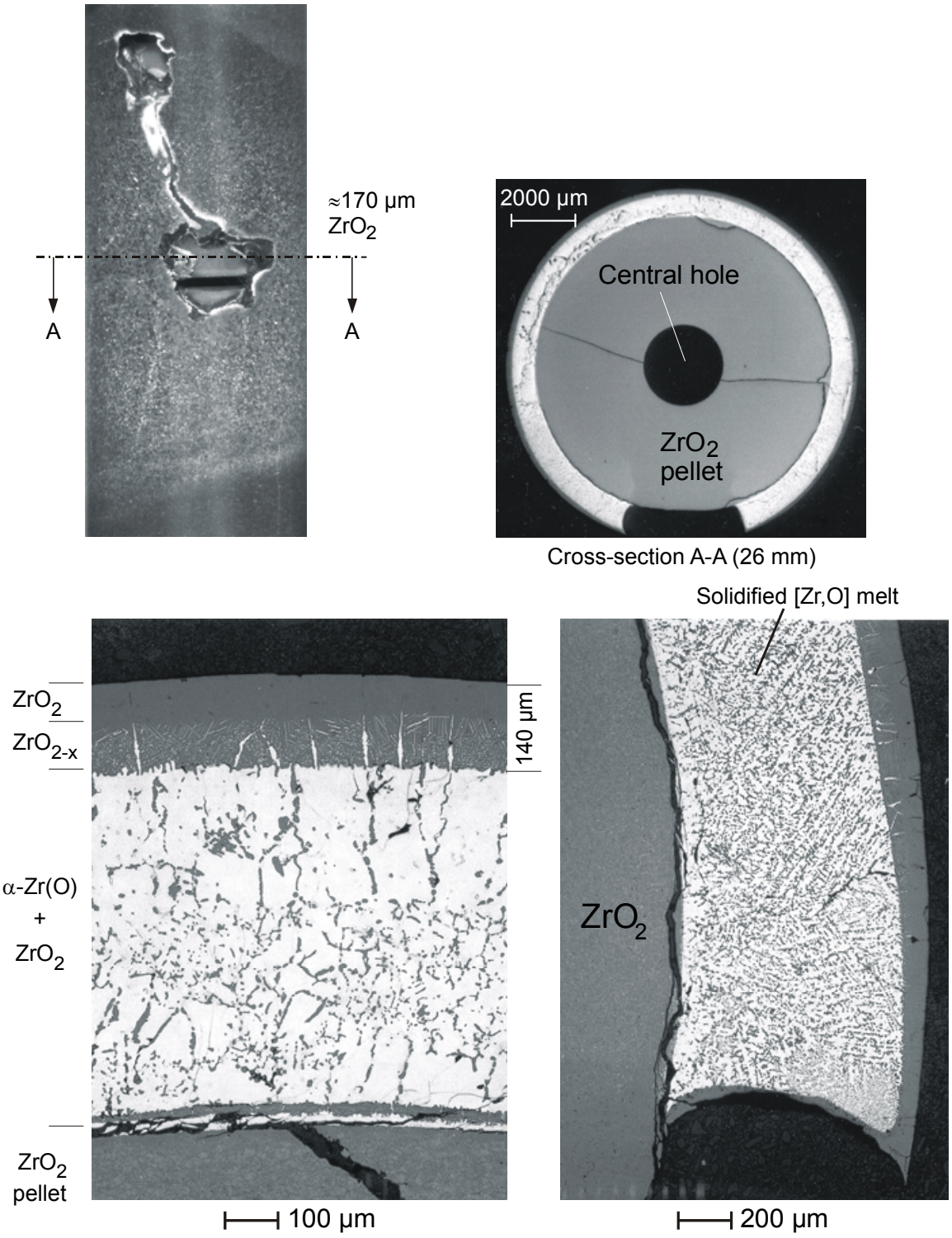

Fig. 6: Test 32SK, Two minutes pre-oxidation at 1400 °C, 8 °K/s heat-up rate, melt-through at 2030 °C (pyrometer). Two upper pictures: outer surface and cross-section of the specimen. Two lower pictures: structure of the layers and breach formed in the oxide layer.

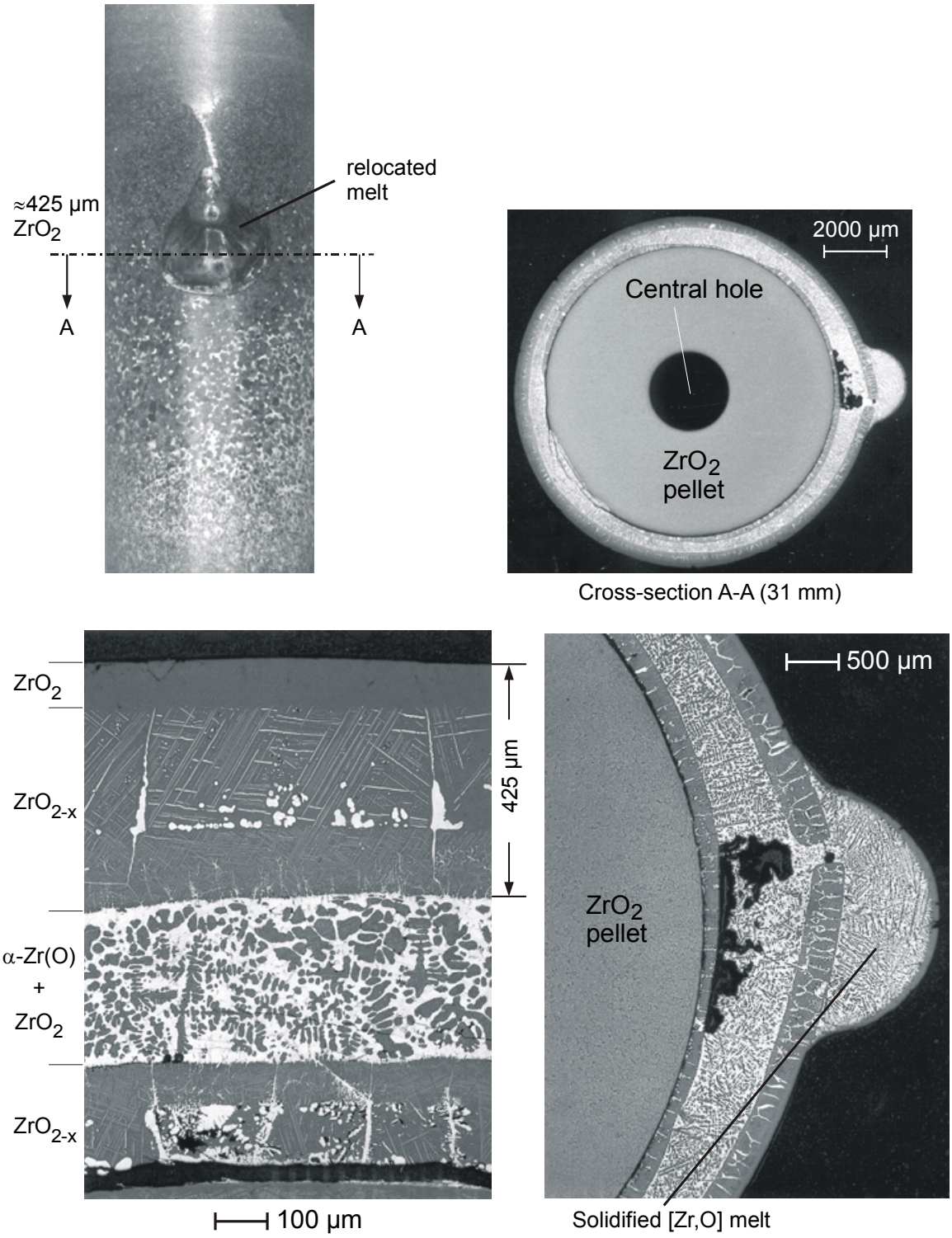

Fig. 7: Test 36SK, Two minutes pre-oxidation at 1400 °C, 4 °K/s heat-up rate, melt-through at 2100 °C (pyrometer)/2185 °C (centerline TC). Two upper pictures: outer surface and cross-section of the specimen. Two lower pictures: structure of the layers and breach formed in the oxide layer.

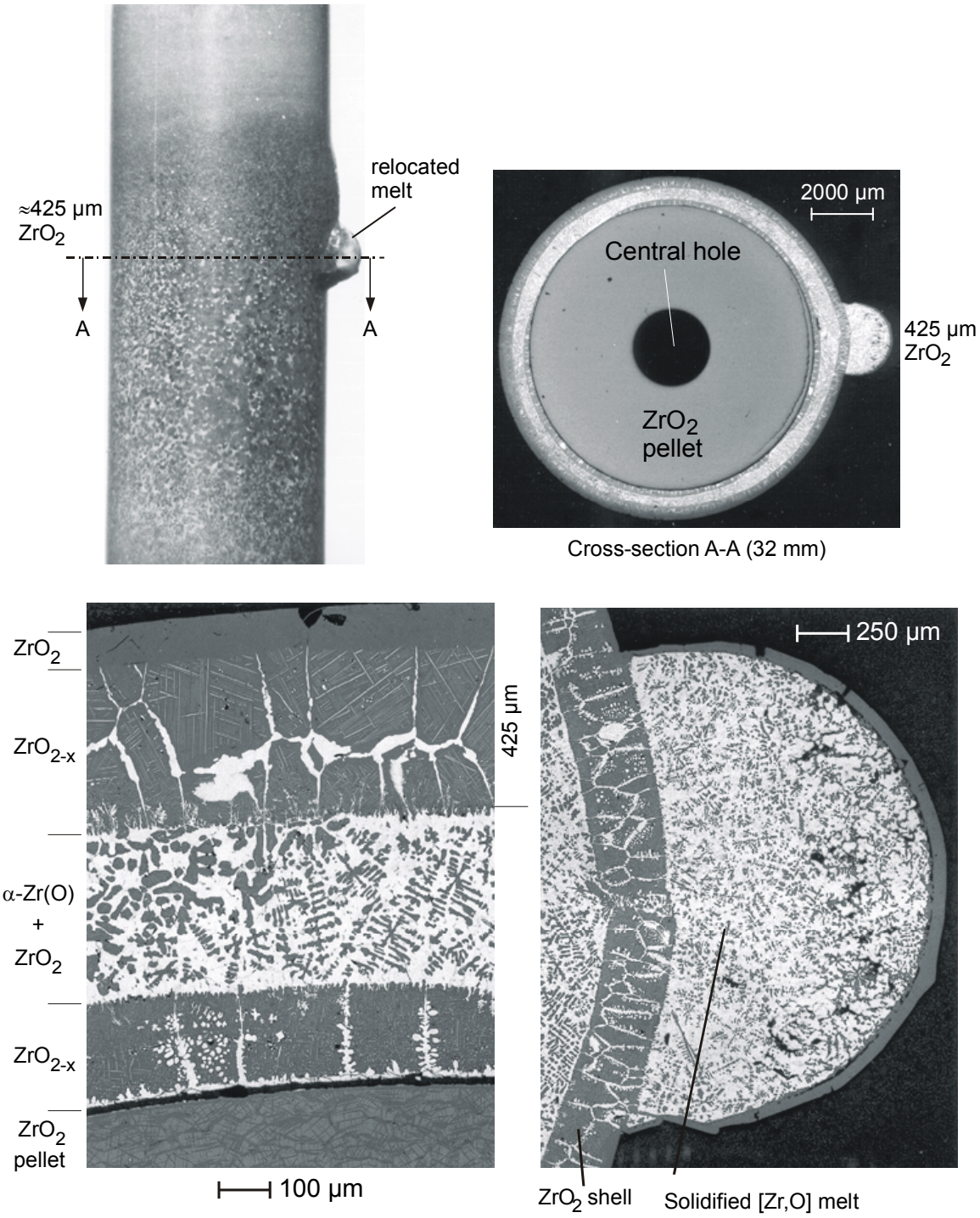

Fig. 8: Test 39SK, Two minutes pre-oxidation at 1400 °C, 4 °K/s heat-up rate, melt-through at 2130 °C (pyrometer)/2180 °C (centerline TC). Two upper pictures: outer surface and cross-section of the specimen. Two lower pictures: structure of the layers and breach formed in the oxide layer.

For the analysis presented below tests with different time of pre-oxidation were selected (Table 2). The results are presented as a function of the pre-oxidation time and heating rate. For each temperature regime the following data are available:

- "Flowering", or failure temperature measured by a pyrometer.
- Thickness of the external oxide scale.
- Thickness of solidified melt [α-Zr(O) + ZrO_2] and inner oxide scale at the location far from the breach in the azimuth direction. These values are estimated from the photographs of the tube specimen cross-sections.

Test ID	Exposure	Rate	T flow	Outer oxide	Mixture	Inner oxide
	Min	K/s	C°	μm	μm	μm
36SK	2	4	2100 (2185)*	425 450	320	190
39SK	2	4	2130 (2180)*	425	330	190
14SK	5	4	1970 (2070)*	510	1046	154
11SK	6	4	1800	350 310	610	100
12SK	7	4	1670	420 450	400	100
13SK	9	4	1850	330 350	500	50
32SK	2	8	2030	140 170	630	20
15SK	4.5	8	1925	140 210 215	600	0
16SK	6	8	1975	100 320	-	-

Table 2: Results of the "flowering" tests: temperature of oxide scale failure and thickness of the cladding layers. * temperature inside the pellet, measured by the central thermocouple

It should be noted that at the heating rate less than 3 K/s the cladding was completely oxidised before the temperature reached the melting point of Zircaloy metal phases, therefore these heating rates are not included into consideration.

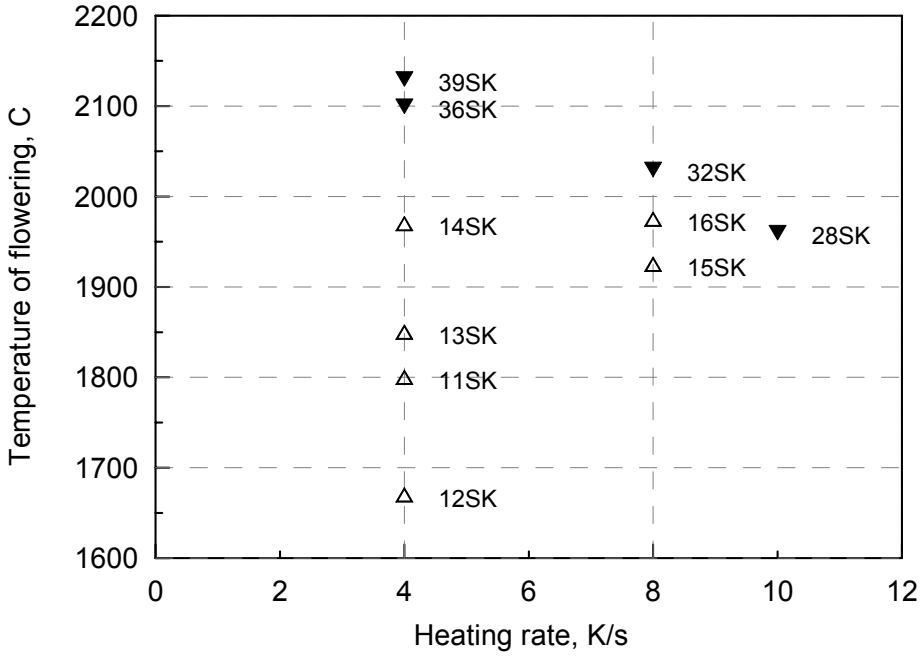

Fig.9: Temperature of oxide failure as a function of heating rate.

In Fig. 9 temperatures of oxide scale failure are plotted as a function of heating rate.

In Figs. 5 - 8 the most typical views of the specimen surfaces and the cross-sections near the molten material appearance are presented for different heating rates.

The following main features of the oxide failure at the given heating rate can be derived from the analysis of the presented experimental results:

- One can see that the pyrometer measured temperature of oxide scale failure varies between 1670 and 2130 °C in the case of heating rate 4 K/s, and between 1925 and 2030 °C in the case of higher heating rates 8 and 10 K/s, Fig. 9. The scatter of the “flowering” temperatures is wider for lower heating rate. One of the reasons of such a scatter of the “flowering” temperature is a low accuracy of the pyrometer measurements.
- The thickness of the outer oxide layer near the location of the molten material appearance is many times greater in the case of low heating rate, Fig. 8 and Fig. 6. In the case of high heating rate the oxide thickness strongly varies in the azimuth and axial directions: the minimum thickness of the oxide scale is observed near the oxide failure location. In the case of low heating rate the oxide thickness variation occurs in the azimuth direction, but this variation is less than for high heating rate.
- A thick inner oxide scale (near the pellets) is observed in all tests with low heating rate, Fig. 8. Oxide thickness varied between 50 and 190 μm. In the case of the high heating rate the inner oxide is absent or very thin (20-30 μm), Fig. 6.

- Cavities in the pellets due to local dissolution by molten Zircaloy are observed only in the test with high temperature rate.
- Views of the formed breaches differ for the various heating rates. In the case of low heating rate the formed breach is covered, as a rule, by the molten material which looks like a drop on the surface, Fig. 8. The cross-section of the formed breach looks like a narrow split in the oxide scale, Fig. 8. In the case of high heating rate the formed breach looks like a spot and in some cases the cladding materials are absent due to relocation, Fig. 6. Breach formation can be accompanied by the local dissolution of the pellets by molten Zircaloy. The cross-section of the tube near the failure location shows that the oxide scale is absent along a segment of the circle in the azimuth direction, Fig. 6.

These experimental observations lead to the following hypotheses on the modes of the oxide scale failure at high temperatures under various heating rates:

- At high heating rates the outer oxide scale which was formed in the pre-oxidation stage, is partially dissolved by molten Zircaloy during heating, and the thinned oxide layer is broken by the hydrostatic pressure of molten Zircaloy. The local vigorous dissolution of the oxide scale can occur near the formed breach.
- At low heating rates the outer oxide scale which was formed in the pre-oxidation stage, continues to grow during heating, and the inner oxide layer appears on the pellet surface. Owing to the volumetric expansion of oxide, the free (gap) volume unoccupied by the melt decreases and finally disappears, leading to the oxide scale failure induced by the incompressible molten Zircaloy pressure.

Behaviour of the oxide scale under loading by molten Zircaloy depends on the oxide scale and metal phase thickness, oxygen concentration in molten Zircaloy and oxygen flux at the cladding surface.

At high heating rates the thinner oxide scale grows during transient up to melting of the metal Zircaloy phases. The volume of the molten materials is higher and the oxygen concentration is lower than in the case of low heating, as can be seen from Figs. 6 and 8 (note that a higher amount of grey ceramic phase particles in the post-test view photographs corresponds to a higher oxygen concentration in the melt). This leads to the intensive convective stirring of the melt and dissolution (erosion) of the outer oxide layer and, possibly, of the pellets fabricated from the stabilised zirconia.

At low heating rates the thick outer oxide scale, smaller volume of the molten materials and higher oxygen content inhibit the dissolution rate and lead to the oxide scale growth. The outer oxide grows due to the outer oxygen flux and the inner oxide grows due to oxygen flux from the pellets.

The competitive processes of the oxide scale dissolution (erosion) and oxidation (corrosion) were described by the model LIQF [2] developed on the base of the zirconia crucible dissolution tests [3].

The model CROX of the SVECHA/QUENCH code [4] for the oxide scale deformation and failure at high temperatures was further developed to examine the deformation behaviour of the oxidised cladding under conditions of the new tests [1] and to verify the proposed hypotheses on the reasons of the oxide scale failure.

3. Oxide scale stress state under the "flowering" conditions

An approach for the stress state evaluation of the oxidised cladding in the stages before Zircaloy melting is described in [4]. In the present section the specific features of the oxide scale deformation under "flowering" conditions are considered.

In the latest stages of an accident when the cladding burst or local melting occurred and external and internal pressures equalised, the factors of the stress generation in the oxide scale are the following:

- temperature gradient along the oxide scale thickness,
- hydrostatic pressure induced by molten Zircaloy column,
- volumetric expansion under oxidation which leads to disappearance of the gap volume and, then, to generation of the high level pressure in the incompressible Zircaloy melt.

Basing on the assumption that oxide deforms elastically up to its melting, the final stress state is considered as a superposition of the stresses generated by all these factors. For this reason, each of these factors will be considered in more details.

3.1 Stress in the oxide scale due to temperature gradient in the radial direction

From simulations of the radial temperature distribution by the heat-exchange module of the SVECHA/QUENCH code [4], it was found that radial temperature gradients in the metal layers are negligible and the radial temperature distribution in the outer oxide layer may be significant and approximated by a linear function, Fig. 10. It is assumed that the oxide scale can be considered as a thin wall cylindrical shell. Hence, due to a small ratio of oxide thickness to the average oxide radius, the influence of the cylindrical geometry becomes negligible and the average oxide temperature T^{ox} can be determined as a half of the sum of the external T^{ox}_{ext} and internal T^{ox}_{int} surface temperatures:

$$T^{ox} = \frac{T^{ox}_{ext} + T^{ox}_{\mathrm{int}}}{2}, \tag{1}$$

The temperature drop in the oxide scale can be calculated as:

$$\Delta T^{ox} = T^{ox}_{\mathrm{int}} - T^{ox}_{ext}, \tag{2}$$

Under an assumption of a thin oxide layer the following expression of the linear elasticity theory for the surface circumferential, axial and radial stresses caused by the radial temperature drop can be applied [5]:

$$\sigma^{ox}_{\theta}(r^{ox}_{e}) = \sigma^{ox}_{z}(r^{ox}_{e}) = \frac{E^{ox}}{2(1-\nu^{ox})} \cdot \alpha^{ox} \cdot \Delta T^{ox},$$

$$\sigma^{ox}_{\theta}(r^{ox}_{i}) = \sigma^{ox}_{z}(r^{ox}_{i}) = -\frac{E^{ox}}{2(1-\nu^{ox})} \cdot \alpha^{ox} \cdot \Delta T^{ox}, \tag{3}$$

$$\sigma_r^{ox}(r_i^{ox}) = \sigma_r^{ox}(r_e^{ox}) = 0\,,$$

where $\sigma_r^{ox}, \sigma_\theta^{ox}, \sigma_z^{ox}$ are the radial, circumferential and axial stresses in the cylindrical coordinate system, respectively; r_i^{ox}, r_e^{ox} are the internal and external oxide scale radii, respectively; E^{ox}, ν^{ox} are the Young's modulus and Poisson's ratio of the oxide at the average temperature T^{ox}, respectively.

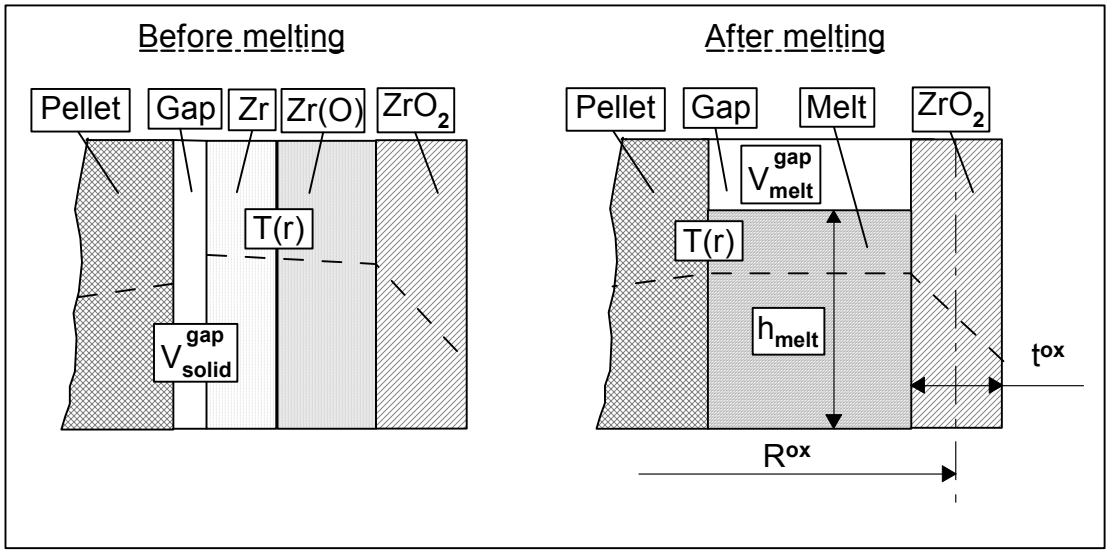

Fig.10: Structure of layers of the oxidized cladding before and after melting of Zircaloy.

The average stress (across the oxide thickness) is equal to zero, hence, the oxide cracks if the tensile circumferential or axial stress on the surface exceeds the flexural strength. It is assumed that cracks propagate through the oxide scale. If the metal layers did not melt before the oxide cracking, then as a rule the cracks propagation is arrested by the ductile metal layer. In the case of molten Zircaloy the through wall breach can form.

3.2 Stress in the oxide scale due to pressure of molten Zircaloy

The stress in the oxide scale after melting of Zircaloy depends on the gap volume between the pellets and the cladding. If the gap volume is greater than the volume increment of the metal layers during melting (the volume of Zircaloy increases due to melting), as shown in Fig. 10, then an additional stress is generated by the hydrostatic pressure of molten Zircaloy column:

$$p = \rho \cdot g \cdot h_{melt}\,, \tag{4}$$

where *p* is the pressure of molten Zircaloy on the bottom of the melt, *g* is the gravity acceleration and h_{melt} is the height of the molten Zircaloy layer after the relocation into the gap between pellets and the oxide scale.

This pressure leads to the circumferential stress in the oxide scale, the axial and radial stresses are negligible. In the case of a thin wall cylinder this average tensile circumferential stress can be found in the following way:

$$\sigma_\theta^{ox} = \frac{R^{ox}}{t^{ox}} \cdot p\,, \tag{5}$$

where σ_θ^{ox} is the circumferential stress in the oxide scale, R^{ox} is the average oxide scale radius and t^{ox} is the oxide scale thickness, Fig. 10. If after Zircaloy melting the oxide scale is intensively dissolved, this stress can break the thin oxide scale. The average axial stress is equal to zero.

If the volume increment of the metal layers during melting is greater than the gap volume then the tensile circumferential stress in the oxide scale increases very steeply (the axial stress is much less) owing to the incompressibility of molten Zircaloy. Hence, the oxide scale may crack practically at the moment of Zircaloy melting.

If the volume increment of the metal layers during melting is less than the gap volume, but a further melt oxidation (corrosion) occurs, a similar reason of the oxide scale failure may take place, Fig. 10. In this case the gap volume further reduces owing to the volumetric expansion under oxidation. When the gap disappears, then the oxide scale cracks as described above.

4. Oxide scale cracking

4.1 Strength limits of zirconia

Zircaloy dioxide mechanical properties are taken from the MATPRO data base [6]. However, only the Young's modulus and tensile strength as a functions of temperature are available in this data base. Tensile strength at the high temperature (> 1800 K) is not available and it is assumed that it equals to 1 MPa up to melting [6].

The lack of reliable data on the compressive strength and flexural strength (i.e. the maximum stress in the outer fiber at the moment of crack or breach formation) significantly complicates the modelling of the oxide scale failure.

Mechanical properties of the stabilised zirconia are studied in more details. Small admixtures of some oxides such as CaO, MgO and Y_2O_3 into the zirconia structure form the solid solution with a stable cubic structure, which has no phase transformation during heating and cooling. Stabilised zirconia is used as engineering ceramics due to its increased hardness and high thermal shock resistivity. The pellets in the described above FZKA "flowering" tests were fabricated from the stabilised zirconia.

Despite the stabilised zirconia differs from the pure oxide, one can try to evaluate some necessary mechanical properties of the pure oxide material. The strength limits at room temperature of zirconia stabilised by magnesium oxide are presented in [7]. The stabilised zirconia shows a typical tendency for the strength limits in the case of a brittle material, i.e. the compressive strength is many times higher than the tensile one, and the flexural strength is slightly higher than the tensile one. It is reasonable to expect that the strength limits of the oxide material conserve the same tendency at any temperature. Hence, the compressive $[\sigma]_c$ and flexural $[\sigma]_f$ strength can be estimated by the following way:

$$[\sigma]_c = 10 \cdot [\sigma]_t$$
$$[\sigma]_f = 1.5 \cdot [\sigma]_t , \tag{6}$$

where $[\sigma]_t$ is the tensile strength of the oxide as a function of temperature [6]. Hence, at temperatures above 1800 K the oxide strength limits can be roughly evaluated as follows:

$$[\sigma]_t = 1 \quad \text{MPa},$$
$$[\sigma]_f = 1.5 \quad \text{MPa}, \tag{7}$$
$$[\sigma]_c = 10 \quad \text{MPa}.$$

More accurate evaluation will be gained below (in section 5.1) by fitting of the model calculations to the test observations.

4.2 Criteria of the oxide scale failure under "flowering" conditions

It is assumed that the oxide scale cracks if the following conditions are satisfied:

- The superposition of the average (through the oxide scale thickness) stresses exceeds the limit value.
- The maximum axial or circumferential stress on the oxide scale surfaces exceeds the flexural strength.

In the first case, an approach proposed by O. Mohr [8] may be used. According to this approach, the fracture occurs along the plane where the maximum shearing stresses act. The fracture is caused by normal and shearing stresses acting in these planes. For the multiaxial stress state the fracture criterion for the material with different strength under tension and compression is the following:

$$\sigma_{eqv} = [\sigma]_t , \tag{8}$$

where σ_{eqv} is:

$$\sigma_{eqv} = \sigma_1 - \psi\sigma_3 , \tag{9}$$

where σ_1, σ_2, σ_3 are the principal stresses in the given point which satisfy the condition $\sigma_1 \geq \sigma_2 \geq \sigma_3$, and ψ is the tensile to compressive strength ratio.

Taking into consideration that under the "flowering" conditions the average circumferential and axial stresses are tensile and the radial stress is negligible, the condition of the oxide scale failure may be written as:

$$\sigma_\theta^{ox} = [\sigma]_t , \tag{10}$$

where σ_{θ}^{ox} is the average circumferential stresses induced by the molten Zircaloy pressure.

In the case of the oxide scale failure due to the surface stresses, the criterion can be defined in the following way:

$$\sigma_{\theta,surf}^{ox} = [\sigma]_f ,$$

or

$$\sigma_{z,surf}^{ox} = [\sigma]_f , \tag{11}$$

where $\sigma_{\theta,surf}^{ox}, \sigma_{z,surf}^{ox}$ are the surface circumferential and axial stresses, respectively. These stresses are induced by superposition of the stresses due to radial temperature gradient, Eq. (3) and the average stresses due to the pressure of the molten Zircaloy.

4.3 The residual deformation strength of the oxide layer after cracking

At the heating stages before Zircaloy melting the stresses in the oxide scale can satisfy the criteria of the oxide cracking, Eq. (8) or (11). In the last case the surface stresses are the sum of the stresses due to radial temperature gradient, Eq. (3) and the average stresses obtained from the solution of the stress state problem for the multilayer oxidised cladding [4]. The average stresses are the result of the following factors:

- the internal (in the gap between fuel pellets and cladding wall) and the external (in the channel of the coolant) pressures;
- volumetric expansion of the cladding material due to oxidation;
- temperature gradient;
- different thermal expansion of the oxidised cladding materials;
- thermal expansion of fuel pellets in the case of the gap collapse.

If the stresses in the oxide scale satisfy the failure criteria, Eq. (8) or (11) it is assumed that oxide cracks, i.e. microcracks which are arrested by the ductile metal layer and do not penetrate through this layer, emerge and lead to the loss of the oxide deformation strength to zero value. If oxidation continues, then a new uncracked oxide layer appears and influences the stress-state of the cladding. This assumption of the loss of the deformation strength of the cracked oxide to zero level works well at the first stage of the cladding heat up when an internal overpressure plays a dominant role in the cladding deformation behaviour and leads to a rapid cladding rapture due to the ballooning.

At a later stage of an accident, when the internal overpressure is absent, the influence of a thick oxide layer on a stress-state of the cladding is more important and, hence, the residual deformation strength of the oxide after cracking should be taken into consideration. Since analytical calculation of the residual deformation strength of the cracked oxide is overcomplicated, the simplified approach is used. After the oxide scale cracking only a part of the oxide thickness is assumed to have the deformation strength:

$$t_{def}^{ox} = t^{ox}(1-\lambda) , \tag{12}$$

where t_{def}^{ox} is the residual thickness of the oxide with deformation strength after cracking; t^{ox} - the oxide thickness before cracking; λ - parameter, $0 \le \lambda \le 1$, which denotes the part of the oxide thickness without the deformation strength. It is considered as a tuning parameter and its real value can be adjusted by the comparison of the simulation and experimental results. It is assumed that after oxide scale cracking the stresses in the oxide relax to zero level and then only the oxide layer with thickness t_{def}^{ox} deforms. The remained oxide layer thickness is considered as incompressible material without deformation strength, Fig. 11. In the case of further oxidation new uncracked oxide thickness is added to t_{def}^{ox}.

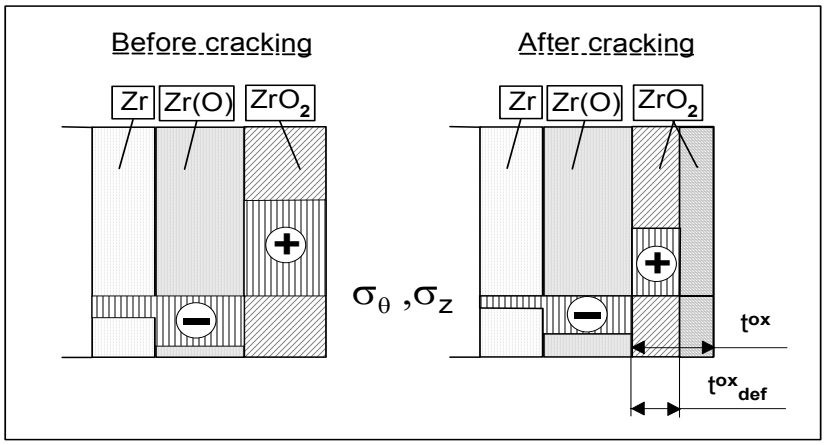

Fig.11: Reduction of the oxide scale deformation strength due to cracking

Consideration of the reduced effective thickness of the cracked oxide is an alternative method of the modelling of the deformation strength decrease due to cracking. Another one is the reduction of Young's modulus of the cracked oxide, however, in this case two oxide layers with different elastic properties should be considered: a new uncracked layer formed as a result of further oxidation, and the cracked one. After the subsequent cracking three layers should be considered, etc. Thus, the reduction of the effective thickness is a convenient method to overcome these difficulties.

The effective thickness t_{def}^{ox} corresponds to the residual deformation strength of the whole cracked oxide layer. Hence, in the real situation this residual deformation strength is uniformly distributed along the cracked oxide thickness. This should be taken into account during the «chemical thinning» of a cracked oxide under steam starvation or during its dissolution by molten Zircaloy. It is assumed that if the total cracked oxide thickness is t^{ox} and the effective thickness with the residual deformation strength is t_{def}^{ox}, then the reduction of t^{ox} leads to the proportional reduction of t_{def}^{ox}. For example, if t^{ox} = 100 μm and t_{def}^{ox} = 10 μm, then the reduction of t_{def}^{ox} to the value of 5 μm is caused by dissolution of the half of the total cracked oxide thickness t^{ox}.

5. Simulation of the oxide scale failure under "flowering" conditions

The presented below results were obtained with the help of the SVECHA/QUENCH (S/Q) code [4] designed for modelling of the single-rod quenching tests at the FZKA facility. The code was modified to take into consideration the specific features of the new FZKA tests [1] on failure criteria:

- The deformation behaviour module CROX was supplemented with the above described models of the oxide cracking and breaching under the "flowering" conditions.
- The new module LIQF for simulation of the molten Zircaloy oxidation (corrosion) and the oxide scale dissolution (erosion) by the molten Zircaloy, was implemented into the code.

5.1 Stress in the oxide scale due to radial temperature drop and the melt pressure

For preliminary estimation of the stress level in the oxide scale under "flowering" conditions the stress calculation according to the expressions (3) and (5) were performed. Only the circumferential stress is calculated, since it attains the maximum value under considered conditions.

The material properties were used from the MATPRO data base [6]. Temperature distribution was simulated by the heat-exchange module of the SVECHA/QUENCH code. It was found that the average temperature drop through the oxide scale thickness was 0.6 K/μm, melt temperature was 2220 K and the average oxide temperature was in the range of 2100-2150 K. From the consideration of the axial temperature distribution in the cladding it was concluded that the melt height in the tests was of the order of 1 cm.

The obtained results are plotted in Fig. 12 as a function of the oxide thickness with residual deformation strength. The small values of this thickness are the result of the intensive oxide cracking at temperatures above 1800 K connected with the low oxide strength at these temperatures. It was verified by simulation of the pre-heating stage by the combined S/Q code with the heat-exchange, oxidation and deformation behaviour modules.

From the presented results the following conclusions can be derived:

- For the given by Eq. (7) values of the oxide strength limits the oxide scale cracks at the onset of the metal Zircaloy melting, since the surface stress is always greater than the flexural strength, Fig. 12. For this reason, in order to fit observations presented in Table 2, the strength limits were two times enlarged in comparison with the values assumed in Eq. (7). A new comparison of the average and surface circumferential stress and the modified strength limits are presented in Fig. 13.

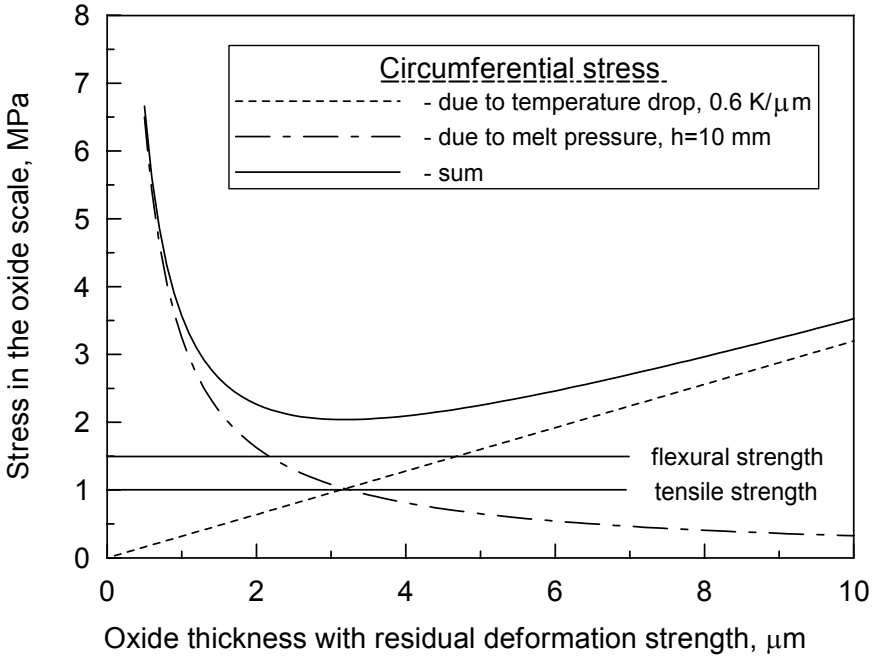

Fig.12: Circumferential stress in the oxide scale under the "flowering" conditions as a function of the oxide thickness with residual deformation strength.

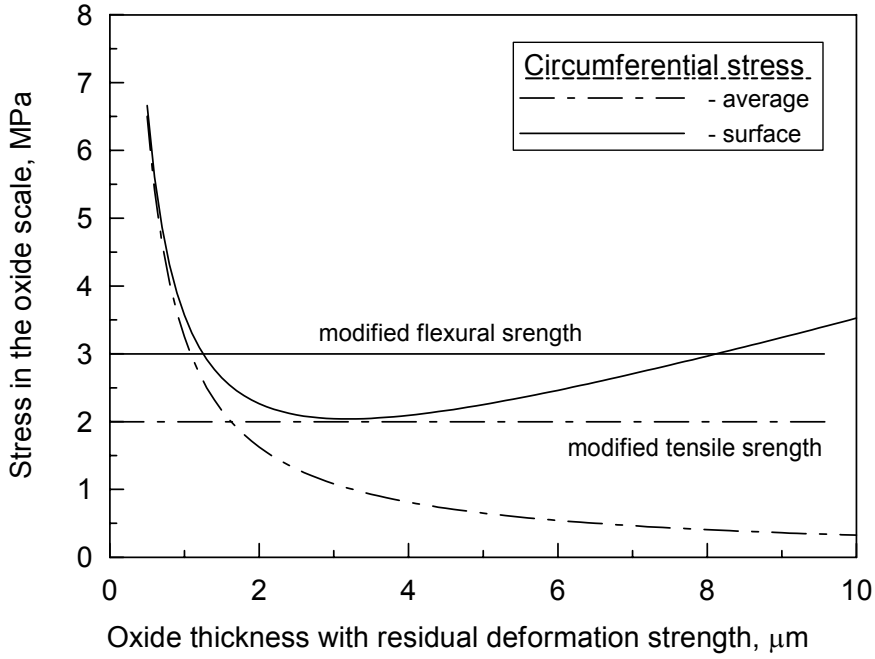

Fig.13: Comparison of circumferential stress under "flowering" conditions and the modified strength limits of the oxide.

- From Fig.13 one can see that the oxide scale cracks if the effective thickness (with residual deformation strain) exceeds $\approx$ 8 microns. Therefore, the oxide scale intensively (micro)cracks during its growth before the temperature reaches the melting point of Zircaloy. Due to cracking, a thick oxide scale without

deformation strength t^{ox} >> t_{def}^{ox} forms which prevents the though wall (macro)crack propagation and arrests the crack motion after metal cladding melting. Thus, the oxide microcracking during the heating phase prevents the instantaneous oxide scale failure after melting.

As a result, the oxide scale failure under the "flowering" conditions may be described by two alternative mechanisms:

- If the surface stress exceeds the flexural limits at Zircaloy melting, then oxide cracks until this stress becomes less than the critical value, see solid lines in Fig. 13. In the case of further melt oxidation, the new uncracked oxide layer grows and the oxide scale cracks again. Hence, t_{def}^{ox} is still at the level of about 8 microns. After the gap disappearance (due to volumetric expansion of the growing oxide), the stresses due to the incompressibility of the Zircaloy melt destroy the oxide scale.

- In the case of oxide dissolution, t_{def}^{ox} reduces proportionally to the total oxide thinning until the average circumferential stress reaches the tensile strength (see dashed lines in Fig. 13) and the oxide scale fails due to hydrostatic pressure of the melt column. In this case the dissolution period should be long enough in order to reduce t_{def}^{ox} to the value of ≈ 2 μm.

As shown below, the first mechanism is responsible for the clad failure in the case of slow heating (4 K/s) in the FZKA tests, whereas the second mechanism acts in the case of rapid heating (8 K/s).

5.2 Simulation of the FZKA "flowering" tests

The above described features of the oxide deformation and failure were taken into consideration in the deformation module CROX for prediction the oxide scale failure under conditions of the FZKA tests [1]. The test simulations were carried out by the S/Q code.

Heating history was simulated by the heat exchange module, the inductive heating was modelled by consideration of the (time dependant) volume heat source in metal layers. Under conditions of a large temperature variation in the oxide scale, the real temperature distribution is very important for oxidation, dissolution and deformation behaviour and for correct modelling of the pellets thermal expansion and the oxide scale cracking.

Oxidation kinetics was modelled by the oxidation module of the S/Q code for the solid state and by the newly implemented LIQF module in the case of Zircaloy melting. It should be noted that the material constants of the dissolution and the oxidation were found from the FZKA experimental data on the dissolution of the stabilised zirconia [3], hence, they can differ from the real oxide properties.

In Figs. 14 and 15 the simulation results of the FZKA tests 36SK and 39SK with heating rate 4 K/s (the same test conditions) and 32SK with heating rate 8 K/s, are presented. One should keep in mind that after melting one-dimensional figures represent the real system configuration (shown in Fig. 10) conditionally, however, correctly determine the free volume unoccupied by the melt.

In the case of low heating rate (Fig. 14), cladding is heavily oxidised before melting (in accordance with observations, Figs. 7 and 8). After melting oxidation (corrosion) continues up to the gap disappearance (due to volumetric expansion of oxide) and

subsequent oxide failure at 2120 °C due to a high pressure induced by incompressible melt.

In the case of heating rate 8 K/s the “flowering” occurs at the surface temperature 2097 °C as a result of the oxide scale dissolution (erosion) and failure of the thinned layer under the hydrostatic pressure of the molten Zircaloy column.

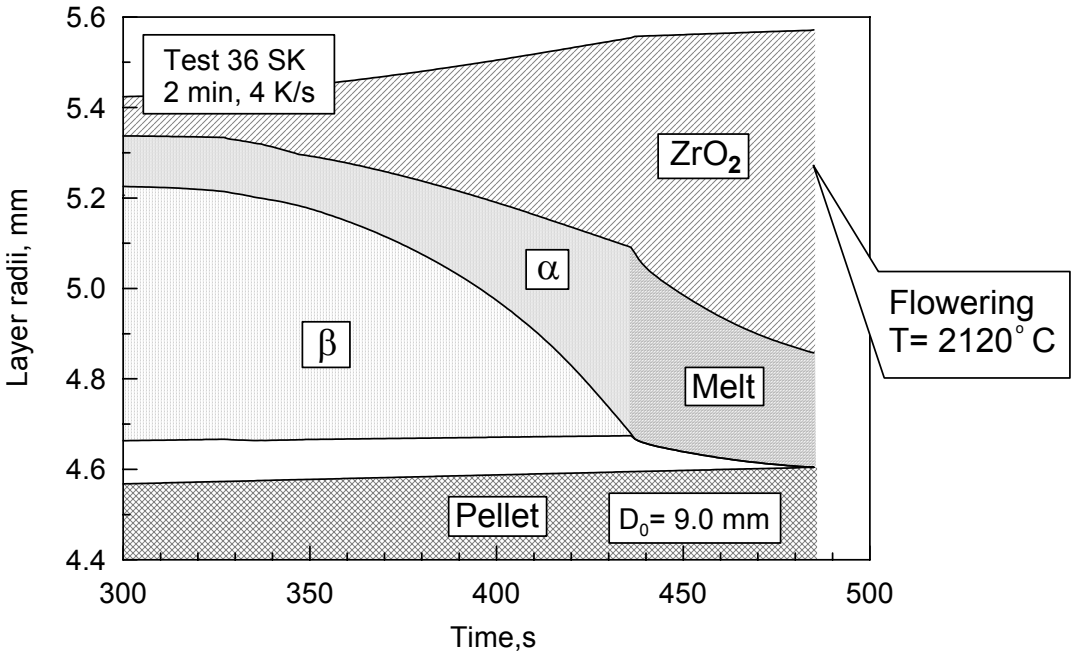

Fig.14: Evolution of the cladding layers thickness under slow heating conditions.
SQ simulation results.

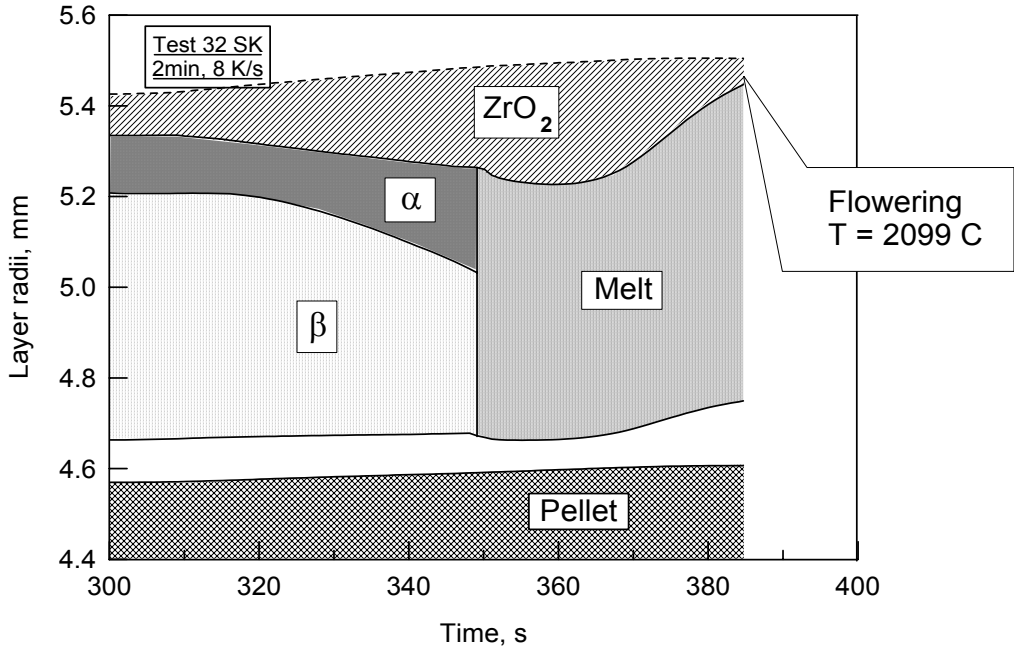

Fig.15: Evolution of the cladding layers thickness under rapid heating conditions.
SQ simulation results.

From consideration of Fig. 14 it is clear that under slow heating conditions the moment of the clad failure is rather sensitive to the gap volume and thus may be rather strongly influenced by a possible deviation (scatter) of the initial pellet radius. In order to simulate such a behaviour, an additional calculation with the initial pellet diameter 9.1 mm (instead of the standard value of 9.0 mm) was performed, Fig. 16. In this case the "flowering" occurs at a much lower temperature of the surface 1950 °C. Hence, the possible reason of a wide scatter of the "flowering" temperatures observed at low heating rates (Fig. 9) can be associated with an uncertainty in the initial pellet diameter.

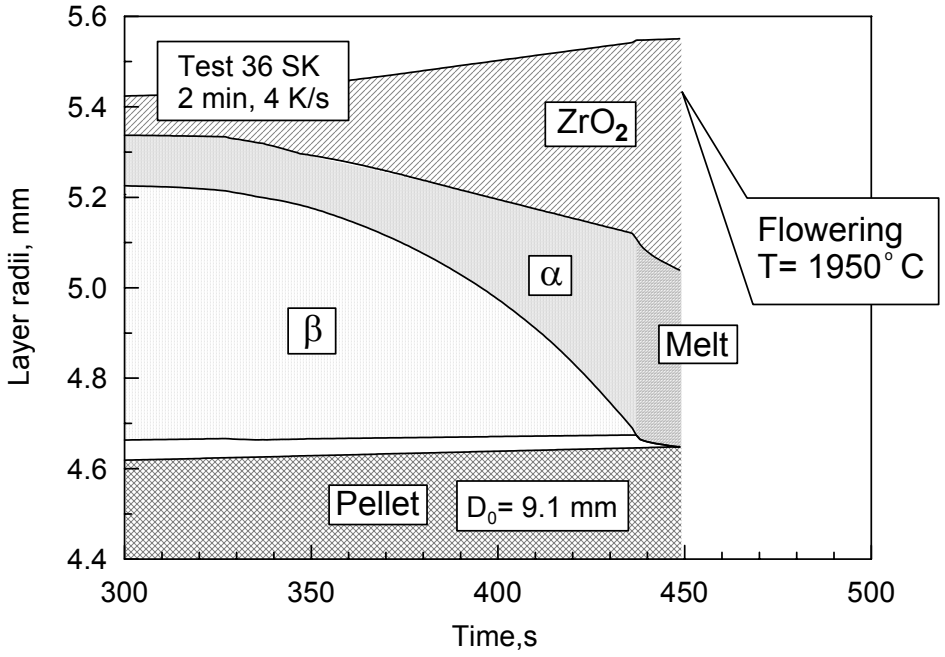

Fig.16: Evolution of the cladding layers thickness under slow heating conditions with a slightly increased pellet diameter. SQ simulation results.

6. Conclusions:

- The experiments in the small-scale QUENCH test apparatus were performed to provide a data base for the development of physically-based models for prediction of the ZrO_2 shell failure at high temperatures.
- The results of the experiments show a clear correlation between the heat-up rate and the oxide shell failure temperature. No failure occurs if a heat-up rate is less than 3 K/s — the cladding completely oxidizes before reaching the melting point of the Zircaloy. The cladding failure temperature continuously decreases with increasing heat-up rate and after reaching a certain limit (app. 6 K/s) remains constant.
- The oxide layer thickness at onset of failure decrease with increasing heat-up rate starting from 450 µm at 4 K/s and reaching 100 µm at 8 K/s and more.

- The new ZrO_2 dissolution model LIQF was successfully implemented in the single-rod code SVECHA/QUENCH.
- The mechanical deformation model CROX was modified and further developed for description of the oxidised cladding behaviour under high transient heating conditions.
- Microscopic consideration of oxidised cladding cracking and «flowering» at high temperatures under conditions of Zry melting and oxide volumetric expansion, allowed specification of the mechanistic criteria for cladding breaching.
- Self-consistent operation of the two newly implemented modules LIQF and CROX within the SVECHA/QUENCH code allows adequate description of the new FZKA tests on clad failure and modelling of different failure modes observed in these tests under various heating rates.
- It is foreseen that after complete development of the new model on simultaneous dissolution of UO_2 and ZrO_2 and its implementation (instead of the LIQF model) in the single-rod code SVECHA/QUENCH, analysis of more representative tests on single rod failure with UO_2 pellets (foreseen within the 5th Framework Programme), will be straightforward.

References:

1. *P.Hofmann, A.Miassoedov,* CIT Meeting, Prague, June 7-8, 1999, unpublished
2. *A.V.Berdyshev and M.S.Veshchunov*, 1st Interim Report, 1997 May, unpublished
3. *P.Hofmann, J.Stuckert*, Final Report INV-CIT(98) - PO26, 1999, unpublished
4. *P.Hofmann, V.Noack, M.S.Veshchunov A.V.Berdyshev, A.V.Boldyrev, L.V.Matweev, A.V.Palagin, V.E.Shestak,* "Phisico-Chemical Behavior of Zircaloy Fuel Rod Cladding Tubes During LWR Severe Accident Reflooding ", Forschungszentrum Karlsruhe, Technik und Umwelt, FZKA 5846, May 1997.
5. *A.M. Katz,* "Theory of elasticity", Techtheorpublishing, Moscow, 1956 (in Russian).
6. SCDAP/RELAP5/MOD2 Code Manual, MATPRO-A Library of Materials Properties for Light-Water-Reactor Accident Analysis. NUREG/CR-5273 EGG-2555, 1990.
7. *Y.M.Lakhtin, V.P.Leont'eva,* "Materials Research", Mashinostroenie, Moscow, 1990 (in Russian).
8. *V.L.Blagonadezjin, Y.A.Okopnyi and V.P.Chirkov,* "Mechanics of materials and constructions", MEI Publishing, Moscow, 1994 (in Russian).